HAL open science

Asymmetric local velocity distribution in a vibro-uidized granular gas and its non-classical hydrodynamic description

Yan Pei Chen

To cite this version:

Yan Pei Chen. Asymmetric local velocity distribution in a vibro-uidized granular gas and its non-classical hydrodynamic description. Other. Ecole Centrale Paris, 2014. English. NNT : 2014ECAP0016 . tel-01141249

HAL Id: tel-01141249

https://theses.hal.science/tel-01141249v1

Submitted on 11 Apr 2015

HAL is a multi-disciplinary open access archive for the deposit and dissemination of scientific research documents, whether they are published or not. The documents may come from teaching and research institutions in France or abroad, or from public or private research centers.

L'archive ouverte pluridisciplinaire **HAL**, est destinée au dépôt et à la diffusion de documents scientifiques de niveau recherche, publiés ou non, émanant des établissements d'enseignement et de recherche français ou étrangers, des laboratoires publics ou privés.

ÉCOLE CENTRALE DES ARTS ET MANUFACTURES « ÉCOLE CENTRALE PARIS »

THÈSE

présentée par

Yanpei Chen

pour l'obtention du

GRADE DE DOCTEUR

Spécialité : Physique des milieux granulaires

Laboratoire d'accueil : Laboratoire Mécanique des Sols, Structures et Matériaux

SUJET : De la dissymétrie des distributions locales des vitesses dans un gaz granulaires stationnaires excités par vibration, et de l'impossibilité de sa description à l'aide de l'hydrodynamique classique

soutenue le : le 10 Avril, 2014

devant un jury composé de :

Benoit Goyeau	-Professeur, Ecole Centrale Paris, France	**Président**
Kunquan Lu	-Chercheur, Institute of Physics, Chinese Academy of Sciences	**Rapporteur**
Philippe Gondret	-Professeur à l'Université Paris-Sud 11, France	**Rapporteur**
Benoit Goyeau	-Professeur, Ecole Centrale Paris, France	**Examinateur**
Bernard Zappoli	-Chercheur, Centre National d'Etudes Spatiales, France	**Examinateur**
Yves Garrabos	-Chercheur, Inst Chim Mat Condensee Bordeaux, Univ Bordeaux 1	**Examinateur**
Damien Durville	-Professeur, Ecole Centrale Paris, France	**Qui remplace le directeur de thèse**
Pierre Evesque	-Professeur, Ecole Centrale Paris, France	**Directeur de thèse**
Meiying Hou	-Chercheur, Institute of Physics, Chinese Academy of Sciences	**Directeur de thèse**

Asymmetric local velocity distribution in a vibro-fluidized granular gas and its non-classical hydrodynamic description

Yanpei Chen

Ecole Centrale Paris

A thesis submitted in partial fulfilment of the requirements of Ecole Centrale Paris for the degree of

Doctor of Philosophy

April 2014

I would like to dedicate this thesis to my loving parents

Acknowledgements

My dissertation has been finished. It is a wonderful experience. I learn a lot: how to do research, give talks, work with other people, learn French, participate Parabolic flight, writing papers. But I am not alone, and netted the support of many people.

I'd like to give my special thanks, beginning with Dr. Meiying Hou. She guided me through this dissertation process. She helped me to select some important subjects which were useful in my following study at the earliest. Her patience, gentle encouragement and genuine caring enabled me to overcome many difficulties.

I'd also like to give a heartfelt thank to Dr. Pierre Evesque. He had been enlightening and encouraging me a lot. When I faced many problems, he told me just to do it. His independent thoughts and open mind give me a fine example. His flexibility in scheduling is helpful to my study career. This habit helps me all the time.

I'd also like to thank Yves Garrabos, Fabien Palencia and Carole Lecoutre who helped me to do the experiment in micro-gravity. I'd like to acknowledge stimulating discussions with Kunquan Lu, Zappoli Bernard, Mario Liu and Yimin Jiang. They are all my good mentors during my growth in academic road.

I am very grateful to my friends. I have stayed in French for three years and never came back China during those three years. There are many friends who helped me to overcome all kinds of difficulties. Biyu Tian, Philippon Jessica, Jun Zheng and I passed a wonderful time. Fau Amélie and Luis Berenguer Todo Bom helped me to make progress in French and English. Frederic Douit helped me to prepare the experiment. Anne-Sophie Mouronval taught me linux.... Thanks

to my other dissertation members: Zhongsen Li, Xin Wei, Catherine Lhopital, Sylviane Bourgeois, Régis Cottereau, Nathalie Langlet, OLS Nadege, Bing Tie, Hachmi Ben Dhia, Yinchang Li, Qiong Chen, Rui Liu and Qinghua Wang.

I feel indebted to my parents upbringing. My brother also provided great encouragement. Theyve taught me about hard work and self-respect, about persistence and about how to be independent. Without their support, I could not finish my thesis.

The work on this thesis was supported by the Centre national de la recherche scientifique (CNRS) and le Centre national d'études spatial(CNES), and Chinese Academy of Science.

Abstract

The present thesis is dedicated to the experiment and simulation studies of vibro-fluidized granular gas dynamics. Granular gases are characterized by dissipation due to inelastic collisions. To keep a steady state, continuous energy is injected to balance dissipation by vibration. This system provides a platform to study the physics of non-linear, non-equilibrium and dissipative systems. This dissertation insists on the necessity of understanding the local state in the granular gases and building a new model for vibration-fluidized granular gases. Research approach includes experiments in micro-gravity, event-driven molecular dynamic simulation and experiments in tilted plane with various gravity.

Micro-gravity experiments were performed on Airbus A300(-0g) (Parabolic flight) to avoid friction with the bottom and gravity field. A long range boundary effect is found to exist in 2D vibration granular gases. Local distributions of the velocity component in the vibration direction are asymmetric in the whole cell except for the center bin. In the system, energy equipartition breaks down. "Granular temperature" is not efficient to describe such a system. We proposed a superposition of two Gaussian profiles to fit the local asymmetric velocity profiles along the vibration direction. We demonstrated the performance of this model by the Airbus experimental data and others' simulation works.

Event-driven molecular dynamics simulation was utilized. Results showed support for experiment results. Furthermore, this long range boundary effect is related to the system dissipation. This effect becomes pronounced if the coefficient of restitution ($e < 1$) decreased

or the number of particles increased. For the elastic situation, there is no such effect. This effect cannot be ignored and treated only as a local boundary effect as in hydrodynamics.

We also studied a 2D vibration fluidized granular system in a tilted plane systematically in the laboratory. The inclined angle is changed from horizontal to vertical, which changing the "effective gravity". These results also showed asymmetric local velocity distributions. Other than the number density profiles deviate from an exponential form, the spatial profiles of the number density of particles moving up and down are non-equal, and asymmetric from the cell center.

The above studies open a new view towards vibration-driven experimental dissipative granular gases systems.

Résumé

La présente thèse est consacrée à l'étude expérimentale et la simulation de la dynamique des gaz granulaires vibro-fluidisés. Les gaz granulaires sont caractérisées par une dissipation due aux collisions inélastiques. Pour maintenir cet état à l'équilibre mécanique (stationarité), l'énergie est injectée en continu depuis les bords vibrant pour équilibrer la dissipation des vibrations. Ce système fournit une base d'étude de la physique des systèmes non-linéaires, hors équilibre thermodynamique et dissipatifs. Cette thèse insiste sur la nécessité d'intégrer, de comprendre et de rendre compte de la situation inhomogène de la distribution locale dans les gaz granulaires et permet la construction d'un nouveau modèle de gaz granulaires fluidisés par des vibrations. Cette approche inclut (i) des résultats expérimentaux 2d en micro-gravité dans l'Airbus A300 0-g de Novespace, des expériences 2d avec des cellules (et des vibrations) horizontales, des expériences 2d sur plan incliné (avec vibrations et cellules inclinées et avec une gravité effective variable), ainsi que des simulations de dynamique moléculaire par la méthode "event-driven" appliquée à chaque choc.

Ces résultats confortent les simulations 3d de Liu et al. Les expériences en micro-gravité dans Airbus A300(-0g) (vol parabolique) permettent d'éviter les frottements avec les parois planes et éliminent l'effet de gravité. Les distributions locales de la vitesse dans la direction de vibrations sont asymétriques partout (à l'exception de la zone centrale de la cellule par raison de symétrie). L' équipartition de l'énergie n'est pas vérifiée dans la cellule, l'énergie est distribuée de manière inhomogène, anisotrope et directionnelle. La " température granulaire "n'est plus une mesure efficace pour décrire un tel système. On rend compte de ces résultats à l'aide d'une superposition de deux distributions gaussiennes à 2 vitesses moyennes différentes pour décrire les profils locaux de vitesse

asymétriques le long de la direction de vibration.

Les résultats des simulations de dynamique moléculaire 2D en gravité nulle montrent les mêmes tendances et confortent les résultats l'expérimentaux (dissymétrie des distributions de vitesse locales). Cette dissymétrie est un effet à longue portée et est liée à la dissipation du système: Elle augmente si le coefficient de restitution bille-bille diminue ou lorsque le nombre de particules augmente. La dissymétrie disparaît lorsque les chocs billes-billes sont élastiques. Cet effet ne peut être ignoré et doit être traité comme la frontière d'une "nouvelle hydrodynamique".

Dans les expériences de vibrations sur cellule 2D et plan incliné parallèle aux vibrations, l'angle d'inclinaison a été modifié de facon systématique de l'horizontale à la verticale, pour simuler différentes gravités effectives. Les résultats confirment une dissymétrie des distributions locales de vitesse, à laquelle se rajoute une dissymétrie supplémentaire liée à la gravité, provoquant une densité différente en haut et en bas de la cellule.

Ces études sont les prémices, nous le pensons, d'une nouvelle vision de la mécanique des gaz granulaires dissipatifs réels.

Contents

Contents viii

List of Figures xii

Nomenclature xxiii

1 Introduction 1

1.1 Definition 1

1.2 Property 2

1.3 Vibro-fluidized granular materials: Phase diagram 5

1.4 Granular gases (GG) 7

1.4.1 Experiments 8

1.4.2 Simulation on GG 9

1.5 Study objective and method 11

1.6 Structure of the dissertation 11

2 Research Progress on Granular Gases 13

2.1 Introduction 13

2.2 Boltzmann-Enskog Equation 13

2.2.1 Chapman-Enskog approach for non-uniform granular gases 14

2.2.2 Boltzmann-Enskog Equation and Sonine polynomial expansion for the homogeneous cooling gas 15

2.2.3 High energy tail 18

2.3 Hydrodynamic theory 20

2.3.1 The pressure 21

2.3.2 The temperature 23
2.4 A stochastic model 25
2.5 Granular Solid Hydrodynamics 25
2.5.1 Macroscopic relations: 26
2.5.2 GSH set of equations: 27
2.6 Discussion 29

3 Experimental results on vibrated granular matter in micro-gravity 30
3.1 Introduction 30
3.1.1 Historical background 30
3.1.2 Micro-gravity experiment 32
3.2 Experimental Setup 33
3.3 Velocity distribution function 35
3.3.1 The global velocity distribution function 35
3.3.2 Local velocity distribution 39
3.3.3 Skewness 44
3.4 the phenomenological model 45
3.5 The phenomenological model and GSH 45
3.6 Hydrodynamic description 52
3.6.1 the hydrodynamic model 52
3.6.2 The number density 52
3.6.3 The Temperature 53
3.7 The mean free path 55
3.8 Summary 59

4 Event-Driven Molecular Dynamics simulation Results 60
4.1 Introduction 60
4.2 The model 62
4.3 Velocity distribution and its skewness 64
4.4 Anisotropy of the mean free path 68
4.5 Energy Sink 70
4.6 Hydrodynamic field 71
4.6.1 Pressure 73

4.6.2 Temperature 73
4.6.3 The number density 75
4.6.4 Velocity field 77
4.6.5 The heat flux 79
4.7 The mean free path 81
4.7.1 Simulation Model and analyse method 83
4.7.2 The local mean free path 84
4.7.3 Local Velocity Distribution 87
4.7.4 The kinetic expression 92
4.8 Summary 96

5 The experiment results with the various gravity 98
5.1 Experimental setup 99
5.2 Experiment results for slightly tilted vibration 101
5.2.1 Various vibration intensity 102
5.2.1.1 The velocity distribution 102
5.2.1.2 The spatial profiles of Hydrodynamics 105
5.2.2 The number of layers 105
5.2.3 The local equation of state 106
5.3 Experiments for various degree 108
5.3.1 The velocity distribution 109
5.3.2 Spatial profiles of the number density $n^{\pm}_{x,y}$ 111
5.4 The Hydrodynamic model 113
5.5 Summary 116

6 Conclusions 118

Appendix A: Airbus data 120

Appendix B: simulation Results 124

Appendix C: experimental results on slightly tilted 2D cell 126

Appendix D:experimental results on various inclination angle(from 5 to 85) 130

References 146

List of Figures

1.1 granular materials types is illustrated: rice, desert, cobblestone, the rings of planets. 2

1.2 An example of statics problem. Scaled normal stress profiles (P/pgh) as function of scaled radial distance r/R for a sandpile.(Up)The localized-source procedure.(Down) The raining procedure[1]. . . . 3

1.3 Examples of dynamics problem: Gravity driven(surface-wave)[2], Vibration(localized oscillation)[3], Rotation(rotation drum)[4],shear[5]. 4

1.4 Jamming phase diagram for attractive particles according to [6, 7] and discussed in [8]. 5

1.5 Snapshot of vibrated-fluidized granular system in three different volume fraction from[9]. From right to left, the volume fraction is reduced one by one.(a) Maximum positive vibrational velocity. (b) Minimum negative vibrational velocity. 6

1.6 Leidenfrost effect[10, 11]. 7

1.7 Four dynamics regimes of vibro-fluidized granular system in 3D simulation are shown: (I)gaseous state, (II)partial clustering, (III)complete clustering, and (IV)bouncing aggregates. 8

1.8 Phase diagram(γ,η) of Four regimes in Fig. (1.7). 11

2.1 Profiles of the diagonal components of the pressure tensor P_{ii} in the steady state for $\alpha = 0.95$. The solid line is the calculated hydrodynamic pressure p. T_w is the temperature of the wall in x direction with a periodic excitation boundary condition in y direction[12]. . 22

2.2 Spatial profiles of the stress tensor components σ_{xx}, σ_{yy}, ρT_x, ρT_y. Here ρT is the " hydrostatic pressure", σ_{xx} is the stress tensor which is described above. The restitution coefficient $e = 0.9$, the box size is $50 * 25$. $N = 240$, particle diameter $d = 1$. 23

3.1 Snapshot of the two top cell particles. The cell contains 47 and 63 bronze sphere particles, driven in the y direction at various vibration parameters(A, V_ω, Γ, f), which is listed in the table(3.1). 35

3.2 The global velocity distributions of different components v_x and v_y. Here, y is the vibration direction. v_x is scaled by v_c^x $(0.041m/s)$. v_y is scaled by $v_c^y = 0.057m/s$. $N = 47$. The area fraction are 0.536. 37

3.3 The global velocity distributions of the components v_x and v_y. Here, y is the vibration direction. v_x is scaled by v_c^x $(0.041m/s)$. v_y is scaled by $v_c^y = 0.057m/s$. $N = 63$. The area fraction are 0.7244. 39

3.4 Local distribution functions of (a) v_y and (b) v_x on log-linear scales. There are 7 bins along the vibration direction y axis. The vibration parameter(A=0.23mm, V_ω=0.07m/s, Γ=21.56 m/s^2, $f = 49Hz$). $N = 47$. 40

3.5 Local distribution functions of (a) v_y and (b) v_x on log-linear scales. There are 7 bins along the vibration direction y axis. The vibration parameter(A=0.23mm, V_ω=0.07m/s, Γ=21.56 m/s^2, $f = 49Hz$).$N = 63$. 41

3.6 The velocity distribution in the boundary layer bin 7 and the center bin 4. 43

3.7 The skewness of v_x and v_y distribution profiles along y/L.The vibration parameter(A=0.23mm, V_ω=0.07m/s, Γ=21.56 m/s^2, $f = 49Hz$). $N = 47$. 43

3.8 The skewness profiles of v_x and v_y along the y axis for various vibrating parameters . All the parameters are listed in the Table (3.1). $N = 47$. 44

3.9 Velocity distribution as simulated in [12], measured in [13], and parameterized by Eq (3.6). Fig (a) and (b) show $f(v_x)$, for the velocity perpendicular to the vibrating walss, with (a) showing f close to the wall, and (b) showing f in the middle. Fig(c) shows $f(v_y)$, while Fig (d) again shows $f(v_x)$. Symbols are measurements, dotted lines simulation, and full curves are Eq(3.6). For the two peaks distributions, we have $T_x = 10$ and 1, $\xi = 2.2$ and -1, 37, and $\alpha = 2.3$ and 3, for Fig (a) and (d), respectively. 48

3.10 variation of stress and kinetic energy along $\hat{x}$. We employ $\sigma_{xx} = const$ as the unit of stress and energy density. Full curves are hydrodynamic results, taking $w_x = \rho b T_g^2/4 + \rho e t_{xx}^2 + \rho c \triangle_x^2/2$, and $w_y = \rho b T_g^2/4 + \rho e t_{yy}^2$, with $b_0, c, e = 1$, and $l_g = 1, 1.1, 1.2, 1$, $l_t = 0.8, 0.9, 1, 0.5$, $l_\triangle = 0.18, 0.28, 0.55, 0.3$, $a_1 = 1.38, 1.2, 0.33, 0.9$, $\rho_{cp} = 0.7, 0.7, 0.7, 0.8745$, $-\alpha = 13, 1.49, 0.772, 0.5$, $-\beta = 3.68, 2.14, 2.18, 3.5$ for (a), (b), (c), (d), respectively. Symbols are from micro-gravity measurements[13], and dotted lines from simulations of [12]. . . . 50

3.11 Variation of the packing fraction for the four cases in Fig. 3.10. Symbols are from micro-gravity measurements of [13] and dotted lines from simulations of [12]. 51

3.12 (a) The number of particles in each bin with velocity $v_x^\pm$. (b) The number of particles in each bin with velocity $v_y^\pm$. (△) V_ω=0.07m/s. (○) V_ω=0.067m/s. (●) V_ω=0.087m/s. (■) V_ω=0.038m/s. Solid curves are for the positive components, and the dashed curves for the negative ones. 53

3.13 The T_x and T_y variation in the y direction, scaled by T_{driven}, where $T_{driven} = m v_{driven}^2$. There are 7 bins along the vibration direction y axis. The vibration parameter(A=0.23mm, V_ω=0.07m/s, Γ=21.56 m/s^2, $f = 49Hz$). $N = 47$. 54

3.14 The four temperaturescompeting to describe the samples. There are 7 bins along the vibration direction y axis. The vibration parameters(A=0.23mm, V_ω=0.07m/s, Γ=21.56 m/s^2, $f = 49Hz$). $N = 47$. 55

3.15 Path of Molecule z among stationary path 56

3.16 Sketch of the breakdown of the mean free path. On the right and left sides of the cell, the v_y distribution is asymmetric, contrary to what occurs in the cell center. As there is no net flow, it means the density number n^+ and n^- are different. So this imposes to define two mean free paths through $n^- dl_c^+ = n^+ dl_c^- = 1$. 57
3.17 The spacial profiles of the collision times($L_x = L_y = 300$, $N = 47$, the vibration parameters A=0.23mm, V_ω=0.07m/s, Γ=21.56 m/s^2, $f = 49Hz$). 58
3.18 The spatial profiles of mean free path l_y^+ and l_y^-, which are calculated by Eq. 3.19($L_x = L_y = 300$, $N = 47$, the vibration parameters$A$=0.23mm, V_ω=0.07m/s, Γ=21.56 m/s^2, $f = 49Hz$). . 58

4.1 The snapshot of a granular gas $N = 360$. 63
4.2 Spatial profiles of v_x (left) and v_y (right) (semi-logarithmic) are plotted along the y direction. The particle radius r is set to be 1. The size of the cell is ($300r \times 300r$). The number N of particles is $N = 360$, the area fraction is $\phi = 0.0126$, and the restitution coefficient $e_p = 0.75$ 64
4.3 Variation of skewness in the cell, as a function of the restitution coefficient and of the particle number N. Here, y axis is the vibration direction. 65
4.4 Skewness in the boundary layer in term of restitution coefficient. . 68
4.5 The values of the fitted parameters, α. 69
4.6 The mean free path of v_y^+ and v_y^-. The particle $N = 360$, the $e_p = 0.85$ and the $e_w = 0.95$. The box is $300 * 300$. The particle diameter is 2. 69
4.7 the energy loss spacial profiles. The particle $N = 360$, the $e_p = 0.85$ and the $e_w = 0.95$. The box is $300*300$. The particle diameter is 2. 71
4.8 Variations of pressure $p_y^+(y)$ and $p_y^-(y)$ for different coefficient restitution e_p (left) and different total number of particle N. $e_w = 0.95$. The box is $300 * 300$. $N = 360$. 74

4.9 Variations of temperature $T_y^+(y)$ and $T_y^-(y)$ for different coefficient restitution e_p(left) and for different number of particle N(right). $e_w = 0.95$. The box is $300 * 300$. $N = 360$. 75
4.10 Semi-logarithmic variation of the $T_y^+(y)/T_y^-(y)$ vs y position in the cell. The number of particles N is 360, the area fraction $\phi = 0.0126$ .The size of the cell is $(300r * 300r)$, r is the particle radius. . . . 76
4.11 Variations of k, i.e the slope (in semi-log coordinate of $\tau(y)$) (see Fig. 4.10) of $ln(q(y)$ in terms of restitution coefficient. The number of particles N is 360, the area fraction $\phi = 0.0126$. The size of the cell is $(300r * 300r)$, r is the particle radius. 76
4.12 The number density spacial profiles $n_y^+(y)$ and $n_y^-(y)$ with various coefficient restitution e_p. $e_w = 0.95$. The box is $300*300$. $N = 360$ for left figure. 77
4.13 The number density Vs N 78
4.14 the mean velocity the particle $N = 360$, the $e_p = 0.75$ and the $e_w = 0.95$. The box is $300 * 300$. The particle diameter is 2. . . . 78
4.15 The spatial profiles of the four components of the rescaled heat flux q_{kin} in $e = 0.99$ (left) and $e = 0.75$(right),q_x^+, q_x^-, q_y^+, q_y^-. The number of particles is $N = 360$, the area fraction $\phi = 0.0126$. . . 80
4.16 The spatial profiles of local free path l, l_1 is the Eq.4.9 and l_2 Eq.4.10.($L_x = L_y = 300$, $e = 0.99$, $N = 1000$, $V_{driven} = 5$). 85
4.17 The spatial profiles of the mean velocity , v_x, v_x^+ and v_x^- ($L_x = L_y = 300$,$e = 0.9$,$N = 1000$,$V_{driven} = 10$). 86
4.18 The spatial profiles of local free path l^+ and l^-. 87
4.19 The spatial profiles of scaled free path l^+ and l^- under various box size. The note number $\sharp 1$ $L_x = 600$, $\sharp 2$ $L_x = 1200$, $\sharp 3$ $L_x = 1500$, $\sharp 4$ $L_x = 1800$, $\sharp 5$ $L_x = 4200$. All the free path are sealed by their L_x.($e = 0.9$,$N = 1000$,$V_{driven} = 5$,$L_y = 300$) 88
4.20 3D probality disitrbution of the velocity.($L_x = L_y = 300$,$e = 0.9$,$N = 1000$,$V_{driven} = 10$). 89
4.21 The spatial profiles of the fitting parameters T_y($L_x = L_y = 300$,$e = 0.9$,$N = 1000$,$V_{driven} = 10$). 90

4.22 The spatial profiles of the fitting parameters a ($L_x = L_y = 300$,$e = 0.9$,$N = 1000$,$V_{driven} = 10$). 91
4.23 The spatial profiles of the fitting parameters ξ($L_x = L_y = 300$,$e = 0.9$,$N = 1000$,$V_{driven} = 10$). 91
4.24 The spatial profiles of the fitting parameters S ($L_x = L_y = 300$,$e = 0.9$,$N = 1000$,$V_{driven} = 10$). 92
4.25 Parametric plots of Eq.4.24 l^+ (■) and Eq. (4.25) l^-(●), compared with the free path l^+ (□)and l^- (○) the simulation results with parameters $L_x = L_y = 600$,$e = 0.9$,$N = 1000$,$V_{driven} = 5$. 95

5.1 the experimental setup. 100
5.2 Snapshot of the cell and particles. The cell ($L_x * L_y = 70mm * 50mm$) contains 256 bronze sphere particles, driven in the x direction at various vibration parameters(A, V_ω, Γ, f). 101
5.3 The global velocity distributions of the components v_x and v_y. Here, x is the vibration direction. v_x and v_y is scaled by their mean squared. The vibration parameters are listed in Item 5 in Table. 5.1). 103
5.4 Local distribution $f(v_x)$ on log-linearscales of vibration parameters Item 5 (in Table. 5.1). 104
5.5 Local v_y distribution $f(v_y)$ on log-linear scales of vibration parameters Item 5 (in Table. 5.1). 104
5.6 Skewness of $f(v_x)$ as function of vibration parameters in Table. 5.1. 104
5.7 The Probability distribution $f(v_x)$ versus the number of particle. The solid line in red Gaussian fitting for $N = 160$. The vibration parameters are listed in the Table. 5.2. 106
5.8 The maximum of the number density profiles versus total particle number N. The size of box is $70mm * 50mm$, the diameter of a particle is $3mm$. The particle change from one layer to 14 layers(16 particles per layer). The vibration parameters are listed in the Table. 5.2. 107

5.9 The spatial profiles of the stress versus total particle number N: σ_{xx}, σ_{yy},σ_{xx}^{kin}, σ_{yy}^{kin},σ_{xx}^{int}, σ_{yy}^{int}. The size of box is $70mm * 50mm$, the diameter of a particle is $3mm$, the number of particles is 256. The vibration parameters: the vibration frequencies $50Hz$, the acceleration $110m/s^2$. 108
5.10 The semi-logarithmic plots the $G(\phi)$ under various area fractions. The solid line is calculated by Eq. 5.2. we suppose $\alpha = 0.8$. The size of box is $70mm*50mm$, the diameter of a particle is $3mm$, the number of particles is from 80 to 256. The vibration parameters: the vibration frequencies $60Hz$, the acceleration $130m/s^2$. 109
5.11 The global velocity distributions of different components v_x and v_y. Here, x is the vibration direction. v_x and v_y are scaled by their mean squared. The vibration parameters are listed in Table 22). Degree is 30°. 110
5.12 The probability distribution $f(v_x)$ versus the tilted angle. x is the vibration direction. 111
5.13 Spatial profiles of the number particles $n_x^{\pm}$ and $n_y^{\pm}$. Here, x is the vibration direction. The vibration parameter is listed in Table. D.22), Label #1 corresponds to 5.5° inclination, #2 to 20.5°, #3 to 50.5°, #4 to 65.5° , and #5 to 85.5°.The number of particles is 112 and the area fraction is 0.23. 112
5.14 The spatial profiles of the mean velocity $v_x^{\pm}$ and $v_y^{\pm}$. Here, x is the vibration direction. The vibration parameters are listed in Table. 22). (Left)5.5°. (right) 35.5° 113

1 Experimental results of scaled pressure $p_x^{\pm}$ profiles in y direction, $N = 47$, and vibration parameters labelled Item 1 $\sim$ 4 in Table. 3.1). 120
2 Experimental results of scaled pressure $p_y^{\pm}$ profiles in y direction, $N = 47$, and vibration parameters labelled Item 1 $\sim$ 4 in Table. 3.1). 120

3 Experimental results of scaled pressure $p_x^{\pm}$ profiles in y direction, $N = 47$, and vibration parameters labelled Item 5 $\sim$ 6 in Table. 3.1). 121
4 Experimental results of scaled pressure $p_y^{\pm}$ profiles in y direction, $N = 47$, and vibration parameters labelled Item 5 $\sim$ 6 in Table. 3.1). 121
5 Experimental results of scaled temperature $T_x^{\pm}$ profiles in y direction, $N = 47$, and vibration parameters labelled Item 1 $\sim$ 4 in Table. 3.1). 121
6 Experimental results of scaled temperature $T_y^{\pm}$ profiles in y direction, $N = 47$, and vibration parameters labelled Item 1 $\sim$ 4 in Table. 3.1). 121
7 Experimental results of scaled temperature $T_x^{\pm}$ profiles in y direction, $N = 47$, and vibration parameters labelled Item 5 $\sim$ 6 in Table. 3.1). 122
8 Experimental results of scaled temperature $T_y^{\pm}$ profiles in y direction, $N = 47$, and vibration parameters labelled Item 5 $\sim$ 6 in Table. 3.1). 122
9 Experimental results of number of particle $N_x^{\pm}$ profiles in y direction, $N = 47$, and vibration parameters labelled Item 1 $\sim$ 4 in Table. 3.1). 122
10 Experimental results of number of particle $N_y^{\pm}$ profiles in y direction, $N = 47$, and vibration parameters labelled Item 1 $\sim$ 4 in Table. 3.1). 122
11 Experimental results of number of particle $N_x^{\pm}$ profiles in y direction, $N = 47$, and vibration parameters labelled Item 5 $\sim$ 6 in Table. 3.1). 123
12 Experimental results of number of particle $N_y^{\pm}$ profiles in y direction, $N = 47$, and vibration parameters labelled Item 5 $\sim$ 6 in Table. 3.1). 123

13 The number of particle $N_y^{\pm}$ for various coefficient of restitution. The particle radius r is set to be 1. The size of the cell is ($300r \times 300r$). The number N of particles is $N = 360$, the area fraction is $\phi = 0.0126$. 124
14 The pressure $p_y^{\pm}$ for various coefficient of restitution. The particle radius r is set to be 1. The size of the cell is ($300r \times 300r$). The number N of particles is $N = 360$, the area fraction is $\phi = 0.0126$. 125
15 The pressure $T_y^{\pm}$ for various coefficient of restitution. The particle radius r is set to be 1. The size of the cell is ($300r \times 300r$). The number N of particles is $N = 360$, the area fraction is $\phi = 0.0126$. 125
16 (upper left) The scaled temperature T_x^{pm} with velocity $v_x^{\pm}$.. (upper right) Pressure. (low left) Number of particle with $v_x^{\pm}$. (low right) Number of particle with $v_y^{\pm}$. Parameters are in Table. 1. 127
17 Local v_x distribution $f(v_x)$ on log-linear scales for vibration parameters Item 1 and in units of Item 1, as the bin number (in Table. 2). 128
18 Local v_y distribution $f(v_y)$ on log-linearscales of vibration parameters Item 1 (in Table. 2). 128
19 (upper left) Temperature in each bin as a function of the bin number, and rescaled by v_ω^2 . (upper right) Pressure with $v_x^{\pm}$. (low left) Number of particle with $v_x^{\pm}$. (low right) Number of particle with $v_y^{\pm}$. Parameters are in Table. 2. 129
20 Local v_y distribution $f(v_y)$ on log-linearscales of vibration parameters ($D = 5.5°$ and $N = 64$ labelled 1 in Table. 22). 131
21 Local v_x distribution $f(v_x)$ on log-linearscales of vibration parameters ($D = 5.5°$ and $N = 64$ labelled 1 in Table. 22). 131
22 (upper left) The scaled temperature $T_x^{\pm}$ with velocity $v_x^{\pm}$. (upper right) The scaled pressure $p_x^{\pm}$ with velocity $v_x^{\pm}$. (low left) Number of particle with $v_x^{\pm}$. (low right) Number of particle with $v_y^{\pm}$. $D = 5.5°$ and vibrational parameters are in Table. 22. 131
23 Local v_y distribution $f(v_y)$ on log-linearscales of vibration parameters ($D = 10.5°$ and $N = 64$ labelled 1 in Table. 22). 132

24 Local v_x distribution $f(v_x)$ on log-linearscales of vibration parameters ($D = 10.5°$ and $N = 64$ labelled 1 in Table. 22). 132
25 (upper left) The scaled temperature $T_x^{\pm}$ with velocity $v_x^{\pm}$. (upper right) The scaled pressure $p_x^{\pm}$ with velocity $v_x^{\pm}$. (low left) Number of particle with $v_x^{\pm}$. (low right) Number of particle with $v_y^{\pm}$. $D = 10.5°$ and vibrational parameters are in Table. 22. 133
26 Local v_y distribution $f(v_y)$ on log-linearscales of vibration parameters ($D = 15.5°$ and $N = 64$ labelled 1 in Table. 22). 133
27 Local v_x distribution $f(v_x)$ on log-linearscales of vibration parameters ($D = 15.5°$ and $N = 64$ labelled 1 in Table. 22). 133
28 (upper left) The scaled temperature $T_x^{\pm}$ with velocity $v_x^{\pm}$. (upper right) The scaled pressure $p_x^{\pm}$ with velocity $v_x^{\pm}$. (low left) Number of particle with $v_x^{\pm}$. (low right) Number of particle with $v_y^{\pm}$. $D = 15.5°$ and vibrational parameters are in Table. 22. 134
29 Local v_y distribution $f(v_y)$ on log-linearscales of vibration parameters ($D = 20.5°$ and $N = 64$ labelled 1 in Table. 22). 134
30 Local v_x distribution $f(v_x)$ on log-linearscales of vibration parameters ($D = 20.5°$ and $N = 64$ labelled 1 in Table. 22). 134
31 (upper left) The scaled temperature $T_x^{\pm}$ with velocity $v_x^{\pm}$. (upper right) The scaled pressure $p_x^{\pm}$ with velocity $v_x^{\pm}$. (low left) Number of particle with $v_x^{\pm}$. (low right) Number of particle with $v_y^{\pm}$. $D = 20.5°$ and vibrational parameters are in Table. 22. 135
32 Local v_y distribution $f(v_y)$ on log-linearscales of vibration parameters ($D = 25.5°$ and $N = 64$ labelled 1 in Table. 22). 136
33 Local v_x distribution $f(v_x)$ on log-linearscales of vibration parameters ($D = 25.5°$ and $N = 64$ labelled 1 in Table. 22). 136
34 (upper left) The scaled temperature $T_x^{\pm}$ with velocity $v_x^{\pm}$. (upper right) The scaled pressure $p_x^{\pm}$ with velocity $v_x^{\pm}$. (low left) Number of particle with $v_x^{\pm}$. (low right) Number of particle with $v_y^{\pm}$. $D = 25.5°$ and vibrational parameters are in Table. 22. 137
35 Local v_y distribution $f(v_y)$ on log-linearscales of vibration parameters ($D = 35.5°$ and $N = 64$ labelled 1 in Table. 22). 138

36 Local v_x distribution $f(v_x)$ on log-linearscales of vibration parameters ($D = 35.5°$ and $N = 64$ labelled 1 in Table. 22). 138
37 (upper left) The scaled temperature $T_x^{\pm}$ with velocity $v_x^{\pm}$. (upper right) The scaled pressure $p_x^{\pm}$ with velocity $v_x^{\pm}$. (low left) Number of particle with $v_x^{\pm}$. (low right) Number of particle with $v_y^{\pm}$. $D = 35.5°$ and vibrational parameters are in Table. 22. 139
38 Local v_y distribution $f(v_y)$ on log-linearscales of vibration parameters ($D = 45.5°$ and $N = 64$ labelled 1 in Table. 22). 139
39 Local v_x distribution $f(v_x)$ on log-linearscales of vibration parameters ($D = 45.5°$ and $N = 64$ labelled 1 in Table. 22). 139
40 (upper left) The scaled temperature $T_x^{\pm}$ with velocity $v_x^{\pm}$. (upper right) The scaled pressure $p_x^{\pm}$ with velocity $v_x^{\pm}$. (low left) Number of particle with $v_x^{\pm}$. (low right) Number of particle with $v_y^{\pm}$. $D = 45.5°$ and vibrational parameters are in Table. 22. 140
41 Local v_y distribution $f(v_y)$ on log-linearscales of vibration parameters ($D = 55.5°$ and $N = 64$ labelled 1 in Table. 22). 140
42 Local v_x distribution $f(v_x)$ on log-linearscales of vibration parameters ($D = 55.5°$ and $N = 64$ labelled 1 in Table. 22). 140
43 (upper left) The scaled temperature $T_x^{\pm}$ with velocity $v_x^{\pm}$. (upper right) The scaled pressure $p_x^{\pm}$ with velocity $v_x^{\pm}$. (low left) Number of particle with $v_x^{\pm}$. (low right) Number of particle with $v_y^{\pm}$. $D = 55.5°$ and vibrational parameters are in Table. 22. 141
44 Local v_y distribution $f(v_y)$ on log-linearscales of vibration parameters ($D = 65.5°$ and $N = 64$ labelled 1 in Table. 22). 141
45 Local v_x distribution $f(v_x)$ on log-linearscales of vibration parameters ($D = 65.5°$ and $N = 64$ labelled 1 in Table. 22). 141
46 (upper left) The scaled temperature $T_x^{\pm}$ with velocity $v_x^{\pm}$. (upper right) The scaled pressure $p_x^{\pm}$ with velocity $v_x^{\pm}$. (low left) Number of particle with $v_x^{\pm}$. (low right) Number of particle with $v_y^{\pm}$. $D = 65.5°$ and vibrational parameters are in Table. 22. 142
47 Local v_y distribution $f(v_y)$ on log-linearscales of vibration parameters ($D = 75.5°$ and $N = 64$ labelled 1 in Table. 22). 142

48 Local v_x distribution $f(v_x)$ on log-linearscales of vibration parameters ($D = 75.5°$ and $N = 64$ labelled 1 in Table. 22). 142
49 (upper left) The scaled temperature $T_x^{\pm}$ with velocity $v_x^{\pm}$. (upper right) The scaled pressure $p_x^{\pm}$ with velocity $v_x^{\pm}$. (low left) Number of particle with $v_x^{\pm}$. (low right) Number of particle with $v_y^{\pm}$. $D = 75.5°$ and vibrational parameters are in Table. 22. 143
50 Local v_y distribution $f(v_y)$ on log-linearscales of vibration parameters ($D = 85.5°$ and $N = 64$ labelled 1 in Table. 22). 144
51 Local v_x distribution $f(v_x)$ on log-linearscales of vibration parameters ($D = 85.5°$ and $N = 64$ labelled 1 in Table. 22). 144
52 (upper left) The scaled temperature $T_x^{\pm}$ with velocity $v_x^{\pm}$. (upper right) The scaled pressure $p_x^{\pm}$ with velocity $v_x^{\pm}$. (low left) Number of particle with $v_x^{\pm}$. (low right) Number of particle with $v_y^{\pm}$. $D = 85.5°$ and vibrational parameters are in Table. 22. 145

Chapter 1

Introduction

1.1 Definition

Granular matter is defined as particle systems with a particle size larger than one micron[14]. There is no upper limit for the size. In nature, granular materials are so widespread. There are many obvious examples, such as sand, snow, coal, grains, industrial products, rice, nuts, the rings of planets, the solar system.... From this definition, we find granular materials ignore the thermal agitation, which exists in materials below one micron due to the environment (gas or liquid...)[14]. In[15, 16], granular materials are classified according to interaction type between particles:

i) **powder**: whose diameter of particles is smaller than 100 μm. Electrostatic force exists between particles. The humidity of environment influences forcefully on the granular materials property.

ii) **granular solid**: whose diameter of particles is between 100 μm and 3000 μm. Electrostatic force can be neglected. More, the humidity of environment influences its properties.

iii) **solid debris**: whose diameter of particles is larger than 3000 μm. The movements of particles are independent of electrostatic force and the humidity of environment.

Granular media are the second largest manipulated materials[14]. In industries, most raw materials are granular media. How to mix, grind, transport,

Figure 1.1: granular materials types is illustrated: rice, desert, cobblestone, the rings of planets.

segregate, pack up and store are very important processes. In geology, disasters like mud avalanche, snow avalanche, landslide, and earthquake are related to the physics of granular materials. To avoid these disasters, it is necessary to study granular fundamental problem. In brief, to explore the science of granular media is important to solve the problem in the human daily life.

1.2 Property

In this section, we exemplify few important properties of granular materials through four driven methods in granular dynamics process. Granular materials are studied by engineers and physicists from different perspectives. At the earliest, granular matter was studied widely by engineers on demand of practical problems, such as Rock and Soil Rheology. Meanwhile, a lot of research work on the granular media have been done by physicists, such as Coulomb, Bagnold, Faraday, Hagen, Hertz, Huygens, Reynolds, and Terzaghi[17]. However, there is still not a satisfying theory for granular matter like those one finds in classical gases, liquids or solids. As De Gennes[18] said, granular materials have similar complexity and flexibility as other soft matter; at present, the physical properties

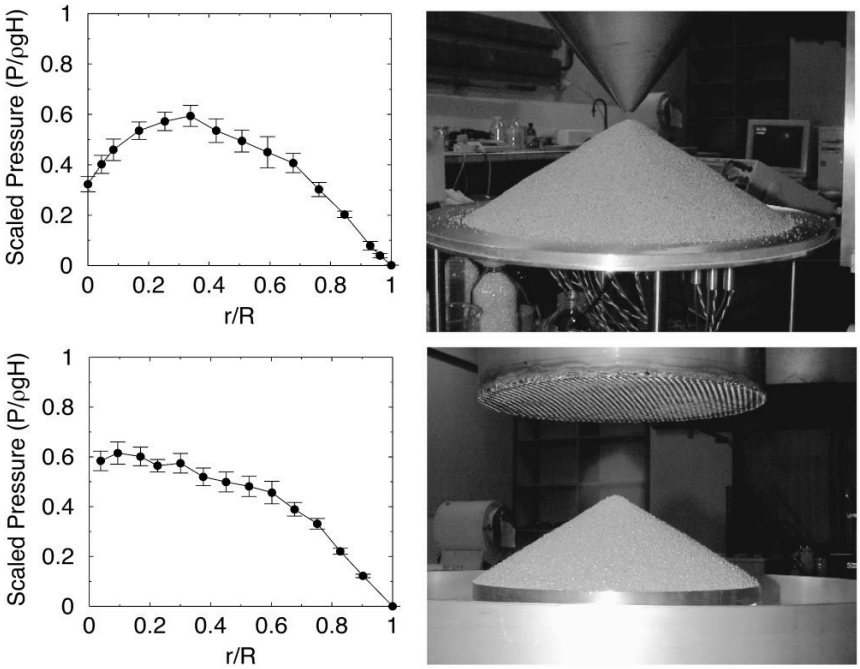

Figure 1.2: An example of statics problem. Scaled normal stress profiles (P/pgh) as function of scaled radial distance r/R for a sandpile.(Up)The localized-source procedure.(Down) The raining procedure[1].

of granular systems are still a great challenge for physicists.

Granular matter exhibits remarkable phenomena such as Rayleigh-Bénard convection, cluster, Taylor-Couette flows, gravity waves, shear flows, pattern formation, and Maxwell's demon[19]. It is interesting and draw more attention. All studies of granular behaviors are classified into statics and dynamics problems (sometimes one more, quasi-statics).

For statics problems, the reference[14] gives a tentative view for granular matter. As discussed in [14], one can include in statics problems: compaction, the packing volume fraction[20], boundary conditions(the free surface or at a solid wall), a silo model, avalanches[21], a heap (sandpile)[1, 22–27], deformations, force channels[28], and the local distribution of forces. Fig. 1.2 gives an example of statics problem, i. e. a local pressure distribution for a sandpile, leading to discussions [1, 22–27].

Difficulty about dynamics behavior is linked to the dissipative nature of gran-

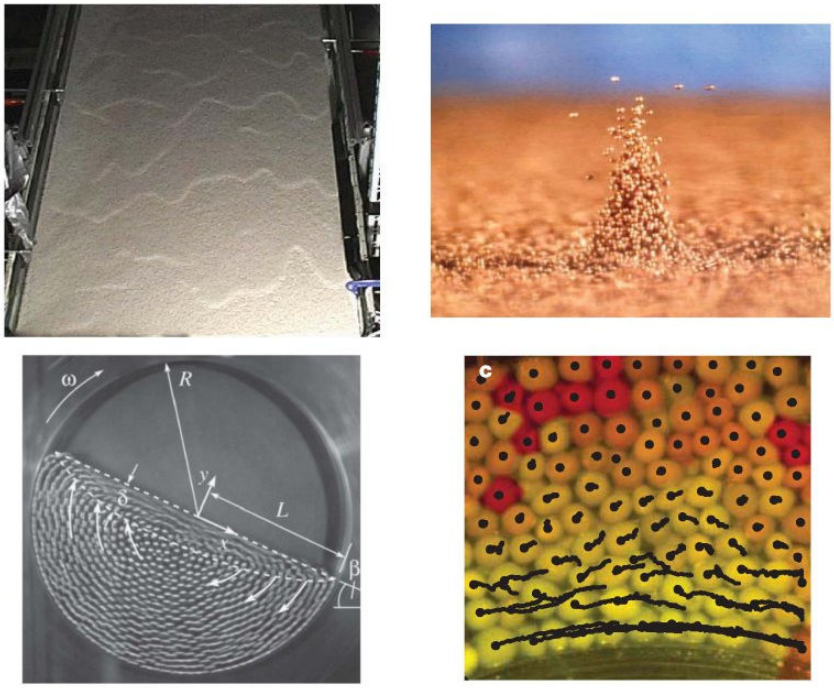

Figure 1.3: Examples of dynamics problem: Gravity driven(surface-wave)[2], Vibration(localized oscillation)[3], Rotation(rotation drum)[4],shear[5].

ular systems, made of inelastic collisions or solid and "viscous" friction. However, the difficulty would be worse without it, since it should introduce developed turbulence directly. To study the dynamics behaviors of granular systems, one shall inject energy to the systems through gravity, shear, rotation, vibration or other means[29] (to balance the dissipation). Fig. 1.3 gives several examples for different methods of repulsing or injecting energy. Granular dynamics problems are fundamental and provide a platform to study the "frontier of modern physics "[30]. It relates to plasticity of solids, fracture, friction in a complex system. Obvious examples contain vehicular traffic[31], patterns formation[3, 32], hopper flow, convection rolls, diffusion, free cooling, jamming(Fig. 1.4)[6–8], rapid grain flow, granular gases, compartmentalized granular gases, rotating drum, size segregation[33, 34], and granular mixture.

There are some review papers about granular materials dynamics[35–43]. In[39], granular materials are explored under three different conditions, i.e. granular solids, granular liquid and granular gases. These three conditions correspond

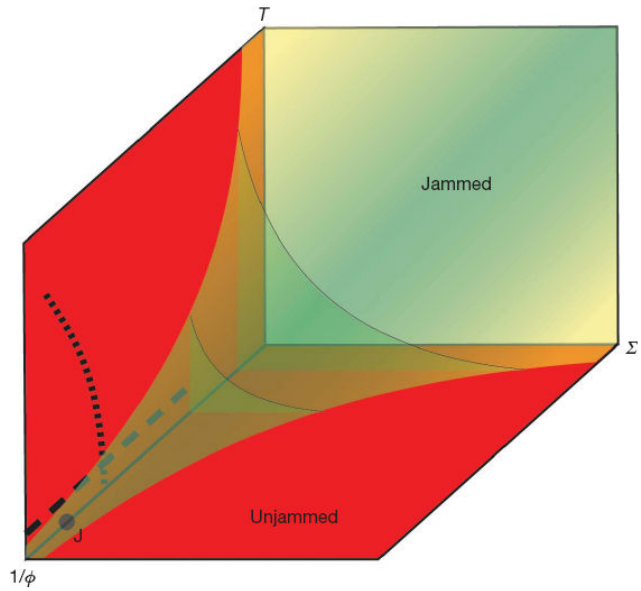

Figure 1.4: Jamming phase diagram for attractive particles according to [6, 7] and discussed in [8].

to classical solids, liquids and gases. Classical theories of solids, liquid and gases are used to describe behaviors observed in granular materials. For instance, theories of ideal gases are used for the granular gas, and hydrodynamics are adopted for the granular flow. However, granular media are have some unique properties which are different from classical ones. As said in[39], it needs to be emphasized that "any seemingly fluid like behavior of granular matter is a purely dynamics phenomenon".

In next section, we discuss the unique features in vibration-driven granular systems.

1.3 Vibro-fluidized granular materials: Phase diagram

There are many cases where vibro-fluidized granular materials are used and studied, such as a single cell vs compartmentalized cell, a mono-type particle vs binary mixture and so on. In this thesis, the dynamics behavior of a single 2d rectangular

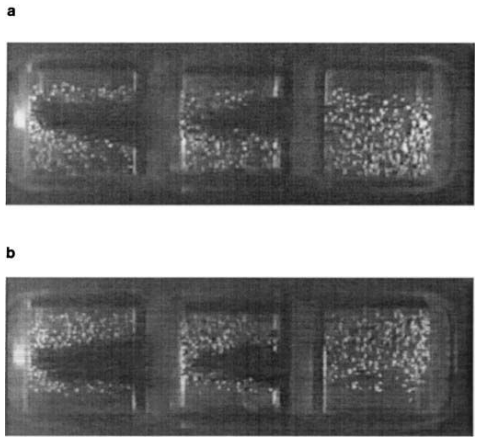

Figure 1.5: Snapshot of vibrated-fluidized granular system in three different volume fraction from[9]. From right to left, the volume fraction is reduced one by one.(a) Maximum positive vibrational velocity. (b) Minimum negative vibrational velocity.

cell containing a single type of particle is investigated, by using both the experimental and simulation approaches. This is a simple and intuitive toy model, of which phase diagram has been investigated by few teams[44]. However, most have not been touched on the physics underlying this system, which will be found in the following.

To begin and summarize all the content in vibro-fluidized granular materials, it is a good choice to discuss the phase diagram. According to the presence or absence of gravity field, the discussion on phase diagram can be found in[44] (Microgravity) and[45](gravity) in particular.

(I),**in microgravity**. In[9], an experimental study of a vibro-fluidized granular system in *Mini-Texux 5* microgravity is reported. Two kinetic regimes, homogeneous and clusterized, are presented (shown in Fig. 1.5). Besides, in[44], authors investigate granular gases in zero-gravity based on 3D molecular dynamics simulation. Four dynamical regimes (Fig. 1.7) are found[10]: gaseous state, partial clustering, complete clustering, and bouncing aggregates (shown in Fig. 1.7). Phase diagram (r, η) of this four regimes is drawn (Fig. 1.8). $r = R/L$, where R is the radius of a particle, L is the box size, $\eta = 4N\pi r^3/3$ is the volume fraction.

(II), **under gravity**. The phase diagram is divided into five regimes: bounc-

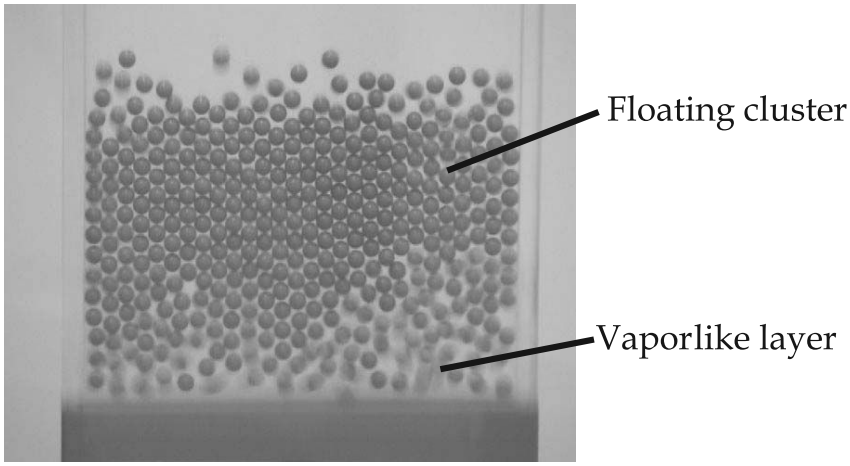

Figure 1.6: Leidenfrost effect[10, 11].

ing bed, undulations, granular Leidenfrost effect (This special case [10] is shown in Fig. 1.6), convection rolls and granular gases.

In this thesis, we are only interested on the gaseous state for vibrated-fluidized granular system in micro-gravity (in the 3st and 4nd Chapter) and in various force field (in 5th Chapter).

1.4 Granular gases (GG)

A highly fluidized granular system is referred as a granular gas[46]. Granular gases are dilute granular systems. In[47], granular gas is named rapid granular flow. In such system, most collisions between particles are binary. In the following part, we discuss the previous studies on granular gases from the experiment and simulation aspects. The granular gas theory will be discussed and described in next Chapter.

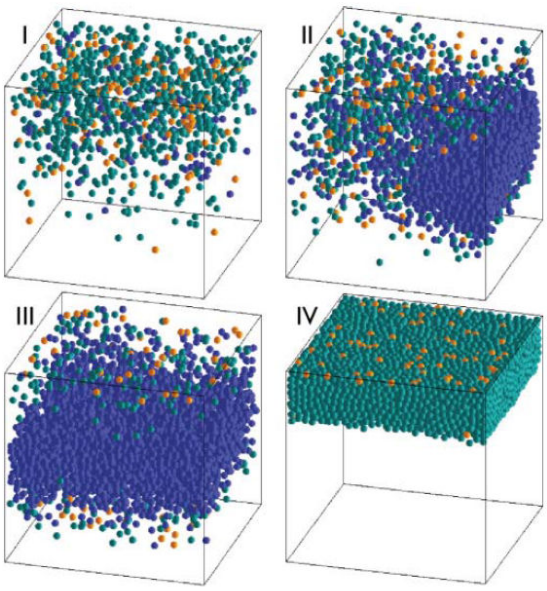

Figure 1.7: Four dynamics regimes of vibro-fluidized granular system in 3D simulation are shown: (I)gaseous state, (II)partial clustering, (III)complete clustering, and (IV)bouncing aggregates.

1.4.1 Experiments

There are many experimental methods to study granular gases. Most can be found in [47]: two dimensions(2D) tracking such as NMR methods (Nuclear Magnetic Resonance Imaging)[48], positron emission particle tracking method[49], video recording system; three dimensions (3D) tracking which can be found in[46]. 2D tracking can only obtain the translational movement, while 3D tracking can record the rotation of each particle[46]. Among all these 2D methods, video recording system is widely used. Image frames[50] are used to observe two dimensional movements of particles. Firstly, particle positions are recorded by high speed camera, and then movement is calculated by tracking algorithm. Many tracking methods can be found, for example minimum distance or Kalman filter algorithm. In the following part, we present some experimental results.

In[50, 51], vibro-fluidized granular system models were investigated at the earliest. They used digital high speed camera and particle tracking technology to obtain movements of particles. A Boltzmann distribution was observed in two

components of the velocity: v_x and v_y. y is the vibration direction. However, with the advance in technology, a Non-Gaussian distribution is found in many experiments[52–55]. All those results show the GG velocity distribution is rather exponential. But the power of exponential distribution is not the same in these works, which ranges from 1 to 2 (When the value is 2, it is Gaussian). Comparing with Gaussian distribution, experimental distribution is higher near the tails of the velocity profiles. What is remarkable, Gaussian and non-Gaussian are observed at the same time in[56]; in this case, there are two particle layers confined in the vertical plane; and the velocity distribution of the upper layer is Gaussian, while the bottom one is non-Gaussian distribution. It should be stressed here that most experiments consider that excitation is obtained by vibration, and that boundary plays the part of a boundary heater; only few works are using electrostatically driven excitation[57] by vibration.

Besides the study of the velocity distribution function, the studies of collisions statistics[58], Molecular Chaos, dissipation of driven granular materials are also investigated in the experiment. Granular system is found different from molecular system since the effective coefficient of restitution is found to have a broad distribution for the same impact angles. The distribution of the free path and collision rules are found to deviate from elastic forms. This will be discussed in detail in Chapter 3.

1.4.2 Simulation on GG

Granular gases are composed of discrete grains. To describe this system, Molecular dynamics simulation, Direct Monte Carlo Simulation, Cellular Automate, and Brownian Dynamics Simulation are common simulation methods. We will describe them briefly.

Molecular dynamics simulation (*MD simulation*) is intuitive. There are the hard and the soft sphere models. For the Hard sphere Model, a particle is considered as a rigid body which is not deformable during collision; collisions are forecast by collision rules from trajectory parameters. For the soft sphere Model, particles are deformable; Each particle is suffering different forces from surrounding particles leading to local deformation. Then one calculates the forces on each

particle and obtain the particle movement. So the force model is critical for Soft Sphere Mode; among them one can quote the Hooke Model(linear) and Hertz Model is common force model.

Direct Simulation Monte Carlo (DSMC) method[59] is used to simulate dilute granular gases. DSMC does not directly describe particle trajectories but lead to determination the local time-dependent distribution function $f(\vec{r}, \vec{v}, t)$ by means of a quasi-particle simulation[17]. This method is efficient and can simulate much larger system than Molecular dynamics simulation. But it is only used to simulate the granular quasi-static state. So it can not be used widely.

Anyway, whatever the simulation method used, a collision model is necessary to be used and its complexity discussed. In reality, during a collision few micro-cracks can be generated on a particle that collide, or some attrition or erosion can happen...; so the process can be quite complex. For sake of simplicity, one can assume rather simple collision laws, as far as the law is complex enough one shall expect results similar to real behavior. For instance, postcollision velocity is calculated from the binary collision theory where the restitution coefficient is constant. As told already, normal restitution coefficient e is supposed in most theories and simulation; some others take into account a tangential restitution[60] , or a random restitution coefficient e or a normal restitution coefficient e that depends on the relative velocity[61].

For the simulation results, one also can get some exponential-like distributions[62, 63] for vibration-fluidized granular gases which are consistent with experimental results. Some previous results have been done by R. Liu, whose results are consistent to ours. But they were mainly alone; this is the reason why we undergo the present PhD work. In [64, 65], Gaussian velocity distribution is found for uniform thermal heating, and a non-Gaussian velocity distribution (or exponential-like) or boundary heating. Except for velocity distribution, many simulation works focus on an interpretation using Hydrodynamic studies[66, 67], but we will come back to this topic a little further in the next chapter.

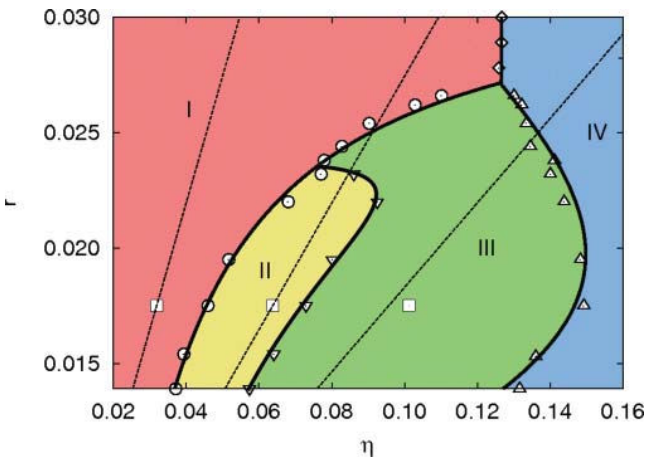

Figure 1.8: Phase diagram(γ,η) of Four regimes in Fig. (1.7).

1.5 Study objective and method

If most GG studies concern single cell, others concern also compartmentalized granular gases.

Experimentally, to obtain granular gases in steady state, it needs to inject energy continuously to balance the energy dissipation due to inelastic collision. In most experiments, energy is supplied by the boundary vibration.

To test the particle experimentally, one can try using Positron-Emission Particle Tracking. However this is a very slow method, which give little information at each step. It is better then to use particle tracking with fast camera, and possibly two cameras to get 3D tracking.

To simulate granular gas, there are two simulation methods: Molecular dynamics and Monte Carlo simulation, which can be found in[17]. In this thesis, we adopted the event-driven molecular dynamics algorithm, which is explained in Chap. 4.

1.6 Structure of the dissertation

now the outline of the thesis is presented as following: In Chapter 2, the current status of granular gases theories are recalled. In Chapter 3, we shall list exper-

imental results of 2D molecular dynamics in **micro-gravity** environment. In Chapter 4, the results of **2D molecular** of event-driven algorithm are discussed. In Chapter 5, the experiments of 2D vibrational granular gases **in a tilted plane** are explored. In Chapter 6, we will give some open question, discussions and conclusions.

Chapter 2

Research Progress on Granular Gases

2.1 Introduction

Because granular matter is characterized by local dissipation, still no satisfactory theory exists. Most granular theories are obtained from the local equilibrium and a modeling using continuum matter assumption. However, these ideas are not valid for the granular matter[68]. So we should restrict our attention to a rigorous scope of applications where the proposed theories can be valid. Such limits are not so well-known. In this chapter, we shall brief introduce the kinetic theory in non equilibrium system and the hydrodynamic equation applied to granular media.

We start in Sec. 2.2 the solutions of Boltzmann-Enskog equation used for the homogeneous cooling granular gas. In Sec. 2.3, the hydrodynamics theory is recalled. Then, we also introduce the hydrodynamics theory used for granular solids.

2.2 Boltzmann-Enskog Equation

Up to now, theoretical analysis of results [69–73] derived from Boltzmann equation for smooth inelastic hard spheres (IHS) is scarce. For instance, Wilkinson

and Edwards[74] studied the velocity distribution function (Vt) in the steady state of a Lorentz gas for an independent granular particle moving under gravity in a random array of fixed inelastic hard spheres used as scatters, driven by gravity[73]. These authors reduce the Boltzmann equation to a Fokker-Planck equation by assuming the velocity change remains small after collision, or assuming little inelasticity. The VDF is obtained in the form, $exp(-Av^4)$ with $A \sim \epsilon/g^2$, where $\epsilon = (1+\alpha)(3-\beta_1)/6$, β is empirical coefficients, α is the coefficient of restitution. Goldshtein and Shapiro[71] solved the Boltzmann-Enskog equation for the free evolving IHS(inelastic hard spheres) gas in the homogeneous cooling state assumption (HCS) by modifying the Chapman-Enskog method, using an expansion in Sonine polynomials. Esipov and Pöschel [72] obtained the following expression $\mathcal{A}exp(-Av/v_0(t))$ for VDF , showing the overpopulated tail of the velocity distribution. Sela and Goldhirsch [75] obtained a perturbation solution of the nonlinear Boltzmann equation by performing a (double) expansion in the Knudsen number and in the degree of inelasticity, which is used to explain the Burnett order. Noije and Ernst[73] studied the VDF in the free cooling and the uniformly heated case of IHS by Sonine polynomials based on the Enskog-Boltzmann equation. Ernst and Brito[76] obtained the solutions for the homogeneous nonlinear Boltzmann equation applied to inelastic Maxwell models under three different types of "thermostats" which are used to excite the granular gas: Gaussian, White noise and gravity field for the non-equilibrium steady state, So the theoretical results look numerous.

In this chapter, we shall look into the solution of the Boltzmann-Enskog Equation by an expansion of the case of HCS with a constant restitution coefficient ϵ. The method of perturbation will not be discussed here.

2.2.1 Chapman-Enskog approach for non-uniform granular gases

The construction of the normal solution for the Boltzmann equation is based on an expansion developed by Chapman and Enskog[77]. Its normal solution is function of the thermodynamic variables which are used to relate the fluxes to spatial derivatives of the thermodynamic variables. Let f_L denote the local

equilibrium distribution function, i.e. locally Maxwellian:

$$f_L = n(\frac{m}{2\pi\kappa T})^{3/2} exp[-\frac{m}{2\kappa T}(\vec{v}-\vec{u})^2] \tag{2.1}$$

Here n is the number density, $\vec{u}$ is the mean flow velocity and T is the temperature. All the parameters, like the thermodynamic variables, are derived from the velocity distribution f_L. We can replace the velocity distribution f by f_L, if these parameters still can be derived from f by the same form equation. For example, the number density

$$n = \int d^3v f_L = \int d^3v f \tag{2.2}$$

To get a better estimate of f, one can try to expend f as a function of f_L, and write as in the from:

$$f = f_L(1+\Phi) \tag{2.3}$$

When $\Phi = 0$, it represents the equilibrium distribution function (so at the 0th order). For the nonequilibrium case, $\Phi = \Phi^{(1)} + \Phi^{(2)} + \Phi^{(2)} + ...$ Then, for the first approximation, the cooling coefficient ς, and the transport coefficients, η, κ, μ can be obtained[69, 70, 77]. These parameters are in turn functions of the temperature, density and the microscopic parameters such as the size and mass of the particle and of the restitution coefficient. The hydrodynamic equations are completed.

We go further through an other step which is described in the next subsection.

2.2.2 Boltzmann-Enskog Equation and Sonine polynomial expansion for the homogeneous cooling gas

The Sonine polynomials is also called associated Laguerre polynomials. In the literature it is a technique used to solve the Boltzmann-Ensog equation through a set of approximations, which will be related now. This concerns the peculiar case of the homogeneous cooling state(HCS); it is assumed that, the velocity field vanishes after a long time, and the density n and the temperature $T(t)$ are spatially homogeneous, while the temperature decays in time[78].

To begin, we consider nonlinear Boltzmann equation for inelastic hard spheres.

There exist many ways to derive the Boltzmann equation[70, 78–80]. Here, the reference[70] is adopted. So the velocity distribution for an inelastic gas is:

$$\frac{\partial}{\partial t}f(\vec{v_1},t) = \sigma^2 \int d\vec{v_2} \int \vec{e}\,\Theta(-\vec{v_{12}}\cdot\vec{e})|\vec{v_{12}}\cdot\vec{e}|\times[\chi f(\vec{v_1}^{"},t)f(\vec{v_2}^{"},t) - f(\vec{v_1},t)f(\vec{v_2},t)] \equiv I(f,f) \tag{2.4}$$

where $f(\vec{v_1}$,t) is the velocity distribution of particles with velocity $\vec{v_1}$, $\vec{e}$ is the unit vector between the colliding pair of particles,$\vec{v_{12}}$ is the particles relative velocity ($\vec{v_{12}} \equiv \vec{v_1} - \vec{v_2}$, σ is distance between the colliding pair of particles); $\chi = \frac{1}{\epsilon^2}$ for the case the restitution coefficient $\epsilon = const$. $I(f,f)$ is the collision integral, f is the velocity distribution function. Θ is the Heaviside step-function,

$$\Theta(x) \equiv \begin{cases} 1 & for \quad x \geq 0, \\ 0 & for \quad x < 0. \end{cases} \tag{2.5}$$

Here, two approximations or hypothesis are used: (i) Binary collision is assumed. Three-body collision or more-bodies effects are ignored. (ii) The two-particle distribution function $f(\vec{v_1},\vec{v_2},\vec{r_{12}},t)$ is replaced by the product of two one-particle distribution $f(\vec{v_1},t)$ and $f(\vec{v_2},t)$, i.e; no correlation effect between particles. This is called the hypothesis of molecular chaos or Stoβzahlansatz. Enskog[69] suggests an approximation which accounts for a global homogeneous finite-volume effects; then the Boltzmann equation (2.4) changes to Boltzmann-Enskog equation:

$$\frac{\partial}{\partial t}f(\vec{v_1},t) = g_2(\sigma)I(f,f) \tag{2.6}$$

$g_2(\sigma)$ is the contact value of the equilibrium pair correlation function. In the slightly inelastic $\epsilon \lesssim 1$, the velocity distribution can be scaled by the following form[72]:

$$f(\vec{v_1},t) = \frac{n}{v_T^3(t)}\tilde{f}(\frac{\vec{v}}{v_T(t)}) = \frac{n}{v_T^3(t)}\tilde{f}(\vec{c}) \tag{2.7}$$

with the scaled velocity $\vec{c} \equiv \vec{v}/v_T(t)$. The thermal velocity $v_T(t)$ is defined by $T(t) = \frac{1}{2}mv_T^2(t)$.

With Eq.(2.7), $\frac{\partial}{\partial t}f(\vec{v_1},t)$ can be expressed as:

$$\frac{\partial}{\partial t}f(\vec{v_1},t) = (-\frac{3n}{v_T^4}\tilde{f}(\vec{c_1}) + \frac{n}{v_T^3}\frac{\partial \tilde{f}}{\partial \vec{c_1}}\frac{\partial \vec{c_1}}{\partial v_T})\frac{dv_T}{dt} \tag{2.8}$$

The collision integral may be written as

$$I(f,f) \equiv \sigma^2 n^2 v_T \tilde{I}(\tilde{f},\tilde{f}) \tag{2.9}$$

Using the time decay rate, $\tilde{f}$ satisfies the following equation:

$$\frac{\mu_2}{3}(3 + c_1\frac{\partial}{\partial c_1})\tilde{f}(\vec{c_1}) = \tilde{I}(\tilde{f},\tilde{f}) \tag{2.10}$$

In this situation, a closed Gaussian distribution for $\tilde{f}(\vec{c_1})$ is expected. We seek for the solution of Eq.(2.10) using the Sonine polynomials. A systematic approximation of the isotropic function $\tilde{f}(\vec{c_1})$ can be found by expanding in a set of Sonine polynomials, i.e.

$$\tilde{f}(\vec{c_1}) = \phi(c)[1 + \sum_{p=1}^{\infty} a_p S_p(c^2)] \tag{2.11}$$

where

$$\phi(c) \equiv \pi^{-3/2} exp(-c^2) \tag{2.12}$$

is the Gaussian distribution for the scaled velocity $\vec{c}$. The set of S_p satisfies the orthogonality relations

$$\int dc\phi(c)S_p(c^2)S_{p'}(c^2) = \delta_{pp'}\mathcal{N}_p \tag{2.13}$$

$\delta_{pp'}$ is the Kronecker delta and $\mathcal{N}$ is a normalization constant. The first few Sonine polynomials are

$$S_0 = 1 \tag{2.14}$$

$$S_1 = -x + \frac{1}{2}d \tag{2.15}$$

$$S_2 = \frac{1}{2}x^2 - \frac{1}{2}(d+2)x + \frac{1}{8}d(d+2) \tag{2.16}$$

where d is the space dimensionality. The coefficients a_p are polynomial moments of the scaling function:

$$a_p = \frac{1}{\mathcal{N}_p}\int d\mathbf{c} S_{p'}(c^2)\tilde{f}(c) \tag{2.17}$$

Now that the velocity distribution with small inelasticity is obtained, one can use Eq. (2.11) when the distribution is essentially a Maxwell distribution ($exp(-v^2/v_0^2)$) and if the series of Sonine polynomials converges rapidly. This means also that the whole set of approximations done to write Eq. 2.11 is correct.

An other question is to describe the tails of the distribution. This is described in the next subsection.

2.2.3 High energy tail

In the previous section, the velocity distribution is assumed Maxwell distribution ($exp - [v/v_0]^2$). However, the velocity distribution in granular gas differs from the Maxwell distribution in the low and high velocity part. In [72], an exponential velocity distribution function is predicted. For the large negative and large positive velocity part, this is called a velocity tail which is overpopulated (or overpopulated velocity tail), because $exp(-v/v_0)$ decreases slower than $exp - [v/v_0]^2$ at sufficiently large v. Hence, this needs to compare the asymptotic forms of the velocity distribution function(VDF) with the corresponding form of the Gaussian distribution, using a log-linear plot for instance.

For the low velocity part, the behavior of the kurtosis or some higher cumulants have to be studied. Here, we recall the work in ref. [72], starting from Eq. 2.9. So, in (Eq.2.9), the collision integral is

$$\tilde{I}(\tilde{f},\tilde{f}) = \int d\vec{c_2}\int d\vec{e}(-\vec{c_{12}}\cdot\vec{e})|\vec{c_{12}}\cdot\vec{e}|\times[\frac{1}{\epsilon^2}f(\vec{v_1}^{"},t)f(\vec{v_2}^{"},t) - f(\vec{v_1},t)f(\vec{v_2},t)] \tag{2.18}$$

$$= \int d\vec{c_2}\int d\vec{e}(-\vec{c_{12}}\cdot\vec{e})|\vec{c_{12}}\cdot\vec{e}|\times\frac{1}{\epsilon^2}f(\vec{v_1}^{"},t)f(\vec{v_2}^{"},t) - \int d\vec{c_2}\int d\vec{e}(-\vec{c_{12}}\cdot\vec{e})|\vec{c_{12}}\cdot\vec{e}|\times f(\vec{v_1},t)f(\vec{v_2},t) \tag{2.19}$$

So we have to evaluate when $c_1 >> 1$, and $\vec{c_{12}} \approx \vec{c_1}$. Moreover, the contri-

bution to the high velocity from the first term of (Eq.2.19) is small. So the first term of (Eq.2.19) can be neglected. Using the normalization

$$\int \tilde{f}(\vec{c_2})d\vec{c_2} = 1 \tag{2.20}$$

and the integral

$$\int d\vec{e}\Theta(-\vec{c_1}\cdot\vec{e})|-\vec{c_1}\cdot\vec{e}| = \int_0^{2\pi} d\varphi \int_{\pi/2}^{\pi} sin\theta cos\theta d\theta = \pi \tag{2.21}$$

The collision integral can be written:

$$\tilde{I}(\tilde{f},\tilde{f}) \approx -\pi c_1 \tilde{f}(\vec{c_1}) \tag{2.22}$$

Then, with Eq (2.22), Eq (2.10) reduces to :

$$\mu_2 \tilde{f}(\vec{c_1}) + \frac{1}{3}\mu_2 c_1 \frac{d}{dc_1}\tilde{f}(\vec{c_1}) = -\pi c_1 \tilde{f}(\vec{c_1}) \tag{2.23}$$

For $c_1 >> 1$, we obtain

$$\frac{d\tilde{f}}{dc} = -\frac{3\pi}{\mu_2}\tilde{f} \tag{2.24}$$

The velocity distribution becomes finally:

$$\tilde{f}(c) = \mathcal{A}exp(-\frac{3\pi}{\mu_2}c) \tag{2.25}$$

Comparing with the Maxwell distribution $exp(-c^2)$, the overpopulation of the high velocity occurs when the coefficient of the exponentials i. e. $(-\frac{3\pi}{\mu_2}c)$ in Eq. (2.25) is larger than $-c^2$. Since μ_2 introduces a factor $1-\epsilon^2$, the overpopulation takes place for $c \gtrsim 1/(1-\epsilon^2)$. Brey et al.[81] find this theory agrees well with the simulation results. They use it for the homogeneous cooling state theory.

In the case of experiments, one finds an exponential velocity distribution in the case of dilute granular gas experiment in micro-gravity[82]. More, Losert[52] presents the experimental velocity distributions described by $exp(-|v/v_c|^{1.5}$ for a large range of parameters.

From experiments from our team, we found $exp-v/v_o$ distribution in the low

density regime[82, 83]. However, it is not needed to discuss further these tails , since we will have to discuss other more surprising results in this dissertation. So we come now to the description using hydrodynamics modeling.

2.3 Hydrodynamic theory

The hydrodynamics equations for a gas of hard spheres with dissipative dynamics can be derived from the Boltzmann equation. We follow [84].

Granular gas is treated as a continuum of matter[85]. Though there is a great difference between granular systems and simple fluid, we can consider this approximation as valid, at least in a first step, and find the statistical limit with the condition of small spatial gradients of temperature and density everywhere. Then, this allows to write the Granular Gas satisfies four conditions: $(i).\vec{\nabla}T \sim \frac{T}{L}$, $L \gg l$, where L is the characteristic lengths, l is the mean free path. This point ensures the slightly spatial gradient of the temperature. (ii) The same as (i) for the number density. $\vec{\nabla}N \sim \frac{N}{L}$, $\quad L \gg l$. (iii) The velocity of macroscopic flow $\vec{u} \ll \sqrt{< v^2 >} \sim \sqrt{T}$. (iv). The characteristic time $\tau_c \ll L/u$.

Since the system preserves the conservation of mass and momentum for the granular matter, the balance equations for the mass and momentum still hold on. We need another equation to close the problem. This one corresponds to the energy (temperature) change. We need to add an energy sink term every where in the sample to mimic the energy losses. Then the hydrodynamic equation for the granular gas can be obtained:

$$\frac{\partial n}{\partial t} + \vec{\nabla} \cdot (n\vec{u}) = 0 \tag{2.26}$$

$$\frac{\partial \vec{u}}{\partial t} + \vec{u} \cdot \vec{\nabla}\vec{u} + (nm)^{-1}\vec{\nabla} \cdot \hat{P} = 0 \tag{2.27}$$

$$\frac{\partial T}{\partial t} + \vec{u} \cdot \vec{\nabla}T + \frac{2}{3n}(\hat{\mathbf{P}} : \vec{\nabla}\vec{u} + \vec{\nabla} \cdot \vec{q}) + \zeta T = 0 \tag{2.28}$$

Here, $n(\vec{r}, t)$ is the local number density field , $\vec{u}(\vec{r}, t)$ is the local average velocity field, or the local flow velocity, $T(\vec{r}, t)$ is the temperature field, $\hat{\mathbf{P}}(\vec{r}, t)$ is the pressure tensor, m is the mass, $\zeta(\vec{r}, t)$ is the cooling coefficient.

For the steady state, since $\vec{u}(\vec{r},t) = 0$ and all parameters are not changing with time(steady state), these equations can be written in the form

$$\nabla \cdot \hat{P} = 0$$

$$\frac{2}{3n}\vec{\nabla} \cdot \vec{q} + \zeta T = 0$$

This is the hydrodynamic model for granular gas. However, the question whether this hydrodynamics modeling applies really to granular media or not is still the center of current debate[12, 86].

2.3.1 The pressure

The kinetic definition of the pressure tensor[70] is:

$$\hat{\mathbf{P}}(\vec{r},t) \equiv \int m(\vec{v}-\vec{u})(\vec{v}-\vec{u})f(\vec{r},\vec{v},t)d\vec{v} \tag{2.29}$$

where u is the mean flow and v is the speed of gas particles. P is a scalar because pressure is assumed isotropic. However P can be a diagonal stress tensor in an adequate frame when the gas is anisotropic, with different values of the diagonal terms. (It is isotropic only when diagonal terms are equal[12, 70].

Anyway, pressure is the transport of momentum since it is the flow of the relative moment m$(v-u)$.

If one considers the Navier-Stokes approximation, the pressure tensor can be written

$$\mathbf{P}_{ij} = p\delta_{ij} - \eta(\nabla_i u_j + \nabla_j u_i - \frac{2}{d}\delta_{ij}\nabla \cdot \vec{u}) \tag{2.30}$$

where $p = nk_BT$ is the hydrostatic pressure, η is the shear viscosity. For the steady state, the above equation reduces to the classical equation $p = constant$.

There are two mechanisms involved in the transport of momentum: (i) The movements of free particles lead to the momentum transfer. Here, "free" means that no collision happened in between the particles during the considered time T. (ii) the collision process participate to the transport of momentum. For the dilute granular gas, the frequency of collision can be neglected, assuming that the time T is negligible. However, this is not true for non-dilute and inelastic

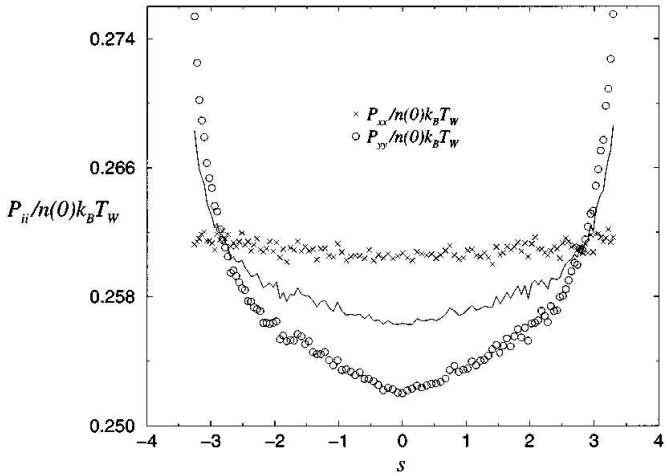

Figure 2.1: Profiles of the diagonal components of the pressure tensor P_{ii} in the steady state for $\alpha = 0.95$. The solid line is the calculated hydrodynamic pressure p. T_w is the temperature of the wall in x direction with a periodic excitation boundary condition in y direction[12].

granular gas, such as, when strong dissipation occurs in the dilute granular gas, or when one considers slightly inelastic granular matter with intermediate density; in such cases, the collision effect cannot be neglected.

Fig. 2.1 of [67] shows, the diagonal components of the pressure tensor P_{ii} in the steady state. P_{ii} was expected to be isotropic and constant from the hydrodynamics modeling; it is neither isotropic, nor constant, nor even linear.

Ref.[12]simulates a granular gas, which is generated using sawtooth driving.. But unlike [67], the collision process is added into the pressure tensor; in this case one gets Fig. 2.2. Here, ρT_x is P_{xx}, and σ_{xx} is calculated from two parts:(i) one is the kinetic part which is the same with the P_{ii}(Eq.2.29). (ii)The other is interactions between the particles. This part gives

$$\sigma_{ij}^{int}(\mathbf{r},t) = \frac{1}{\Delta t}\frac{1}{|V_r|}\sum\nolimits_{t_n}\sum\nolimits_{k_n} l_i^{k_n}(t_n)\Delta p_j^{k_n}(t_n) \tag{2.31}$$

where l_i^k is the half distance between the colliding pairs (when masses are equal), $\Delta p_j^{k_n}(t_n)$ is the jth component of the change of momentum of particle k during this collision. V_r is the small volume element located at $\mathbf{r} = (x, y)$. Δt is the small time element $[t - \Delta t, t]$. This statistical method uses the method of coarse

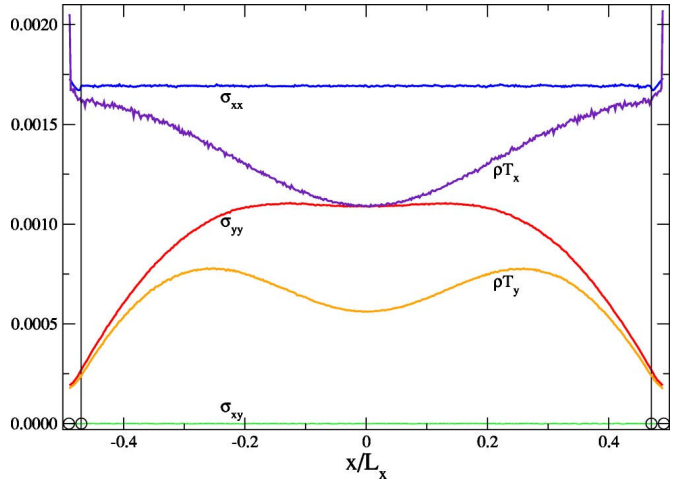

Figure 2.2: Spatial profiles of the stress tensor components σ_{xx}, σ_{yy}, ρT_x, ρT_y. Here ρT is the " hydrostatic pressure", σ_{xx} is the stress tensor which is described above. The restitution coefficient $e = 0.9$, the box size is $50 * 25$. $N = 240$, particle diameter $d = 1$.

grain measurement[87]. We can observed from (Fig. 2.2), that the stress tensor (the pressure tensor) in the vibrating direction is linear in a large part of the cell, which makes the " pressure tensor" satisfied (Eq. 2.30).

It seems Eq.2.27 still holds for strong dissipation when the second mechanism is considered[12].

2.3.2 The temperature

For a homogeneous flow, the temperature is defined as:

$$\int \frac{1}{2} m v^2 f(\vec{v}, t) d\vec{v} = \frac{3}{2} nT \tag{2.32}$$

when mean of v is 0. However, the concept of temperature in granular matter remains controversial[88–90]. This concept has been used since 1978 at least[91] to measure the velocity fluctuations in the granular gas. Temperature is a concept of equilibrium system. However, we know that granular system already deviate from equilibrium thermodynamics state due to the dissipation of inelastic collision and energy input, and due to memory effect. A typical example where the temperature concept broken is found for mixture of two kinds of particles[92]. Also,

Evesque[88] question whether the vibrator is generating or not a " thermal agitation" but some " velocity agitation". In other words, does the exciting boundary play the part of a " velostat"[93]. In a simple approach, he demonstrates that granular gases violate the classic laws of the kinetic theory of gas.

Baldassarri[89] discusses the thermodynamical concepts, especially the temperature concept based on the fluctuation-dissipation theorem, in different cases: dense, liquid-like and gas-like behaviors of granular media. However, the very possibility of consistently constructing a thermodynamics is doubtful due to the energy lost.

Some other papers also doubt about the granular temperature [40, 94]. Some others try to avoid to use this concept in their theory[95].

Anyway, now we introduce the temperature of the granular gas. In a steady state[12], the total kinetic energy fluctuates with space and time around a time-independent mean value. Assuming the velocity distribution is $f(\vec{r}, \vec{v})$, two components granular temperature(2D) are defined:

$$T_{i=x,y}(\vec{r}) = \frac{m}{\rho} \int_{\mathbb{R}} dv_x \int_{\mathbb{R}} dv_y f(\vec{r}, \vec{v})(v_i - U_i(\vec{r}))^2 \tag{2.33}$$

where $\mathbb{R}$ stands for the small cell volume located at $\vec{r}$, ρ is the particle density, $U_i(\vec{r})$ is the mean velocity field:

$$\vec{U}(\vec{r}) = \frac{1}{\rho(\vec{r})} \int_{\mathbb{R}} dv_x \int_{\mathbb{R}} dv_y f(\vec{r}, \vec{v})\vec{v} \tag{2.34}$$

Total temperature is $T(\vec{r}) = [T_x(\vec{r}) + T_y(\vec{r})]/2$. $U_i(\vec{r}) = 0$ in the stationary state, hence, the temperature is obtained succinctly, like $T_x =< \sum(v_x^2) >$.

We shall note at this stage that time average of these variables has to be defined, which may be difficult in the case discussed in the present dissertation (see Chap. 3 and 4). But we shall stop here the discussion. Next focuses on the hypotheses which are used for deriving the above equation.

2.4 A stochastic model

In this section we mention other modeling which looks easier, compared to the previous ones for which correct description is questionable too, and whose solutions are difficult to obtain, for instance as the exact solution of Boltzmann equation. So in[96, 97], a solvable stochastic model of dissipative granular gases was introduced with a granular gas heated by a bath from below. The papers presume that each particle is only described by its energy and its momentum and that spatial variables are eliminated. Using an inelastic collision, the stochastic evolution of the particle energy is given. Finally, the papers find the high tail of the energy distribution, which is exponential distribution.

Question remains: can we make such crude assumptions and hope still to be correct and describe the real complexity.

2.5 Granular Solid Hydrodynamics

We turn now to an other attempt to a new description for granular system called the Granular Solid Hydrodynamics (GSH). It has been developed by Mario Liu and Yimin Jiang[98] starting from classical thermodynamics principle and tempting to generalise them to system out of thermal equilibrium, in the Prigogine flavour. So, in this part, we recall main points of this GSH theory.

In classical thermodynamics, a system out of equilibrium but in local equilibrium, which flows J and the set of forces X satisfied the linear relationship of the kind:

$$J_k = \sum_l L_{kl} X_l \tag{2.35}$$

as shown by Onsager. Here $X_l = -(\frac{\partial \Delta S}{\partial \alpha})$, $J_k = \frac{d\alpha}{dt}$, S is the entropy and α is the fluctuation. The proportionality coefficients between flows J and forces X are denoted by L. For example, the Fourier Law expresses the linear relation between heat flux and gradient of temperature. There are three limits for the proportionality coefficients L_{kl}. Firstly, the second law of thermodynamics makes L_{kl} to be a positive definite matrix. Secondly, Curie-Prigogine principle gives the spacial limit for L_{kl}. Thirdly, Onsager[99] obtained the symmetry of the matrix,

$L_{kl} = L_{lk}$ based on the time reversibility of microscopic dynamics. To apply Onsager reciprocity relation to granular media, it is not obvious. Paper[98] is a model approximation[98] to be used for granular media. But, due to inelastic collision, the dynamics is indeed irreversible. So the approximation is as crude as the assumption of local equilibrium which is used in granular matter in the all the above sections. This needs to be recalled as an advertisement before the description of the model.

Here, we firstly discuss the strain field of granular matter. There are two parts of strains according to classic mechanic point of view: $\epsilon_{ij} = u_{ij} + p_{ij}$, where ϵ_{ij} is the total strain, u_{ij} is the elastic strain and p_{ij} is plastic one. The elastic one u_{ij} is reversible and p_{ij} is non reversible. We denote σ_{ij} is the total stress, π_{ij} is the stress part due to elastic strain. $\partial_t(\rho v_i) + \nabla_j \pi_{ij} = 0$. The granular system can reach a state $\partial_t \epsilon_{ij} = 0$ if running enough time, otherwise we shall note $\partial_t \epsilon_{ij} = \partial_t u_{ij} + \partial_t p_{ij}$. So we obtain $\partial_t p_{ij} = -\partial_t u_{ij}$. In granular gas the elastic part ∂u_{ij} shall relax due to dissipation after a long time, nd the stress shall go to 0, according to some finite relaxation time. So $\partial_t u_{ij} = -u_{ij}/\tau$, and τ is a constant and $\int (u_{ij}/\tau) dt \approx 0$.

2.5.1 Macroscopic relations:

In the second step, granular temperature, granular entropy and the free energy shall be described.

i) *Granular temperature* is firstly introduced by[85]. It comes directly from the analogy with a molecular gas, i. e. $T_g = w_{kin}$. So we shall obtain $T_g \equiv \partial w_{kin}/\partial s_g \sim \partial T_g/\partial s_g$, $s_g \sim lnT_g$.

ii) It is assumed that the conserved energy density w is related to the entropy s, to the mass ρ, and to the momentum g_i, so $w(s, \rho, g_i)$. For simplicity, w can be separated: $w(s, \rho, g_i) = w_0(s, \rho) + g_i^2/(2\rho)$. Here, w_0 is energy in the frame at rest. For a granular medium, we shall assume that strain is independent to density. Or in other words, density can change with the same deformation(u_{ij}).So we need to add a new variable for w_0, $w_0(s, \rho, u_{ij})$. So $w_0(s, \rho, u_{ij}) = Tds + \mu d\rho - \pi_{ij} du_{ij}$.

Looking from another way, all the microscopic is generally subsumed as a

global variable. Let us consider Tds, so $dw_0 = Td(s - s_g) + T_g ds_g = Tds + (T_g - T)ds_g$. The free energy is defined as $f \equiv w_0 - Ts$. When $s_g = 0$, the system is in equilibrium and the free energy reaches a minimum. We can expand this quantity using Taylor expansion at $s_g = 0$, so

$$f = f_0(T) + s_g^2/(2b\rho) \tag{2.36}$$

where b is material parameter.

$$\partial f/\partial T = T_g - T = s_g/(b\rho) \tag{2.37}$$

We also define $\bar{T}_g = T_g - T$, so,

$$\tilde{f}(T, \bar{T}_g) = f_0(T) - b\rho \bar{T}_g{}^2/2 \tag{2.38}$$

Where $\tilde{f}$ is the potential obtained from Legendre transformation.

iii) *granular entropy.* we also introduce the granular entropy s_g in the following way. The movement of grains can be divided into two parts: the large-scaled smooth velocity and small-scaled mesoscopic one. The first one is the so-called "hydrodynamic variable" of , i.e. the "macroscopic" local velocity and the second one corresponds to the stochastic motion of grains. We use a granular temperature T_g to describe the second part. T_g is based on the transiently elastic granular matter. From the granular temperature concept, a granular entropy should be defined. The equation of variation for s_g should contain a convective and a diffusive term.

$$-\partial s_g = \nabla_i[s_g v_i - k_g \nabla_i \bar{T}_g] + \gamma \bar{T}_g \tag{2.39}$$

2.5.2 GSH set of equations:

The third step needs to complete GSH equations. There are three parts:

i) *The motion equation of the state variable*:

$$d_t \rho = -\rho v_{kk} \tag{2.40}$$

$$d_t\vartheta = \frac{R}{\rho T} + \frac{\nabla_k f_k}{\rho} \tag{2.41}$$

$$d_t v_i = g_i - \nabla_j \frac{\sigma_{ij}}{\rho} \tag{2.42}$$

$$d_t u_{ij} = v_{ij} - u_{ij}\nabla_j v_k - u_{jk}\nabla_i v_k - \frac{\nabla_j Y_i + \nabla_i Y_j}{2} + Y_{ij} \tag{2.43}$$

$$d_t \sigma_g = \frac{R_g}{\rho T_g} + \frac{\nabla_k f_k^2}{\rho} - \frac{I}{\rho} \tag{2.44}$$

This set of Eq. (2.40 to 2.44) contains the continuity equation, Newton equation, the entropy law parts and the strain geometric equations with dissipation.

ii) *Energetics identical equation and Onsager relations*: stress, thermal entropy and granular entropy production.

$$\sigma_{ij} = \rho^2\mu_1\delta_{ij} + \pi_{ij} - 2u_{ik}\pi_{kj} - \sigma_{ij}^{(1)} - \sigma_{ij}^{(2)} \tag{2.45}$$

$$R = f_k\nabla_k T + \sigma_{ij}^{(1)} v_{ij} + Y_I\nabla_j\pi_{ij} + Y_{ij}\pi_{ij} + IT_g \tag{2.46}$$

$$R_g = f_k^{(2)}\nabla_k T_k + \sigma_{ij}^{(2)} v_{ij} \tag{2.47}$$

Elastic stress, chemical potential, two entropy energetics identical equations:

$$\pi_{ij} = -\rho\frac{\partial\mathcal{F}}{\partial u_{ij}}, \mu_1 = \frac{\partial\mathcal{F}}{\rho}, \vartheta = \frac{\partial\mathcal{F}}{T}, \vartheta_g = \frac{\partial\mathcal{F}}{T_g} \tag{2.48}$$

Onsager relation:

$$f_i = \kappa\nabla_i T_g \tag{2.49}$$

$$\sigma_{ij}^{(1)} = \eta v_{ij}^* + \zeta v_{kk}\delta_{ij} + \alpha_s\pi_{ij}^* + \alpha_v\pi_{kk}\delta_{ij} \tag{2.50}$$

$$Y_i = \beta\nabla_k\pi_{ik} \tag{2.51}$$

$$Y_{ij} = -\alpha_s v_{ij}^* - \alpha_v v_{kk}\delta_{ij} + \lambda_s\pi_{ij}^* + \lambda_v\pi_{kk}\delta_{ij} \tag{2.52}$$

$$I = \gamma T_g \tag{2.53}$$

$$f_i^2 = \kappa_2\nabla_i T_g \tag{2.54}$$

$$\delta_{ij}^{(2)} = \eta_2 v_{ij}^* + \zeta_2 v_{kk}\delta_{ij} \tag{2.55}$$

iii) *The free energy*:

$$\mathcal{F} = CT + B\frac{\Delta}{\rho}(\frac{2}{5}\Delta^2 + \frac{1}{\xi}u_s^2) - \frac{b}{2}T_g^2 \tag{2.56}$$

So, this is the way to introduce the granular entropy s_g, based on the Onsager relations, GSH equations. It contains three parts: the equation of motion of state variables, Onsager relations, the material model.

2.6 Discussion

In conclusion, there are still no satisfying theories which can describe granular gases except for under conditions of near-elastic and low volume fraction. Granular gases are unique and need to be treated carefully. This is what we want to demonstrate with this dissertation. The following Chapters will present our results in micro-gravity; this will show that the granular gases characteristics do not obey the classical theory, and that the pressure itself is not isotropic, nor so simple to define. While in Chap. 5, experiments will be conducted in a 2D horizontal experimental set-up. Their results will show up similar behaviors, confirming the discrepancy. The rest of this chapter 5 is dedicated to experiments using 2D inclined setup study the changes linked to small gravity effect, and their changes with the effective gravity. We report in Chapter 4, 2D simulations in 0g which were undergone to conclude on the validity of these discrepancies; they will show that normal gas behavior can be reproduced when dissipation by collision is reduced to zero, but that the discrepancies appear as soon as dissipation increases from $(1 - e) = 0$ to some small value. Moreover, we will demonstrate that our experimental results in $0g$ can be reproduced by appropriate values of effective collision losses, and that all these data depend on the real motion and excitation at boundaries. This confirm previous 3D results from R.Liu simulations in his stay at ECP.

Chapter 3

Experimental results on vibrated granular matter in micro-gravity

3.1 Introduction

3.1.1 Historical background

The advantages to study experimentally granular materials under microgravity are liked to the removing of the effects of gravity, to void the concentration of grains on the bottom side and then avoiding the friction between particles and the baseboard. A model of 2D vibrating granular gases is perhaps simplified, but microgravity condition is so hard to achieve, that it may be used as a first step. As a matter this was not the first step for the French team (P. Evesque, Y. Garrabos, E.Falcon and S.Fauve for which first flight was 1998)) nor for the Chinese one (M.Hou, P.Evesque, satellite in 2006); but the topic is so hard to understand. This topic is found necessary to restart with a simplified 2D devise.

There are only several methods to obtain a microgravity circumstance. They all use free-fall concept, but the technique can be different: the easier and more expensive, is to use rocket or satellite flight out of earth atmosphere, or free-fall flight from a tower or in a mine. A third one is to use a plane as the A300-0g of Novespace, and to undertake parabolic flight, where the pilot adjusting the engine power to counter balance the aerodynamic forces. Here are some references, for experiment in outerspace[9, 82] or in the Airbus parabolic flight experiment[13,

100], a last one is the magnetic field[57] using diamagnetic materials to counter balance gravitation, but this last method can not work on a whole volume, but only on a small surface. So, the experimental results in microgravity are scarce. Falcon[9] et al. firstly reported what the authors considered at that time as cluster formation of a granular medium, fluidized by vibration in low gravity. In fact, it took a long time to understand the real meaning of the results, since repeating the experiments in such conditions is hard and asking the good questions is hard too. This led the French team to perform a series of experiments using rockets (MiniTexus 5, Maxus 5, Maxus 7) and parabolic flight (from 2000 to 2011).

At this stage it is worth mentioning also other pioneering space experiments such as the series of triaxial test experiment made by NASA to characterize the behavior of pile under low compression and "low" density conditions, which required to use the space shuttle to generate constant, long time stability of microgravity.

Coming back to granular gas physics, common spatial French-Chinese project has allowed Hou and Leconte[82, 83] et al. investigated the velocity distribution of vibration granular gas in Knudsen regime in micro-gravity. An exponential distribution, i.e. $exp(-v/v_o)$, was found in directions parallel and perpendicular to vibrating direction through few different studies[83]. An other group Grasselli[100] et al. also studied the free cooling process in a vibrated granular matter in micro-gravity with Airbus where it was found that the energy decay was much faster than the theoretical predictions. In this chapter[13, 101, 102], we present some small part of the experiments performed with Airbus. They concern the 28/3/2006 Airbus flight of the ESA campaign, which was the first Chinese French Airbus campaign on granular matter, starting the collaboration through VIP-Gran ESA Topical team. This happened as following: At the end of 2005, O. Minster (ESA) went and visited China, explaining ESA activities. This leads Prof Hou to e-mail Dr Evesque late in December about some possible advice for their next experiment on satellite (Sept.2006). After some discussion in between Christmas and the new year, the idea of collaboration was set up with the filling of few cells in "SJ-8". Esa supported this idea inviting the Chinese team to its next Airbus campaign.

It is then remarkable that this first collaborative experiment was so much

fruitful, as we will discuss in this chapter 3. However, this appeared obvious only on 2009, after the R.Liu's simulations, which were found to be supported by these Airbus experimental data. We shall remind also that it has not been the only surprise we got during this investigation, among which we shall quote: (i) the behaviour of dense systems in "SJ-8" which do not move (we thought at the beginning it was an artefact, but it was not as discussed in the film "un chercheur-une manip" at the Palais de la Découverte (February-April 2008, in French); we have been surprised also by the exponential distribution we got in Knudsen regime, and by the behaviour of 1 or 2 particles whose motion becomes coherent with the cell motion (i.e. merely locked in phase) at large amplitude of vibration; this shows a strong diminution of the phase space dimensionality.

3.1.2 Micro-gravity experiment

This Chapter reports on our experimental observations obtained in Airbus of *Novespace* (2006 Campaign) in a 2D vibro-fluidized granular system. This experiment was developed by CNES and performed in collaboration with Yves Garrabos' group. It was part of a larger series of experiments, starting with the investigation of 1-ball behavior,..., to achieve correct definition for next experiment to be flown under ISS or Chinese satellite. It turns out that we need to focus on this special experiment made (in 2006) because it shows different and important results, as detailed below. Indeed the understanding of the importance of these experiments came much later than 2006, i.e. about 2010, after the PhD long stay of R. Liu at ECP and after the results he obtained there.

In this experiment, the particle velocity distributions are obtained in both x and y directions, globally and locally. It is found that the probability distributions of velocities both along (v_y) and perpendicular to (v_x) the vibration direction are exponential and symmetric, when taking into account all the particles. However, when the particles are divided into different long bins, the length of which are oriented perpendicular to the vibration direction, the local velocity distribution of (v_y) is found to deviate measurably from a symmetric one. Considering that the distributions of local velocities are asymmetric, we measure the "hydrodynamic" profiles for positive and negative components in accordance with the sign

of velocity components. It is found these two components, positive and negative, of p_y, n_y and T_y differ not only at the boundary layer but also in the whole cell. This demonstrates the long effect of the combination of boundary excitation and of dissipation. But, besides the extensive boundary effect, particles are found to be inhomogeneous distributed and the distribution of particles depends also on the direction v of motion but also on the way ($+v$ vs. $-v$). So we had to define not only a granular temperature or a granular pressure, which depends on the considered way ($+$ or $-$). It means in other word, that the granular temperature (pressure) is no more a symmetric tensor but a asymmetric one (with some anisotropy between x and y)

The outline of this Chapter 3. is as follows: firstly, we present the experimental method, we then show the local velocity distributions, which are asymmetric in the y direction; finally, local hydrodynamic parameters are investigated. Table 3.1 reports the experimental vibration parameters, as a function of the time at which each parabola happened. The micro gravity duration is 20s for each, with some larger g-jitter at the beginning and at the end, so that we used only the 16 s of middle for which we can consider $gravity = (0.00 \pm 0.05)g$ about. We repeated experiments twice, one to follow the grains during the whole parabolic with 30 fps (frame per second), the other one using the fast camera at 1MPixels resolution with 499 fps with a 1s interval recording. Only this last one was used to extract speed and position information with time. The recorded time in the fast mode was only 1s, that limited the number of the data series. The cell used is made of 4 cells. Only the dynamics of the two top of these cells containing either 47 or 63 bronze balls, were investigated. These cells are recombined like in Fig. 3.1. Their dynamics were recorded at the same time, but were studied independently.

3.2 Experimental Setup

In this section, the experimental method is presented. A quasi-2D quadrate cell (side walls in aluminum, front and back walls in glass, V=10mm *10mm *1.4 mm) containing several bronze spheres is driven in y direction by a sinusoidal oscillating shaker. A snapshot is shown in Fig.3.1. The diameter of the bronze

Time	f **(Hz)**	A **(mm)**	Γ (m/s^2)	V_ω (m/s)
10H12	49	0.2275	21.6	0.07
10H21	97	0.07329	27.22	0.04
10H24	97	0.1111	41.28	0.07
10H27	49	0.1237	11.7	0.038
11H03	97	0.1443	53.60	0.087
11H20	97	0.0792	29.42	0.048
11H26	126	0.08386	52.56	0.066
11H44	39	0.18347	11.01	0.0449

Table 3.1: The driving parameters in the Airbus experiment (28/03/2006). Here, notations (A, V_ω, Γ, f) to represent amplitude, vibrating peak velocity, acceleration and frequency, respectively.

spheres is 1.21mm ± 0.02mm. The spheres can rotate in three dimensions but only have two dimensional translational motions.

The cell is fixed on a V455 LDS shaker, which vibrates in the y direction. The vibration controller is the same as the one in previous works [82]. The movement of the beads is recorded by a fast camera (499 fps). The LEDs are mounted in the reverse side of the cell to increase the contrast between beads and the background. The experiments are performed for 30 parabolic flights in a 2-hour Campaign. Each parabolic flight has about 20s for micro-gravity (0.0 g± 0.05 g). Within the 20s of each parabolic flight only one second is recorded by the fast camera. The resolution of the cell image is 288 pixel* 288 pixel, i.e. 1 pixel= 0.035mm. In this dissertation, several sets of data with different vibrating conditions were selected to be studied; they are listed in Table(3.1). We use notations (A, V_ω, Γ, f) to represent amplitude, vibrating peak velocity, acceleration and frequency, respectively.

In the table all the parameters are determined by image analysis using the software *ImageJ*. Images recorded by the fast camera are firstly processed to get the positions of bead centers, which are calculated through the ultimate eroded points(UEPs) in the Euclidean distance map(EDM). Afterwards, particles are tracked using the program of minimum-distance algorithm. Since our system has moderate number density, the spheres can not move extensively, the minimum-distance algorithm can work well in our case. The accuracy obtained in this way

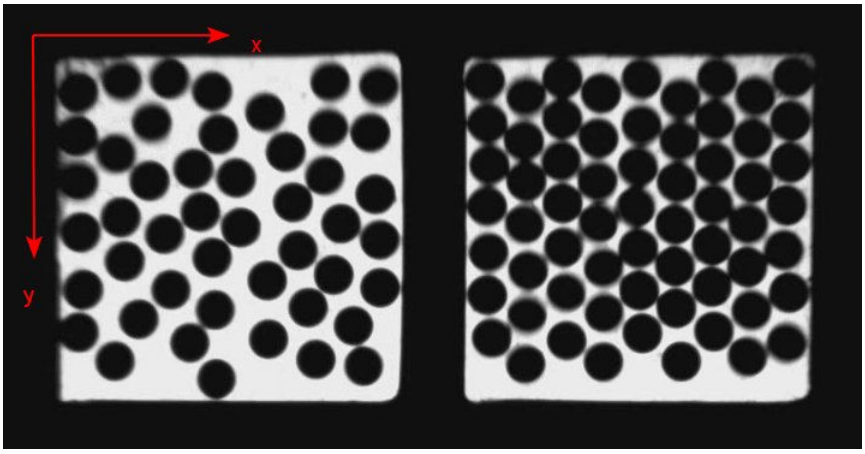

Figure 3.1: Snapshot of the two top cell particles. The cell contains 47 and 63 bronze sphere particles, driven in the y direction at various vibration parameters(A, V_ω, Γ, f), which is listed in the table(3.1).

reaches $0.01mm$. The particle velocities are obtained from 499 image sequences within 1 second; it means also a speed accuracy of 5- 10mm/s.

3.3 Velocity distribution function

3.3.1 The global velocity distribution function

Warr et al.[103] first measured the velocity distribution function using a high speed camera. Due to technical limitations, deviations from a Gaussian was not shown. Over time and the development of the experimental technique, a stretched exponential law was reported by other teams afterwards. That means:

$$P(v) \propto exp(-|v/v_0|^\nu) \tag{3.1}$$

where ν is a parameter[54, 55], that depends on the author. In particular, ν is found close to 3/2 in experiments[52, 53, 104].

As far as we know, there are several factors influencing the shape of the velocity distribution which have been discussed in the previous works: the heating mechanism, the number density (the area fraction), the restitution coefficient, the granular temperature (the vibration parameter), the ratio between the average

number of heating and the average number of collisions in the granular gas $q = N_H/N_C$. Factors such as the number density and the restitution coefficient will be discussed in the next chapter since it is easier to study them from simulations. We shall discuss the other factors in the following part.

We first look at the heating mechanism[105, 106]. To describe a vibrating granular system, the heating mechanism must be specified for several reasons. Granular materials characterize kinetic-energy dissipation. This requires continuous energy injection to sustain a steady state. Accordingly, heating mechanism (energy input) is crucial for studying the granular system. Under different heating mechanisms, the systems yield different results[56, 64]. In [56], results of two kinds of particle, segregated in two layers, and vibrated vertically are displayed for a wide variety of driving and density parameters. The heavier balls, which lay on first layer, which are directly driven by the vibrator, shows non-Gaussian velocity distribution, whereas in the second layer, lighter ball overlayed on top of heavier-balls and are driven by the heavy-ball layer ; these lighter balls exhibit more Gaussian statistics. In [64], they found Gaussian distribution for the uniform heating and non-Gaussian velocity for boundary heating. In [12], the velocity distributions of particles in the center area of the box seems more Gaussian-like than the results of particles in the entire box.

In [53], the shape of the distribution does not change when varying the number density from the average aerial density. Note that in these experiments, velocity distribution is measured only in a rectangular window which is located in the middle of the cell. The simulation results of [12] show a value of the exponent ν which is independent of the global area fraction. However, in[107], the experimental results indicates that, the velocity distribution curves deviate from Gaussian when increasing the number density of particles. Then, it seem conflicting results. We believe this conflict derived from the boundary effect since reference [53] does not consider the boundary area but the paper [107] does consider it.

In our work here, the local velocity distribution will be used to understand the importance of the boundary layer.

The value of the exponent ν seems to depend on the restitution coefficient e, and falls in the range $1.2 < \nu < 1.6$ [63]. In [108], a random restitution coefficient model is proposed. Rouyer et al.[53] found the distribution was determined

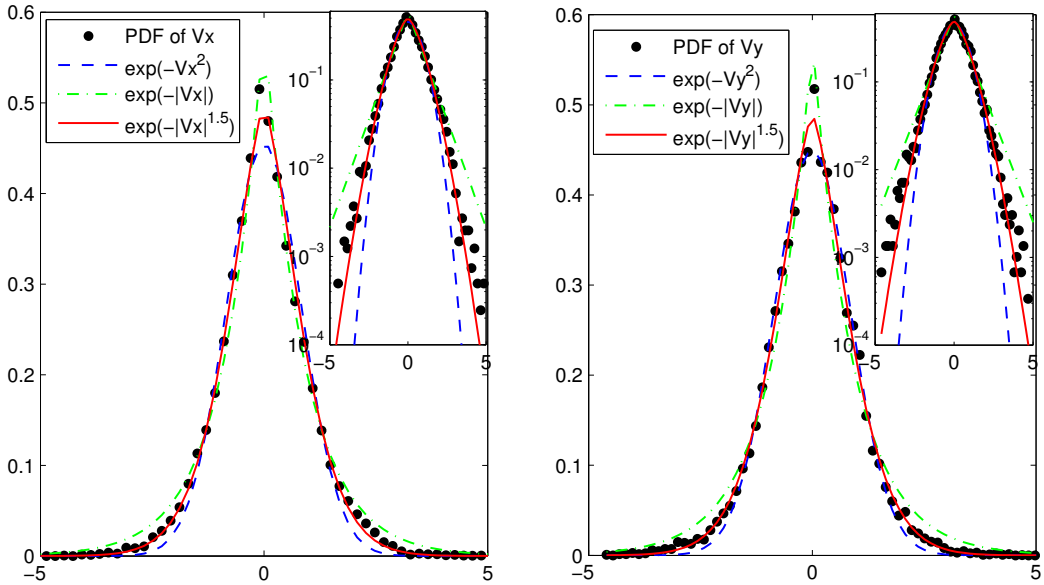

Figure 3.2: The global velocity distributions of different components v_x and v_y. Here, y is the vibration direction. v_x is scaled by v_c^x $(0.041m/s)$. v_y is scaled by $v_c^y = 0.057m/s$. $N = 47$. The area fraction are 0.536.

completely by a single parameter: the granular temperature. The form of the velocity distribution is governed primarily by the restitution coefficient e and by the ratio q between the average number of heating N_H and the average number of collisions N_C in the granular gas, $q = N_H/N_C$.

A clear explanation of the conflict between experiments and theories seems to be found in[109]. In the theory, velocity distribution is assumed to be locally Gaussian[108, 110–114]. In particular, $\nu = 3/2$ is obtained analytically[73, 76?], which is based on a "Stochastic thermostat" homogeneously driven by white noise. Though $\nu = 3/2$ is deduced from theory, it is worth comparing the heating mechanism between experiments and theories: it is not possible to confess the agreement between theoretical analysis and experimental results reached.

Turning to our Airbus results, we studied two groups of particles, each group in a cell (see Fig. 3.1) for which the velocity distributions for components v_x and v_y are investigated and are reported in Figs. (3.2)($N = 47$,$\phi = 0.536$) and (3.3)($N = 63$, Area fraction $\phi = 0.7244$). The vibration direction is always the

y axis. The vibration parameters are in Table. 3.1. To show a complete analysis of the data, we focus on the case of the parabola at #10h12, which in Figs. 3.2 to 3.8;). In these Figs, the velocities v_x and v_y are scaled by the characteristic velocities $v_c^x = \sqrt{\bar{v_x^2}} = \sqrt{T_x}$ and $v_c^y = \sqrt{\bar{v_y^2}} = \sqrt{T_y}$ [52], respectively. Logarithmic scale are also shown in the insets of these Figures. In the figures, the solid lines are exponential fitting, i.e. $A * exp(-|B * x|^{1.5})(\nu = 1.5)$, the dot lines are exponential fitting, i.e. $C * exp(-|D * x|)(\nu = 1)$, and the dash lines are Gaussian fitting $E * exp(-(x/F)^2)(\nu = 2)$, where A, B, C, D, E and F are fitting parameters.

As can be seen in Fig. 3.2, the Gaussian fitting underestimates the tails at low and high velocities, and the exponential fitting $\nu = 1.5$ is the best fitting globally, in agreement with previous reports[52, 53, 104]. The characteristic velocity $v_c^y(0.057m/s)$ is found larger than v_c^x $(0.041m/s)$. So anisotropy exists. However, for the denser situation of Fig. 3.3, the characteristic velocity v_c^y $(0.0462m/s)$ is almost equal to v_c^x $(0.0465m/s)$ as given by Fig. 3.3; and the high velocities tail exhibits an exponential fitting with $\nu = 1$ which is the best fitting. These two cases only differ from the number of particle. It is clear that the velocity distribution depends on the number density, as supported by the reference[107].

All up, the foregoing factors influencing the shape of the velocity distribution produce an inconclusive result: one gets two values ($\nu = 1 \sim 1.5$) to fit the exponential tail. These results demonstrate that the velocity distribution of 2D granular gases is not determined uniquely and depends on many factors. But they can be also interpreted due to the system dissipation. If so, let assume that we increase the density, the collision rate will rise, generating more dissipation, and likely more non-Gaussian. Until now, one can not find a detailed expression to describe dissipation of the granular system correctly, taking into account, the multi-body system.

Before finding a global velocity distribution for the vibrating granular media and before applying it to the local Maxwellian assumption, it is useful to know the real local velocity distribution, and its variation with the position in the cell. This might enlighten the true events. Only a few studies can be found using such methodology. Methodologically, the local velocity distribution is more important than the global one. In the next section, we shall examine the local velocity

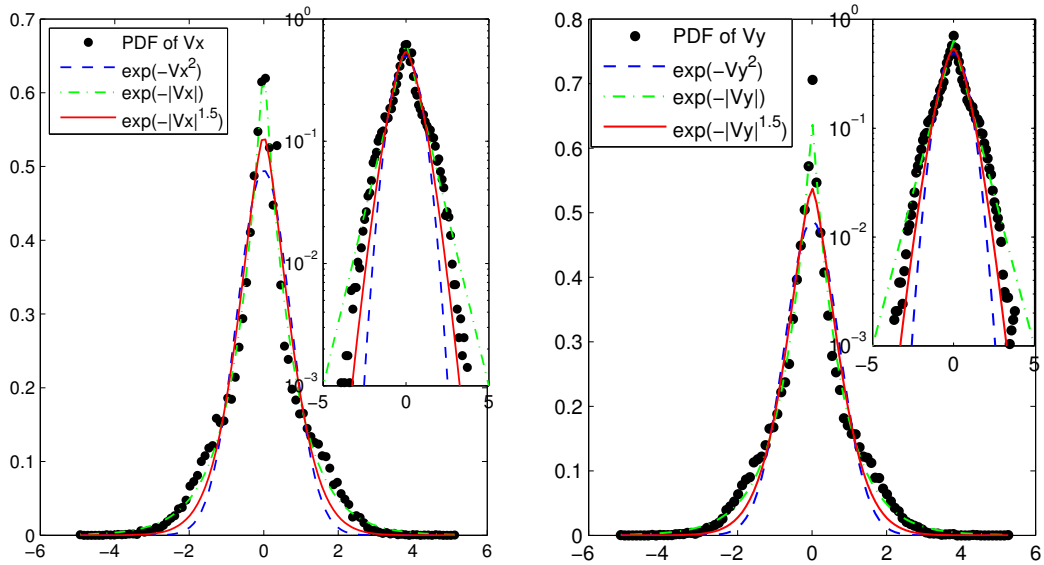

Figure 3.3: The global velocity distributions of the components v_x and v_y. Here, y is the vibration direction. v_x is scaled by v_c^x $(0.041m/s)$. v_y is scaled by $v_c^y = 0.057m/s$. $N = 63$. The area fraction are 0.7244.

distribution.

3.3.2 Local velocity distribution

In this section, the local velocity distributions are investigated to understand better the global behaviour. We shall discuss results coming from the two cells($N = 47$ and $N = 63$) excited with the same vibration parameters. We report only Figs from the parabola at 10h12 (in Table. (3.1)) for clarity and also to save time; but similar trends have been obtained from other parabolas, which are reported in appendix A.

Considering anisotropy of the vibration, we analyze x and y components of velocity distributions, separately. To analyze the system correctly, we decided to divide the cell into 7 bins either parallel to x or to y, to measure the variation of the local distribution along y or along x. This allowed us making average on a same thickness and a long side to get sufficient accurate results, which show up distinct behavior depending on the direction of the bins. When the bins were

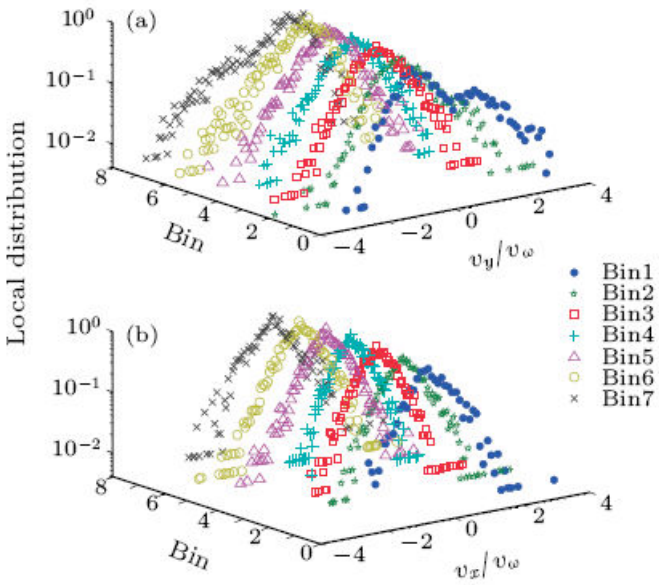

Figure 3.4: Local distribution functions of (a) v_y and (b) v_x on log-linear scales. There are 7 bins along the vibration direction y axis. The vibration parameter(A=0.23mm, V_ω=0.07m/s, Γ=21.56 m/s^2, $f = 49Hz$). $N = 47$.

oriented along (parallel to) y axis, local distribution was rather independent of the bin, while this was not more true in the other direction x.The study using the bins with their length parallel to y did not show up any different trends. So we do not consider such division profile in the following, and we concentrate only with results using bins with length parallel to x, and located at different y (where y is the vibration direction).

After this discussion, we describe what was now done explicitly: The cell is divided into 7 bins along the y axis, and distributions of velocity v_x and v_y are averaged in each bin. Velocities are scaled by the maximum driving velocity $V_\omega(0.07m/s)$. Figs. (3.4) and (3.5) show the local velocity distribution $f(v_x)$ and $f(v_y)$ in each bin, i.e. at different y, for each cells, i.e. Fig. 3.4 for $N = 47$ balls, Fig. 3.5 for $N = 63$ balls. From these results we can conclude the following:

(I) For v_y distributions, $f(v_y)$ at different y. $f(v_y)(y)$ is asymmetric in most bins. Two peaks appear in local velocity distribution profiles of v_y in bins near the two heating boundaries $\widetilde{y} = 0$ or 1 ($\widetilde{y} = y/L$). One shall note this asymmetry in local profiles can be observed. While moving away from the driving wall, asym-

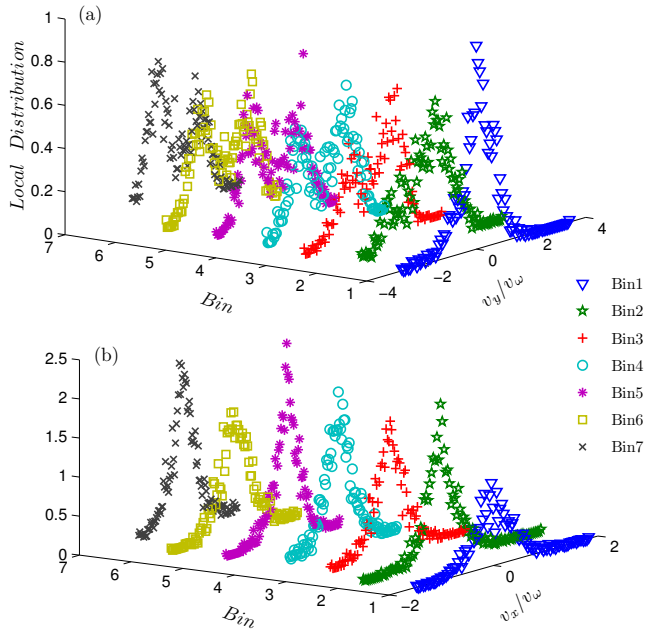

Figure 3.5: Local distribution functions of (a) v_y and (b) v_x on log-linear scales. There are 7 bins along the vibration direction y axis. The vibration parameter(A=0.23mm, V_ω=0.07m/s, Γ=21.56 m/s^2, $f = 49Hz$).$N = 63$.

metry of the profile of the local velocity distribution v_y becomes less profound. In the box center, the profile becomes symmetric, where the boundaries effect may be balanced out.

(II) For v_x distributions, $f(v_x)$ at different y. $f(v_x)$ is symmetric for all the 7 bins. However, the $f(v_x)$ is not-Gaussian.

Turning now to $N = 63$ case of Fig. 3.5, it provides the local velocity distribution of the particle number $N = 63$. We conclude:

(i) v_y distribution , $f(v_y)$, at different y. It seems more complex than Fig. 3.4. one observed in Fig. 3.5. (i), $f(v_y)(y)$ in the boundary bin(7) include this two-peak: one locate in the $v_y > 0$ area and the other locate in the $v_y < 0$ area. So this is different from what is happening in Fig. 3.4. Furthermore, we see also that the amplitude of the two peaks are roughly equal to each other. Moreover, the center bin still includes two peaks as shown in Fig. 3.5 and exemplified in Fig. 3.6. So this distribution persists everywhere and is a new phenomenon. This phenomenon demonstrates that the local state can not be conveniently overlooked as a simple compressible gas anymore and that the local Maxwellian hypothesis is not correct even in the middle of box. Coming back to Fig. 3.1, we observe the packing of the second cell is rather dense and the motions of the different balls are merely coherent, i.e. in phase with the other ones. the whole system looks as a solid. This explain the two peaks structure because the second peak is due to the collision of the other surface that collides half a period after on the other side wall. The direct transmission of that force to the other side show the solid structure of the system during the collision.

(ii) v_x distributions, $f(v_x)$, at different y remains symmetric whatever the bin, as for Fig. 3.4(N=47). To conclude, we think the two peaks effect which is observed in the case of N=63-ball cell demonstrate it is due to a “solid-like” transmission of stress the collision of the system with the vibrating wall at both sides. This means the gas nature of the system is broken at least periodically during these collisions. This is why we will no more consider this case in the rest of the dissertation since it is far from the “gas-like” behaviour.

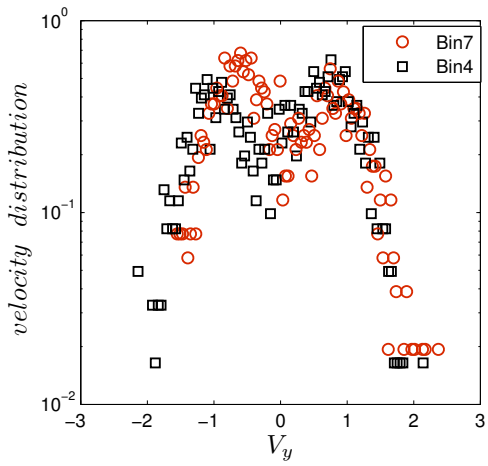

Figure 3.6: The velocity distribution in the boundary layer bin 7 and the center bin 4.

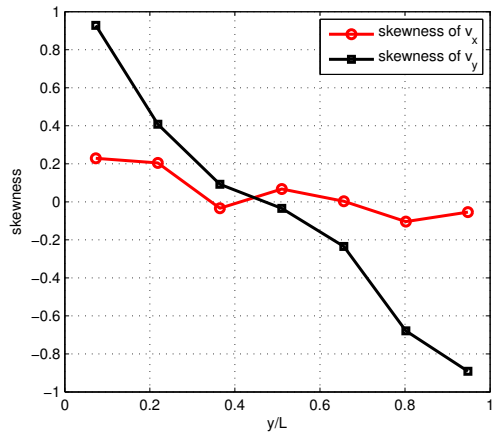

Figure 3.7: The skewness of v_x and v_y distribution profiles along y/L.The vibration parameter(A=0.23mm, V_ω=0.07m/s, Γ=21.56 m/s^2, $f = 49Hz$). $N = 47$.

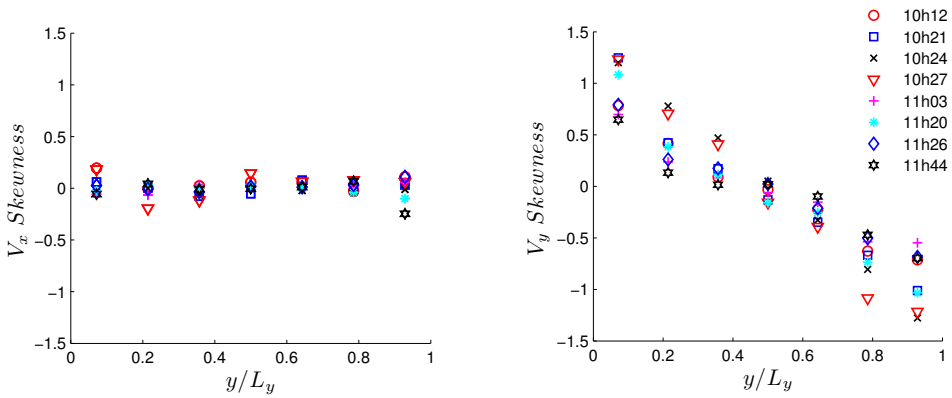

Figure 3.8: The skewness profiles of v_x and v_y along the y axis for various vibrating parameters . All the parameters are listed in the Table (3.1). $N = 47$.

3.3.3 Skewness

For a quantitative analysis of the asymmetry, momentum technique can be adopted to measure quantitative difference between statistics. Skewness S is the third standardized momentum of the sample point. The skewness S of variable q with n sample points is defined as:

$$S = \frac{\frac{1}{n}\sum_{n}^{i=1}(q_i - \bar{q})^3}{(\frac{1}{n}\sum_{n}^{i=1}(q_i - \bar{q})^2)^{3/2}} \tag{3.2}$$

where $\bar{q}$ is the mean of all n sample points q_i. This skewness, applied on velocity distribution, shall be non zero if the velocity distribution is non symmetric. when S becomes large, the asymmetry gets large.

Fig. 3.7 compares the skewness of profiles for v_x and v_y in different bins along y axis for the case of $10h12$ in the Table 3.1. The skewness $S(v_y)$ changes linearly from positive to negative, and is around zero at the center of the box for v_y profiles, while skewness $S(v_x)$ seems flat and equals to 0 for local v_x distribution in these seven bins. Furthermore, over a wide range of Frequency and Amplitude (in Table (3.1)), the skewness of the local velocity distribution yield the same rule as shown in Fig. 3.8. All the results are consistent with our previous results[13].

3.4 the phenomenological model

In this section, we focus only on the case for N=47 balls for which we shall give some theoretical description to explain the above phenomena on v_y distribution. We first recall some previous works, then we present our phenomenological model.

3.5 The phenomenological model and GSH

We come to the description of the two peaks observed in the local velocity distribution function and we give a phenomenological model[115]. To account for a two-peak fluid, it seems obvious that one should employ as variable two different sets of T, ρ, ρv, for the $(+)$ and $(-)$ particles, along with formulas for the pressures, P_+ and P_-[116]. In addition, one would need two additional sets of T, ρ, ρv for $\hat{y}$ and $\hat{z}$. We are afraid this opens a Pandora box of state variables, neither conserved nor truly independent, rendering the theory quite arbitrary and unable to widen efficiently. One should instead, we believe, retain the conserved variables ρ and ρv, also T as the average width of all peaks in the system[116]. It should sufficient, for a minimal, surgical modification, to introduce two additional variables.

To describe these two peaks velocity distributions, we first think how many variables to consider. For a normal Gaussian distribution(since the mean of the speed distribution is zero, here due to steady state), one parameter is enough to describe, the width of the distribution(for Maxwell distribution, the width is T), can describe all the information of the distribution. Our experiment results show that one peak of two-peak distribution is located in positive and the other in the negative area.

So two parameters should be considered. The first is the distance between the two peaks, which is the crucial second scale of a two peaks distribution, much more relevant than the difference between the two widths. To present the velocity difference between two distribution, we add a new variable Δ_i, which is used to assist original variable T_x. Δ_i should be described the positive and negative velocity difference. As being a velocity difference, the new variable Δ_i is odd under time reversal and a vector.

As above experiment results discussed, this difference only exists in vibration direction, on our case, only $\Delta_x \neq 0$. Second is ,the anisotropy, difference between T_x and T_y, between the average width along $\hat{y}$. More generally, we have $\delta T_i \equiv T_i - T$, $i = x, y, z$, with $\sum_i \delta T_i = 0$. These are similar to the order parameter of nematic liquid crystal[117]. The diagonal elements of a symmetric, traceless tensor. (They do not form a vector, because T_x does not distinguish between $\hat{x}$ and $-\hat{x}$.) So a tensor, even under time reversal, needs to be added. Instead of δT_{ij}, however, we employ t_{ij}, the deviation of the granular temperature T_g as considered below, see Eqs(1.5). In our case, only $t_{xx} = -t_{yy} \neq 0$.

Granular solid hydrodynamics(GSH)[98, 118] was derived employing the hydrodynamic procedure. GSH is based on general principles which are independent of the system density. GSH obtains equations that include collisions and enduring contact, which are valid in the dense, elastic-plastic limit, and the rarefied one. For instance, GSH is capable of accounting for the relaxation of the temperature until it is zero.

Although the present system deviated from rarefied gas in the opposite direction, towards ballistical, the hydrodynamic procedure still works, if we add variables that characterize the deviation from local equilibrium. The reason is the hierarchy of equilibria: Although the two peaks three widths are not in equilibrium with one another, the elements within each are well thermalized.

In deriving GSH, a granular heat w is introduced with s_g the granular entropy, and $T_g \equiv \partial w/\partial s_g$ the associated temperature. It quantifies the energy contained in the mesoscopic, intergranular degrees of freedom, especially the strongly fluctuating part of the grains' kinetic and elastic energy. Expanding w in s_g, we have

$$w = s_g^2/(2b\rho) = b\rho T_g^2/2, \quad b \sim (\rho_{cp} - \rho)^{a_1} \tag{3.3}$$

with $a_1 = const$. The lowest order term is quadratic because equilibrium, or minimal energy $w = 0$, is given for $s_g = b\rho T_g = 0$. (This is quite the same idea as with any Ginzburg-Laudau energy functional, just without the fourth order term, or a phase transition.) The density dependence of $b(\rho)$, with ρ_{cp} the random close density, is chosen such that the associate pressure[98, 119],

$P \equiv (\rho\frac{\partial}{\partial\rho})(w - T_g s_g) = -\frac{1}{2}\rho^2 T_g^2 \partial b/\partial\rho$, given as

$$P = \frac{a_1 \rho w}{\rho_{cp} - \rho} = \frac{\frac{1}{2}a_1\rho^2 T_g^2}{\rho_{cp} - \rho} \tag{3.4}$$

is appropriate for all densities[120].

For a rarefied system, in which the elastic contribution to the energy is negligible, we may identify the energy $w = \frac{1}{2}b\rho T_g^2$ with the kinetic energy per unit volume ρT (for a 2D system), implying $bT_g^2 \sim 2T$, especially in the above expression for the pressure. Clearly, taking $T_g \sim \sqrt{T}$, Haff's granular hydrodynamics is retrieved.

If the temperature is maintained by vibrating walls, we need(as discussed above) Δ_i and t_{ij} as additional variables. They also contribute to the energy which, in an expansion in all three variables, becomes

$$w = (b\rho T_g^2 + c\rho\Delta_i^2 + e\rho t_{ij}^2)/2 \tag{3.5}$$

These variables relax, specifically because they possess energy that may be redistributed among microscopic, inner-granular degrees of freedom(such as photons). The energy being quadratic, the relaxation stops when the variables are zero, and the energy vanishes.

Taking $c, e = const$, independent of the density, the pressure is not changed by introducing the new variables, and remains as given in Eq. 3.4, (Same with $P \sim \partial/\partial\rho$), additional pressure contributions would have resulted from $\partial c/\partial\rho$ and $\partial e/\partial\rho$) We assume this for simplicity, as we are more interested in an anisotropic stress, less in modifying a given pressure.

Next we relate Δ_x, t_{xx} to parameters of $f(v_x)$ and $f(v_y)$, the velocity distributions, as the latter is indenpently measurable. Denoting the norm as $N \equiv \sqrt{\pi T_x}(1+\alpha)$ and $2k_B = 1$, we take

$$f(v_x) = \frac{1}{N}(\alpha exp\frac{(v_x - \xi)^2}{-T_x} + exp\frac{(v_x + \alpha\xi)^2}{-T_x}) \tag{3.6}$$

and $f(v_y) = f(v_x \to v_y,\ T_x \to T_y,\ \xi = 0$, with $\langle v_x\rangle$, $\langle v_y\rangle = 0$, see Fig 1. The energies along $\hat{x}$, $\hat{y}$ are then $w_x = \frac{1}{2}\rho T_x + \rho\alpha\xi^2$ and $w_y = \frac{1}{2}\rho T_y$, implying, first of

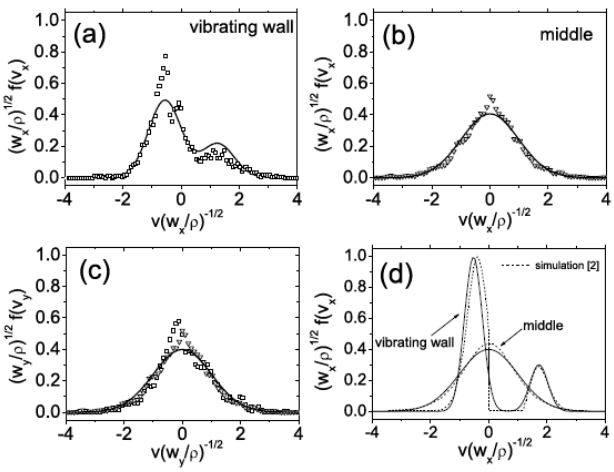

Figure 3.9: Velocity distribution as simulated in [12], measured in [13], and parameterized by Eq (3.6). Fig (a) and (b) show $f(v_x)$, for the velocity perpendicular to the vibrating walss, with (a) showing f close to the wall, and (b) showing f in the middle. Fig(c) shows $f(v_y)$, while Fig (d) again shows $f(v_x)$. Symbols are measurements, dotted lines simulation, and full curves are Eq(3.6). For the two peaks distributions, we have $T_x = 10$ and 1, $\xi = 2.2$ and -1, 37, and $\alpha = 2.3$ and 3, for Fig (a) and (d), respectively.

all, $\alpha \to c$, $\xi \to \triangle_x$.

Taking $T_x = \frac{1}{2}(T + \delta T_{xx})$, $T_y = \frac{1}{2}(T + \delta T_{yy})$, with $\delta T_{xx} + \delta T_{yy} = 0$, we find that the energy, $w_x + w_y = \frac{1}{2}\rho T$, does not depend on δT_{xx}. But taking

$$T_x = b(T_g + t_{xx})^2/4, T_y = b(T_g - t_{xx})^2/4 \tag{3.7}$$

we obtain $w_x + w_y = \frac{1}{2}\rho b(T_g^2 + t_{xx}^2)$, as in Eq(3.5). This discrepancy may be surprising at first, but results from ρT being the energy of an ideal gas, or the kinetic energy of a rarefied gas, with no collision contributions. Yet collisions are what equalize T_x and T_y. On the other hand, $w = \frac{1}{2}\rho b T_g^2$ is the total energy of an interacting system. Increasing T_g by t_{xx} in one population, and decreasing it by t_{xx} in another, must lead to an energy increase, as t_{xx} would nor relax otherwise. Still, we should not take the equality of b and e seriously, as it hinges on the previous assumption that w_x, w_y remain sensible quantities in an interacting system. In contrast, expanding w in t_{ij} leading to Eq(3.5) is generally valid

approach.

Having specified the additional variables and their contributions to the energy, we may employ the same hydrodynamic procedure as used for GSH[98, 118], to set up their equations of motion. The generalized hydrodynamics consists of continuity equations for momentum, $\partial_t(\rho v_i) + \bigtriangledown_j(\delta_{ij} + \rho v_i v_j) = 0$, and mass, $\partial_t \rho + \bigtriangledown_i(\rho v_i) = 0$, in addition to the balance equations,

$$T_g[\partial_t s_g + \bigtriangledown_i(s_g v_i - \kappa_g \bigtriangledown_i T_g)] = \eta_g v^*_{ij} v^*_{ij} - \gamma_g T_g^2 \tag{3.8}$$

$$\partial_t \triangle_i + \bigtriangledown_j (\triangle_i v_j - \kappa_\triangle \bigtriangledown_j \triangle_j) = \alpha \triangle_j v^*_{ij} - \gamma_\triangle \triangle_i \tag{3.9}$$

$$\partial_t t_{ij} + \bigtriangledown_\kappa(t_{ij} v_\kappa - \kappa_t \bigtriangledown_\kappa t_{ij} = \beta v^*_{ij} - \gamma_t t_{ij}) \tag{3.10}$$

with

$$\sigma_{ij} = P\delta_{ij} - \eta v^*_{ij} - c\rho\alpha \triangle_i \triangle_j - e\rho\beta t_{ij} \tag{3.11}$$

The first equation is the same as in GSH. It reports a convective, a diffusive ($\sim \kappa_g$) and a relaxative term($\sim \gamma_g$, in addition to viscous heating, with η_g the viscosity, and v^*_{ij} the shear rate $-v^*_{ij}$ being the traceless part of $v_{ij} \equiv \frac{1}{2}(\bigtriangledown_i v_j + \bigtriangledown_j v_i)$. Employing $T_g \sim \sqrt{T}$, one sees that Eq (3.8) is the same as Haff's energy balance[121]. Eqs(3.9,3.10) are new, but quite similar to (3.8). They also each report a convective, diffusive, and relaxative term. Instead of viscous heating, however, there is a linear, offdiagonal Onsager term: with v^*_{ij} as the thermodynamic force, $\triangle_i$ as the preferred direction, and α an Onsager coefficient in Eq(3.9).

The stress σ_{ij} consists of pressure, viscous stress (with bulk viscosity neglected), and the two counter Onsager terms. The signs of α, β in the three equations obey Onsager reciprocity relation; and because both $\triangle_i \bigtriangledown_j v^*_{ij}$ and $v^*_{ij} t_{ij}$ are odd under time inversion, their respective contribution to the production of true entropy (not displayed) vanishes. There is no constraint on the sign or magnitude of α, β; both are functions of the density.

To solve Eq(3.8, 3.9, 3.10, 3.11), we first note that for the above discussed Herbst geometry, setting $v_i, v_{ij} = 0$, and assuming dependence only $\hat{x}$, we have

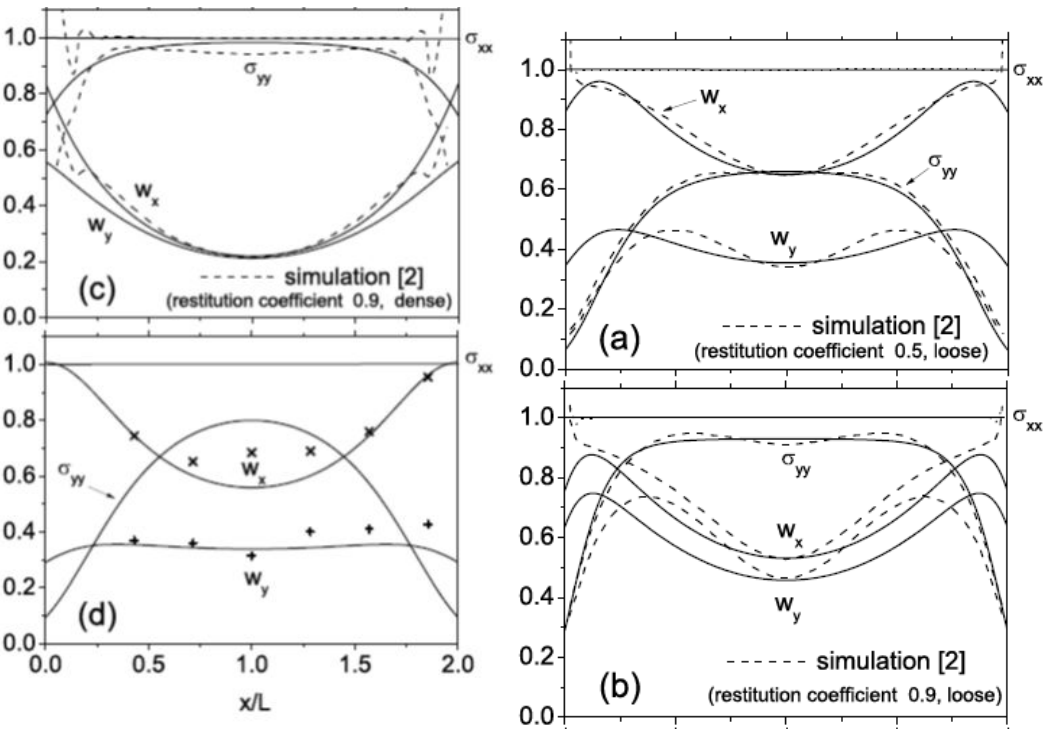

Figure 3.10: variation of stress and kinetic energy along $\hat{x}$. We employ $\sigma_{xx} = const$ as the unit of stress and energy density. Full curves are hydrodynamic results, taking $w_x = \rho b T_g^2/4 + \rho e t_{xx}^2 + \rho c \triangle_x^2 /2$, and $w_y = \rho b T_g^2/4 + \rho e t_{yy}^2$, with $b_0, c, e = 1$, and $l_g = 1, 1.1, 1.2, 1$, $l_t = 0.8, 0.9, 1, 0.5$, $l_\triangle = 0.18, 0.28, 0.55, 0.3$, $a_1 = 1.38, 1.2, 0.33, 0.9$, $\rho_{cp} = 0.7, 0.7, 0.7, 0.8745$, $-\alpha = 13, 1.49, 0.772, 0.5$, $-\beta = 3.68, 2.14, 2.18, 3.5$ for (a), (b), (c), (d), respectively. Symbols are from micro-gravity measurements[13], and dotted lines from simulations of [12].

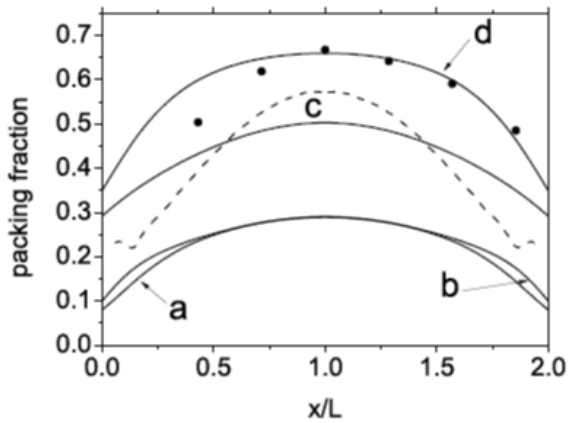

Figure 3.11: Variation of the packing fraction for the four cases in Fig. 3.10. Symbols are from micro-gravity measurements of [13] and dotted lines from simulations of [12].

$\sigma_{xy} = 0$,

$$\sigma_{xx} = P - c\rho\alpha \triangle_x^2 - e\rho\beta t_{xx}.\sigma_{yy} = P(x) + e\rho\beta t_{xx} \tag{3.12}$$

Force balance $\nabla_j \sigma_{ij} = 0$ requires $\sigma_{xx} = const$, but leaves σ_{yy} undetermined. Denoting $l_g^2 \equiv \frac{\kappa_g}{2\gamma_g}$, $l_\triangle^2 \equiv \frac{\kappa_\triangle}{2\gamma_\triangle}$, $l_t^2 \equiv \frac{k_t}{2\gamma_t}$, with $2L$ the distance between the two vibrating walls, and employing the boundary conditions: $T_g = T_0$, $\triangle_x = \triangle_0$, $t_{xx} = t_0$ at $x = 0$, and $T_g = T_0$, $\triangle_x = -\triangle_0$ at $x = 2L$, the stationary solution, for $\partial_t s_g$, $\partial_t \triangle_i$, $\partial_t t_{ij} = 0$, is

$$\frac{T_g}{T_0} = \frac{cosh\frac{x-L}{l_g}}{cosh\frac{-L}{l_g}}, \frac{t_{xx}}{t_0} = \frac{cosh\frac{x-L}{l_t}}{cosh\frac{-L}{l_t}}, \frac{\triangle_x}{\triangle_0} = \frac{sinh\frac{x-L}{l_\triangle}}{sinh\frac{-L}{l_\triangle}}, \tag{3.13}$$

Note we have taken all transport coefficients, generally functions of ρ, T_g, $\triangle_i$, as constant. (Although κ_g, $\gamma_g \sim T_g$), see [98, 121], this does not change the solution if included, since the equation contains only the ratio $l_g^2 \equiv \frac{\kappa_g}{2\gamma_g}$. Searching for an understanding at present, we are unabashedly qualitative. Given the scarcity of experimental and simulation data, there is too much arbitrariness for more quantitative considerations. For a comparison of theory, experiment, and simulation, see Fig. 3.10 and 3.11.

3.6 Hydrodynamic description

3.6.1 the hydrodynamic model

In the steady state, the conservation of momentum requires[122]:

$$\int_0^{+\infty} vf(v)dv = -\int_{-\infty}^0 vf(v)dv. \tag{3.14}$$

In turn, near the boundary $y = 0$, the number of particles moving towards the wall and leaving the wall shall be conserved, that is, the number of particles leaving the vibrating wall shall be equal to the number of particles moving towards the vibrating wall in a sawtooth excitation:

$$f_y^-(v_y)v_y = f_y^+(2V_\omega - v_y)(v_y - 2V_\omega) \tag{3.15}$$

Here, f_y^+ (f_y^-) is the velocity distribution function for the $v_y > 0$ ($v_y < 0$). The number density n near the boundary $y = 0$ can therefore be obtained from particle-number conservation mentioned above[122]:

$$n_y = 2n_y^- + 2V_\omega \int dv_y \frac{f_y^-}{v_y - 2V_\omega} \tag{3.16}$$

It implies at the boundary $y = 0$, n_y^+ is smaller than n_y^-. The discrepancies between n^+ and n^- are confirmed in our experimental results shown below (Fig. 3.12).

To measure the hydrodynamic field, the box is subdivided into strips along the vibrating direction.

3.6.2 The number density

The four components of the number density $n_x^+(y)$, $n_x^-(y)$, $n_y^+(y)$, $n_y^-(y)$ are shown in Fig. **??** (a) and (b). Here, the notation used is: $n_x^+(y)$ means the spatial profile of the number density of particles with velocity $v_x > 0$ along the y direction. It is observed that $n_x^+(y)$ and $n_x^-(y)$ overlap and their peaks occur at the cell center as in Fig. **??**(a). The curves in Fig. 3.12 (b) confirm the difference

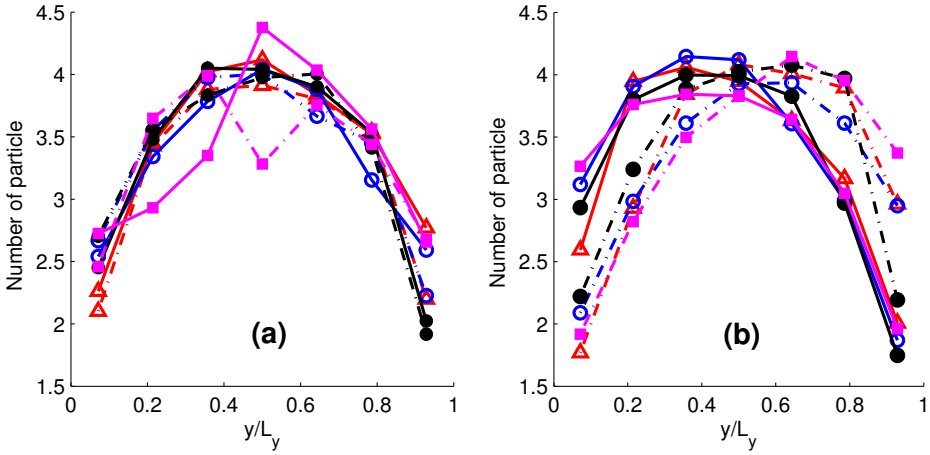

Figure 3.12: (a) The number of particles in each bin with velocity $v_x^{\pm}$. (b) The number of particles in each bin with velocity $v_y^{\pm}$. (△) V_ω=0.07m/s. (○) V_ω=0.067m/s. (●) V_ω=0.087m/s. (■) V_ω=0.038m/s. Solid curves are for the positive components, and the dashed curves for the negative ones.

of behaviour between $n_y^+(y)$ and $n_y^-(y)$ near the boundaries, predicted in Eq. (3.16). Moreover, n_y^+ and n_y^- do not overlap. The components $n_y^+(y)$ and $n_y^-(y)$ are mirror symmetric to each other as shown in Fig. 3.12(b). It is apparent that $n_y^+(y) \neq n_y^-(y)$. This has often been ignored in previous works when calculating the transport parameters in granular system[66, 70].

3.6.3 The Temperature

Here, as Fig. 3.13 exhibits it, one shall define two different temperatures T_x and T_y, one for each x or y direction, in the case of Airbus experiment with the cell containing 47 balls. It can be seen that the difference between two temperature components T_x and T_y. The anisotropy is quite real and $T_y > T_x$. This is because the heating mechanism (vibration) is in the $\hat{y}$ direction only, generating the anisotropy in our case. In [123], smooth granular material is fluidized by vertically shaking of a container in gravity. The authors also find that the temperature in the direction of the energy input always exceeds the temperature in the other direction. Our results agree well with theirs ($T_y > T_x$, $\hat{y}$ is the energy input direction).

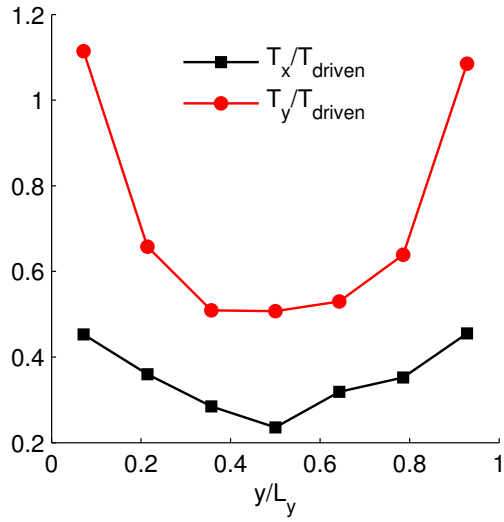

Figure 3.13: The T_x and T_y variation in the y direction, scaled by T_{driven}, where $T_{driven} = mv_{driven}^2$. There are 7 bins along the vibration direction y axis. The vibration parameter(A=0.23mm, V_ω=0.07m/s, Γ=21.56 m/s^2, $f = 49Hz$). $N = 47$.

Another question is the shape of the temperature profile, which is normal constant in Fig. 3.13. However, some explanation exists; for instance, in[122], a hydrodynamic model is adopted to explain the shape of the temperature profiles.

We want to discuss now why and how the velocity distribution is asymmetric, and why and how it influences the temperature profiles. It is of interest to examine the positive and negative components of the temperatures T_x and T_y. In other words, T_x is divided into two components, T_x^+ and T_x^- according to the sign of the velocity v_x. Fig. 3.14 exhibits a typical variation of T_x^+, T_x^-, T_y^+ and T_y^- profiles in our micro-gravity experiment. It can be seen that $T_x^+ \approx T_x^-$, and $T_y^+ \neq T_y^-$. T_y^+ and T_y^- are symmetric from each other through the central axis of the cell. The value of T_y^+ gets its maximum in the boundary($y = 0$), while the maximum of T_y^- located in the boundary ($y = L$).

We note that $T_y^+ \neq T_y^-$ is a very surprising result. $T_y^+ \neq T_y^-$ means the energy equipartition is broken into the energy input direction even in pure granular-gas system. In fact, the non-equipartition of the energy was first found in the binary mixture in the experiment[124] and simulation[125]. Here, this result shows that

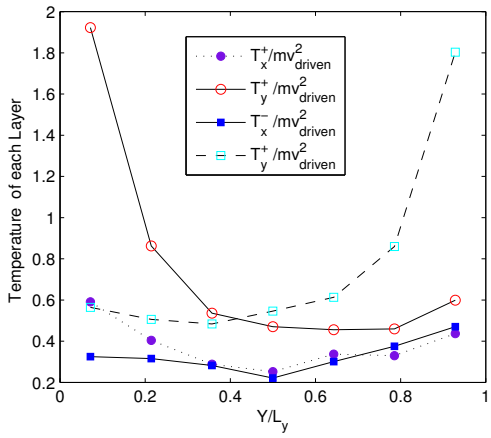

Figure 3.14: The four temperaturescompeting to describe the samples. There are 7 bins along the vibration direction y axis. The vibration parameters(A=0.23mm, V_ω=0.07m/s, Γ=21.56 m/s^2, $f = 49Hz$). $N = 47$.

the profiles of T_y can not reflect the total information of the granular velocity fluctuation. This proves that the granular temperature definition needs to be modified.

3.7 The mean free path

Mean free path is a basic concept in the kinetic theory. It is defined as the average distance that the particle travels between two successive collisions. A zig-zag path of a molecule is illustrated in Fig. 3.17. (a)[126]. This path is straightened out as shown in Fig. 3.17 (b). The number of molecules in the straight cylindrical volume surrounding the straight line trajectory, which is the effective volume explored by the molecule per unit of time, can be written:

$$\Theta = \pi d^2 \bar{C} n \tag{3.17}$$

where $\bar{C}$ is the uniform speed, n denotes the number of molecules per unit volume of gas, d is the diameter of molecules. Here, the straight cylindrical volume is $\pi d^2 \bar{C}$. Θ represents the number of particles in such cylindrical volume and also denotes the number of collisions per unit time for one molecule z (Fig. 3.17).

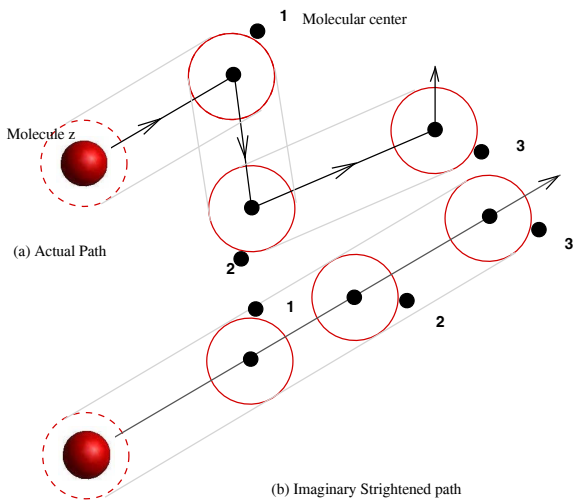

Figure 3.15: Path of Molecule z among stationary path

The mean free path for three dimension turns out to be

$$\lambda = \frac{1}{\sqrt{2}\pi d^2 n} \tag{3.18}$$

The factor $\sqrt{2}$ is the ratio between the mean relative speed and the uniform speed.

More importantly, the mean free path is often used to be a parameter to judge the suitable scope of the kinetic theories and hydrodynamics for granular medium[66]. The concept of mean free path is based on the assumption of particles being in random distribution, i.e., Maxwell-Boltzmann distribution is valid. However, in our system, the velocity distribution is no longer the Maxwell-Boltzmann distribution. Moreover, the local velocity distribution is asymmetric and anisotropic. This indicates the breakdown of kinetic models based on the concept of the mean free path.

Let us consider the mean free path in the granular system. According to the equation ($l = \frac{1}{\sqrt{8}nd}$) for two dimensional situation, the mean free path of our Airbus data is $6E-4$ for $N = 47$ and $4.6E-4$ for $N = 63$. Due to the local velocity distribution asymmetry, it is not possible to make a simple average, but we have to consider the collisions between the different kinds of particles. At the cell wall, for instance, while the asymmetry of velocity v_y is the largest, one has

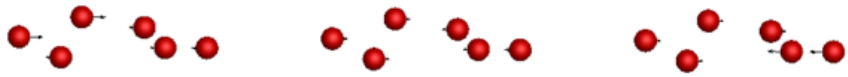

Figure 3.16: Sketch of the breakdown of the mean free path. On the right and left sides of the cell, the v_y distribution is asymmetric, contrary to what occurs in the cell center. As there is no net flow, it means the density number n^+ and n^- are different. So this imposes to define two mean free paths through $n^- dl_c^+ = n^+ dl_c^- = 1$.

to define two mean free paths, l_c^+ and l_c^-, for the two "kinds" of particles with v^+ and v^-. In Fig. 3.4, on the right and left side of the cell, the v_y distribution is asymmetric, contrary to what occurs in the cell center. As the average flow is zero, it means the density number n^+ and n^- are different. So this imposes the need to define two mean free paths that $n^- dl_c^+ = n^+ dl_c^- = 1$ (d is the particle diameter).

In our experiments, all the particles can be tracked. Because of the microgravity, the particle trajectory(a line) changes directions if and only if it is happened a collision. So if a trajectory direction changes more than 20 degree, we suppose that a collision happens. The spatial profile of the local collision times is illustrated in Fig. 3.17. The collision time are largest in the box center due to the highest density in the box center. Since we know the local collision frequencies (N^+/N^-) and the mean velocities ($\bar{c}^+/\ \bar{c}^-$), then, two mean free path are given by the expression:

$$l^+ = \frac{\bar{c}^+}{N_c^+} \tag{3.19}$$

Fig. 3.18 show the spatial profiles of l^+ and l^- calculated by Eq. 3.19. l^+ and l^- are different with each other as expected except for the center point. l^+ and l^- is smaller than the $6E-4$ but still have the same magnitude. It is difficult to obtain the mean free path precisely from the tracking. In the next Chapter about the simulation, the local mean free path will be discussed in detail.

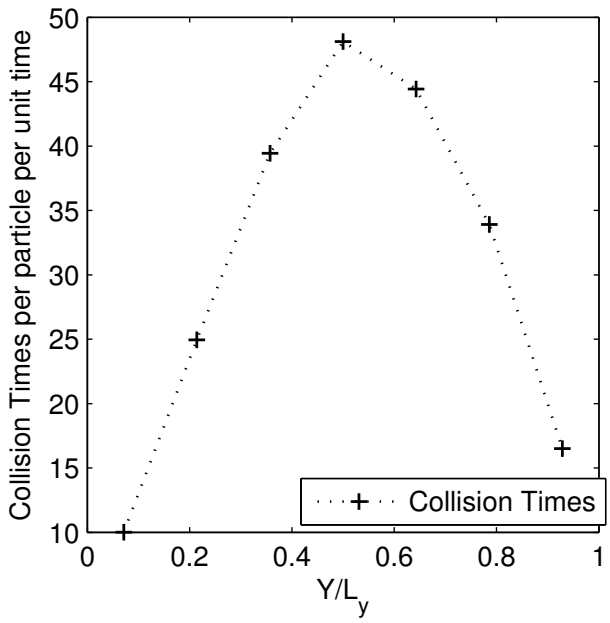

Figure 3.17: The spacial profiles of the collision times($L_x = L_y = 300$, $N = 47$, the vibration parameters A=0.23mm, V_ω=0.07m/s, Γ=21.56 m/s^2, $f = 49Hz$).

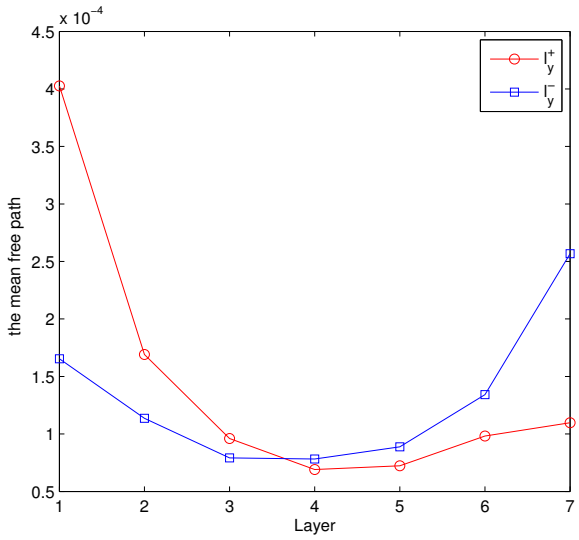

Figure 3.18: The spatial profiles of mean free path l_y^+ and l_y^-, which are calculated by Eq. 3.19($L_x = L_y = 300$, $N = 47$, the vibration parameters$A$=0.23mm, V_ω=0.07m/s, Γ=21.56 m/s^2, $f = 49Hz$).

3.8 Summary

In this chapter, the aim has been to investigate a vibrated granular gas confined by a rectangle box in micro-gravity. The study focuses on the steady state with the zero velocity field. The major results could be summarized as follows: (i) The global velocity distribution is isotropic. The mean value of the velocity component in vibration direction v_y is larger than non-vibration component v_x; (ii) The spatial profiles of the local velocity distributions $f(v_y)$ is asymmetric, while $f(v_x)$ is still symmetric everywhere. Moreover, $f(v_y)$ in the boundary layer even appears two peaks, then two peaks melts into one peak gradually when moving from the boundary to the box center. Double-Gaussian distribution model is used to describe the local velocity distribution $f(v_y)$; (iii) Granular hydrodynamic solid theory is adopted to explain the stress profiles, and agrees well with our experiment results and others' simulation results; (iv) The two temperature components T^+ and T^- are not equal to each other as expected. It proves that the energy equipartition breaks in a vibrated granular gas; (vi) The local mean free path of l^+ and l^- are different with each other, too.

All prove that the vibrated granular gas is different with the classical molecular gas. The steady state of granular gases is just a dynamic process. Even with zero the velocity field, the granular gases still show plenty of surprising phenomena, for example, energy equipartition breaks down. From a more practical point of view, double-Gaussian distribution model is simple but is closer to the reality of a vibrated granular gas, which is strongly affected by two vibrated wall. Maybe one argues that our box is not large enough to avoid the boundary effect. We will lengthen the box size and prove that the boundary effect is a long range effect for a vibrated granular gas by simulation in the next chapter.

Chapter 4

Event-Driven Molecular Dynamics simulation Results

4.1 Introduction

As mention in Chapter 3, we have found that dilute granular media, or granular gases, behave very differently from molecular gases[12, 52, 56, 66, 88, 127]. Due to inelastic collisions, energy injection is needed to maintain a steady state. In most experimental case, energy is injected through boundary shaking. This kind of boundary heating mechanism introduces anisotropy to the granular gas system. In our previous microgravity experiment[13], the distribution profiles of the two velocity components, v_y (vibrating direction) and v_x (perpendicular direction), are found different. While the local distribution of v_x is symmetric, the local distribution of v_y is found asymmetric. This asymmetry is generated by the boundary heating , (at least it is consistent with the boundary excitation and with dissipation), but it has a long range effect, which modifies the distribution in the whole cell (see chapter 3).

A similar effect can be also found in a bi-disperse granular system. For two species of particles, energy equipartition doesn't persist[124] and segregation appears, modifying the energy input. Hence, this energy equipartition is found to be affected by the "heating" mechanism(we write here "heating" in between quotation marks, because boundaries deliver a "constant" speed to each ball rather

than a real constant "heat". This is why we need to speak of "velostat" [128]) .

Different kinds of particles are unequally heated at the boundaries, and this heating effect at the boundary is found to influence the level of non-equipartition even in the bulk of the system. The boundary effect can never be forgotten even in the limit where heating events are rare compared to collisions[125].

Such long range effects do not exist in elastic system even with the boundary heating , or at least this is what we are thinking. Hence, the long range boundary effect results from a combination of inelasticity of the dissipation in granular media and of the boundary condition, which is not used as a heater but better as a mechanical excitator, since it is no more a thermal energy which is given in our case, but a transfer of momentum. To study this long range boundary heating effect may help understanding the real dissipative macroscopic laws of the granular system. Most of previous works [12, 122, 129–131] assume this effect only exists in the boundary layer and try to avoid it. For example, some papers only study the velocity distribution of particles in the central area of the box. Taking no account of the boundary effect, it is clearly misleading the boundary " heating " process of the granular system (as already told the boundary plays the part of generator of impulse so that the boundary is not a thermostat, but shall be better called "velostat" , or "speed injector" in one direction)..

In this chapter we investigate the role of the coefficient of restitution of particles in determining the extent of the "heating" in the whole medium. So, we use event-driven molecular dynamic (MD) simulation to study the macroscopic and microscopic transfer laws in the system.

As it will be demonstrated in the section 4.2, the simulations we performed show and confirm that there exist anisotropic temperature T_x and T_y (T_x diff T_y) in the two different direction; but also that the behaviour is more intricate and that we can find two different temperatures T_y^+ and T_y^- depending on the way the particle fly (towards $+y$ or toward $-y$). It shows different temperature components depending on the way in the y (i.e. excitation) direction $T_y^+(y)$ (temperature of particles moving in positive y direction) differs from $T_y^-(y)$ (temperature of particles moving in the opposite direction). So the energy equipartition is broken down in many ways. This agrees with the previous experimental observation of the Chapter 3[13] and simulation results[129]. We also find that the ratio of

these two components of temperature $T_y^+(y)$ and $T_y^-(y)$ drops exponentially along the y direction Fig. **??**. All results confirm that the long range boundary effect depends on the dissipation properties of the granular gas.

In this Chapter 4, our goals are studying the local steady state at a local scale using 2D driven granular gas excited by boundary. In other words, the analyses is based on the assumption that one needs to separate positive and negative speed, because the positive and negative parts of the velocity component in the vibration direction are different, their energy coming from different boundary, and their dissipation "from the other side".

The event-driven molecular dynamic simulation is adopted. Section 4.2 illustrates the model rules of our simulation. In section 4.3, data are presented, which exemplify the system local velocity distribution and the skewness is defined, which quantifies the asymmetry of the distributions. We give their dependence at various number of the particles and the restitution coefficient. By considering the local velocity distribution asymmetry, we also show the difference between the positive and negative mean-free-path and their difference from the classical expression. Similarity, the dissipation of the granular matter is presented from the four parts of the gas, which are defined by the four different direction of velocities the sign of the velocity components(v_x^+, v_x^-, v_y^+, and v_y^+). Section 4.4 shall list and display the "hydrodynamic" parameter p_x^+, p_x^-,p_y^+, p_y^-, T_x^+, T_x^+, T_y^+ , T_y^+ in accordance with the sign of velocity components. Results will provide their distribution in the gas as functions of excitation parameters and dissipation (restitution coefficient or number of particles.)

4.2 The model

We consider a 2D driven granular gas of N inelastic hard spheres with diameter $d = 2$ and mass $m = 1$ in a square box ($L = 300$) (shown in Fig. 4.1). An event-driven molecular dynamic algorithm is adopted[17]. No friction and rotation are considered in the model. The vibrating boundary varies as a triangular vibration in the y-axis direction; its peak-peak motion is $D = 5r$, and velocity $v_\omega = \pm 5r$, where $r = 1$ is the particle radius; this implies $2\pi\omega = 1$ in the system of units

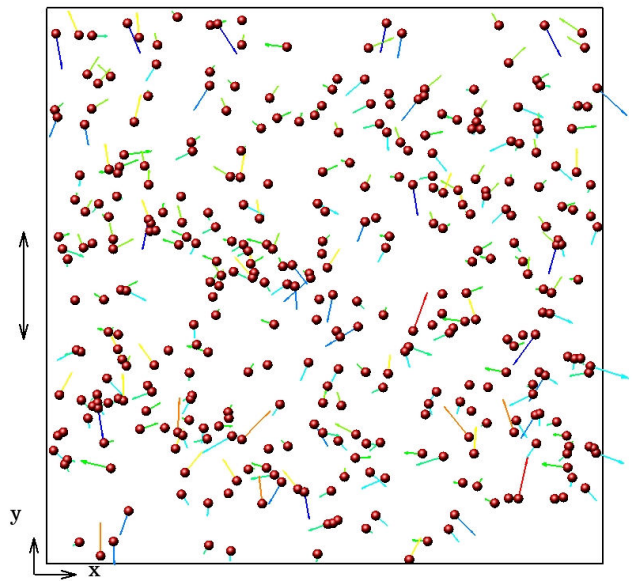

Figure 4.1: The snapshot of a granular gas $N = 360$.

used. The particle velocities of post-collision with wall are given by:

$$v'_x = -e_w * v_x$$

$$v'_y = -e_w * v_y + (1 + e_w) * v_{driven}$$

Where e_w is the coefficient of restitution between the particle and the wall. The post-collision velocities of colliding spheres i and j are determined by:

$$\vec{v'_i} = \vec{v_i} - (1 + e_p)[(\vec{v_i} - \vec{v_i}) \cdot \vec{n}]\vec{n}$$

$$\vec{v'_j} = \vec{v_j} + (1 + e_p)[(\vec{v_j} - \vec{v_j}) \cdot \vec{n}]\vec{n}$$

Where e_p represents the coefficient of restitution between the particles, $\vec{n}$ is the unit vector between the two particles mass centers. e_p and e_w range between [0, 1]. Gaussian random number is given for initial velocities and positions of particles. Here, we focus on the " steady" state of the granular system. So, all the particle velocities and positions are recorded after the system go through ten thousand collisions and reach a steady state.

We want to study a steady state, this implies that the means of local quanti-

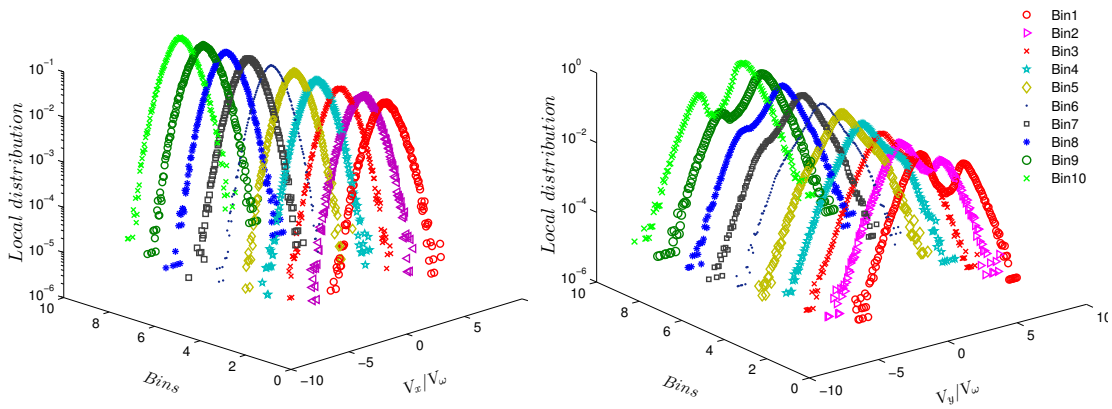

Figure 4.2: Spatial profiles of v_x (left) and v_y (right) (semi-logarithmic) are plotted along the y direction. The particle radius r is set to be 1. The size of the cell is $(300r \times 300r\ )$. The number N of particles is $N = 360$, the area fraction is $\phi = 0.0126$, and the restitution coefficient $e_p = 0.75$.

ties averaged over short times remains constant with time (within some average fluctuations). Local equilibrium means the system is spatially and temporally divided into "cells" or "Micro-phases" in small size, in which the classical quantities remain steady with a good approximation. In this section, we study the local equilibrium by dividing the cell into several bins along the vibrating direction y-axis and similarly into the x-axis, to evaluate anisotropic effect..... Each bin is treated as a local unit and we will examine the local equilibrium state in each bin. In this work the cell is divided into 60 bins.

4.3 Velocity distribution and its skewness

In this section, we investigate the dependencies of the local velocity distribution as functions of various coefficient of restitution and of the number of particle. The spatial profiles of the local velocity distribution of v_x and v_y are obtained from our simulation. They are shown in Fig. 4.2. All of the local velocity distribution functions $f(v_x)$ are found symmetric, while $f(v_y)$ are asymmetric in the side bins. We also investigate the spatial profiles of the skewness as functions of the coefficient of restitution and of the number of particles.

Skewness, when it is non zero, demonstrates the asymmetry of the distribu-

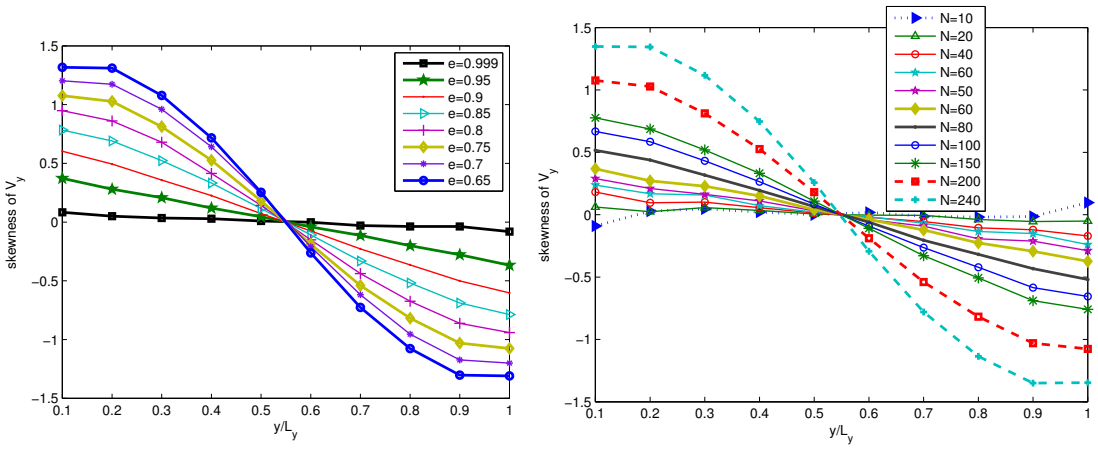

Figure 4.3: Variation of skewness in the cell, as a function of the restitution coefficient and of the particle number N. Here, y axis is the vibration direction.

tion. We recall that skewness of variable p with n sample points is its third standardized moment, defined as

$$skewness = \frac{\frac{1}{n}\sum_{n}^{i=1}(p_i - \bar{p})^3}{(\frac{1}{n}\sum_{n}^{i=1}(p_i - \bar{p})^2)^{3/2}} \tag{4.1}$$

Here p_i is the variable value of sample point i, $\bar{p}$ is the mean of all n sample points p_i, n is the number of the sample points . A negative skewness indicates the distribution has a left-side tail, while a positive one indicates a right-side tail.

Fig. 4.3 illustrates the skewness of the v_y spatial profile as a function of either the restitution coefficient or of the number of particles. For simulations with a restitution coefficient which is merely one and the number of particles N which is small (so that dissipation of the sample is small, we found that $e_p = 0.999$, skewness is approaching a constant value, zero. This means for an elastic granular gas the long range boundary effect does not exist even under boundary heating. For coefficient of restitution smaller than 1 (inelastic particle cases), skewness S along y-axis fails to be a constant. Especially, S is most pronounced near the boundary, and is zero at the center of the cell. Also skewness is positive for the left boundary layer of the cell and negative for the right boundary layer of the cell. Moving towards the box center, the value of skewness decreases slowly, and linearly near the box center. At the box center, skewness becomes zero (due to

symmetry). It shows that the boundary effect is not only at the layer of particles next to the boundary, it extends into the cell, and therefore it is a bulk effect, or a long range effect. The amplitude of effect depends on the inelasticity of the particles. It is more profound as the system is more dissipative or the restitution coefficient of the particles is smaller.

Previous studies only consider central region of the box. So they could ignore the boundary. But here we show that except at the center the skewness is non zero. This approach obviously reduces this boundary effect because the skewness in central area is smaller than the boundary area. It is reasonable that the velocity distribution in the central area is different from the velocity distribution near the wall[127]. It is also obvious the velocity distribution in the central area is close to be symmetric in the central part; this is imposed by symmetry[127]. However, it is not correct to restrict the description to this state, since skewness is only zero at the center as it is shown here (Fig. 4.3).

We study the role of the coefficient of restitution in the skewness S value(this one is shown in Fig. 4.3(left)). So, Fig. 4.3 demonstrates that the higher the inelasticity becomes, the higher the change of the skewness amplitude gets. The effect is not only shown at the boundary bin, but also it extends into the whole cell(except at the center), since all skewness curves at different coefficients of restitution meets in the centre of the box where they pass zero. This result is completely different from previous hydrodynamic treatment. In previous hydrodynamic considerations, the boundary layer effect only exists in a thin layer [122]. But here, we find that from the spatial profiles of skewness this boundary effect in vibro-fluidized granular gas can be a bulk effect. This shows that the hydrodynamic description for the granular system needs further consideration since it never includes this in the described facts. Comparing with our previous experimental results of Chapter 3[13],we find that the skewness dependence , which is non zero does not always vary linearly when it is obtained from simulations, as we see from Fig. 4.3 (left). This is different to what we did observed in experiments (Fig. 3.7). A possible explanation is that the aspect ratio of the length of the cell to the particle diameter L/d in simulation is much larger than in the experiment: the ratio is 9 in the Airbus experiment[13] , while it is 150 in our simulation here.

Fig. 4.3reports also the variation of S at the left boundary bin in terms of the

coefficient of restitution. These values exhibits a bijective relation, which shows the strict ordering between S_{max} and e. It seems that S varies nonlinearly with the coefficient of restitution.

For the sake of simplicity, we use a phenomenological model to describe this asymmetric distribution [115] of $f(v_y, y)$. It is assumed to be the superposition of two Gaussian functions:

$$f(v_y) = \frac{1}{N}(\alpha exp\frac{(v_y - \xi)^2}{-T} + exp\frac{(v_y + \alpha\xi)^2}{-T}) \tag{4.2}$$

where the factor $N \equiv \sqrt{\pi T}(1+\alpha)$, $2k_B = 1$, $T = b(T_g + t_{yy})^2/4$[115], T_g is entropy temperature. An important assumption is that the parameters(N, ξ, α)in this expression are calculated to make sure the mean velocity is zero, $\int vf(v_y) = 0$. The local velocity distribution is well fitted by this function, as is done in[115].

By using the above local velocity distribution function (the superposition of two Gaussian functions) and the definition of the skewness, we can obtain the skewness S equation:

$$S = \frac{-\alpha\xi^3(\alpha - 1)}{(\frac{1}{2})^{3/2}\sqrt{\pi T}(1 + \alpha)(T + 2\alpha\xi^2)^{3/2}} \tag{4.3}$$

We find that the S is related with parameters α, T and ξ. In the cell center, the two Gaussian functions merge into one, $\xi = 0$. Therefore skewness is equal to zero, $S = 0$, in the center. Except for this center point, all other points have non-zero S with a value depending on parameters α, T and ξ. The advantage of using a probability distribution function is that S can be obtained with known values of parameters α, T and ξ. However, the "heating" wall model[17] is such as the velocity of a particle which touch the wall gains a speed which pertains to Maxwell distribution $exp - (v^2/v_0^2)$ given by the wall temperature T. We find that the local distribution $f(v_y)$ in the boundary layer only is made of a broad tail with some maximum on one side of v, says v_+, and a high narrow peak at $v = 0$ on the other side of v, says v_-, rather than a clear two peaks. This is normal, and it is included in the hypothesis.

The fat tail of the local velocity profile near the boundary can be explained as follows: at the left boundary, for instance, the mean velocity v_y^+ of particles

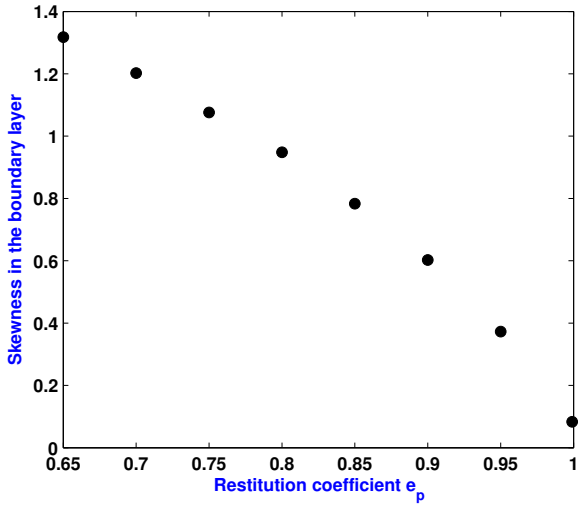

Figure 4.4: Skewness in the boundary layer in term of restitution coefficient.

moving away from the wall, has gained some velocity (or some energy) from the wall. So V_y^+ has to be is larger than that of v_y^- since these ones have passed through the center of the gas where they have loosed energy by collisions (i.e. particles moving toward the wall, lose energy through particle-particle collisions). Since there is no mean flow in a steady state, the mean velocity ($< v_y >$) shall be zero, the particle number with v_y^+ is therefore smaller than the number of v_y^- as observed in Fig. 4.3(right), and the skewness at the boundary layer is greater than layers away from the boundary.

Next we have to fit the variations of a (α) with y. This is done in Fig. 4.5.

4.4 Anisotropy of the mean free path

Mean free path is an important and fundamental concept. In general, it is defined as the average distance that a particle travels between two successive collisions. In the dilute classical gas, it is expressed as:

$$l = \frac{1}{\sqrt{8}\rho d} \tag{4.4}$$

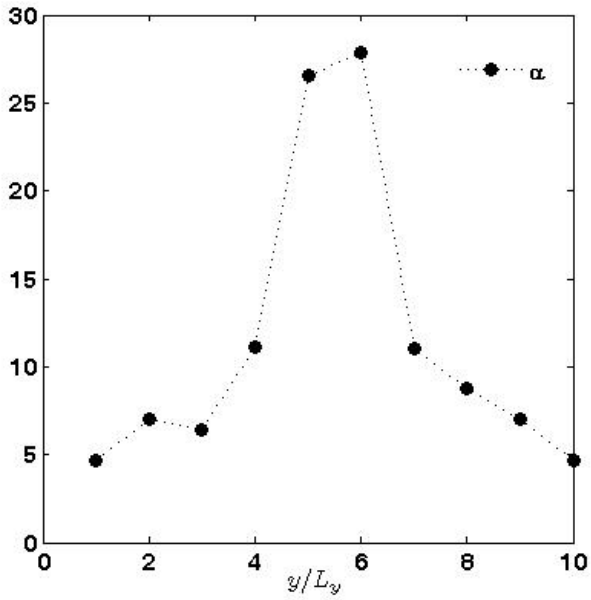

Figure 4.5: The values of the fitted parameters, α.

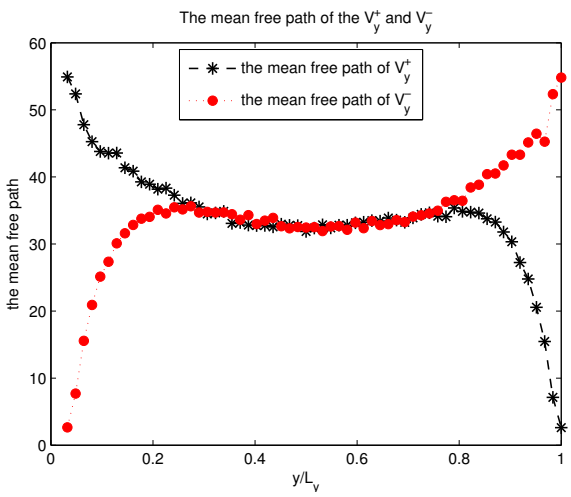

Figure 4.6: The mean free path of v_y^+ and v_y^-. The particle $N = 360$, the $e_p = 0.85$ and the $e_w = 0.95$. The box is $300 * 300$. The particle diameter is 2.

where ρ is the number density. But this definition requires that all particles are identical, have similar speed and the system is homogeneous. Here most of these assumptions are not satisfied: The area fraction in our simulation is small, it ranges from $3.49 * 10^{-4}$ to 0.0126, and varies with position. It seems that this mean free path expression should work, however, let us consider the situation described above. The local velocity distribution is far from the classical ones, though the global velocity distribution seems near the classical ones(one is Gaussian, the other is the exponential distribution). The boundary long range effect make the mean free path concept breakdown[13]. It is necessary to modify the definition and to define new categories of mean-free-path according to the sign of the velocity v_y component in the vibration direction. For the experiment, it may be difficult. But for the simulation, this is quite easy. In fig. 4.6, the statistical results of the mean-free-path l^+ for the v_y^+ and l^- for v_y^- are presented. It agrees well with our expectation. l^+ and l^- are different and varies as a function of y. In the box left side, the l^+ is larger than the l^-. Similarly, the l^- is larger than the l^+ in the cell right side. It is obvious that the previous mean-free-path expression Eq. 4.4 can not show the Fig. 4.6.

4.5 Energy Sink

Since our system dissipates, it is instructive to measure the effective energy loss. In the forgoing, the energy loss is described in the hydrodynamics modelling of the granular gas with the hard sphere by the following expression $-\zeta(1-e^2)nk_BT$; this is a mean field theory, where $\zeta = Cn(r,t)T(r,t)^{1/2}$, $n(r,t)$ is the local number density, C is a constant depending on the dimension[122]. This is equivalent to have sinks of heat randomly distributed in the gas. Based on asymmetric distribution, we believe that the energy loss also should be examined by the velocity sign.

We count all the collision pairs in our simulation including the particles that collide with the wall. These collisions are grouped according to the direction and sign of the velocities. Then the energy loss can be collected directly from collisions. It means the energy loss $\Delta E_{i|j}$ is divided into four parts: $\Delta E_{i|j}^{v_x^+}$,$\Delta E_{i|j}^{v_x^-}$, $\Delta E_{i|j}^{v_y^+}$ and $\Delta E_{i|j}^{v_y^-}$. $\Delta E_{i|j}^{v_x^+} = \sum((v_x')^2 - v_x^2)/2N_c v_{driven}^2$ at $(v_x > 0)$, where v_x' is

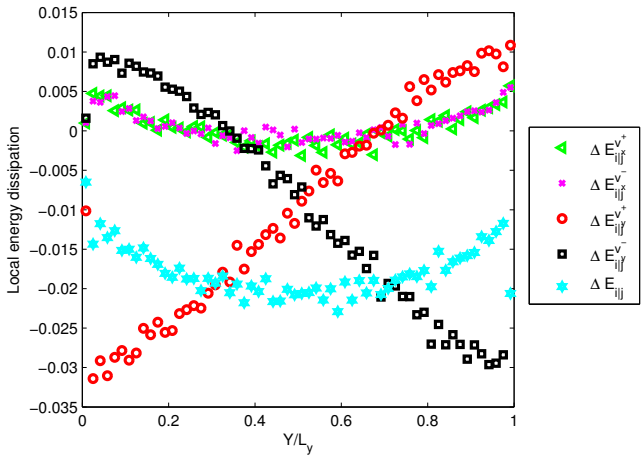

Figure 4.7: the energy loss spacial profiles. The particle $N = 360$, the $e_p = 0.85$ and the $e_w = 0.95$. The box is $300 * 300$. The particle diameter is 2.

the velocity component in x axis after a collision and v_x before a collision. Each energy loss is scaled by the $N_c v_{driven}^2$, where N_c is the total collision times, v_{driven} is the driven velocity. Fig. 4.7 gives a typical result of our simulation. It can be seen from the figure, the energy loss is anisotropic since curve with v_x is different from curve with v_y. Further more it depends on the way in v_y^-, since v^- gains energy in the left part of the cell, but looses energy in the right part one; and it is reversed for v_y^+ which looses. $\Delta E_{i|j}^{v_x}$ and $\Delta E_{i|j}^{v_y}$ are different totally. The two components of $\Delta E_{i|j}^{v_x}$, $\Delta E_{i|j}^{v_x^+}$ and $\Delta E_{i|j}^{v_x^-}$, are almost equal to each other. On the contrary, $\Delta E_{i|j}^{v_y^+}$ and $\Delta E_{i|j}^{v_y^-}$ show great difference. In left side of the box, the particle of $v_y > 0$ losses the most part of energy, while the particle of $v_y < 0$ seems to get energy at first and to loose energy increasing as moving from the boundary to the center. This results is totally different from our expectation which is $\Delta E_{i|j}^{v_y^+}(y) = \Delta E_{i|j}^{v_y^-}(y)$.

4.6 Hydrodynamic field

One can try to extend hydrodynamics formulation to extend it to include dissipation by collisions in a low density gas. We start on the basis of a one-particle

distribution function f

$$\frac{\partial f}{\partial t} + \vec{v} \cdot \nabla f = -\zeta(f - f_0)$$

The granular gas field is then described by the following 3 equations[122]:

$$\partial_t n + \nabla \cdot (n\vec{u}) = 0$$

$$\partial_t \vec{u} + \vec{u} \cdot \nabla \vec{u} + (mn)^{-1} \nabla \cdot \mathbf{P} = 0$$

$$\partial_t T + \vec{u} \cdot \nabla T + 2(dnk_B)^{-1}(\mathbf{P} : \nabla \vec{u} + \nabla \cdot \mathbf{q}) + T\zeta = 0$$

where $\mathbf{P}$ is the pressure tensor, $\mathbf{q}$ is the heat flux and ζ is the cooling rate associated to the energy dissipation. Furthermore paper[122] proposes a local Maxwellian distribution for ($f = exp(-v^2/kT)$. It is also said that a hydrodynamic description exists for Navier-Stokes till a development at second order in ϵ, i.e. at order ϵ^2 if $\epsilon^2 > 1/2$, where ϵ is the coefficient of restitution.

Obviously, it is not right in our system. Furthermore, since the real local velocity distribution is far from the Maxwellian distribution, it is not known whether these equations hold or not. In the other hand, we should also discuss the shape of the energy loss; it is written as

$$\zeta(\mathbf{r}) = cn(\mathbf{r})T^{1/2}$$

In fact, there are many works already which try to discuss the local equation of state for a granular gas[12].

Here, we wish to study " hydrodynamic" laws to which the granular gas obey from the basis: we need to introduce a statistical description before introducing the mean effects we had to observe and understand better the system. This means that we need to introduce statistic of some parameters. Considering the anisotropy, parameters we had studied v_x, v_y statistics, and show they have to split into independent values for the local mean in x and y directions. Furthermore, to gain insight into the local velocity; asymmetry of v_y distribution has to be introduced too. It means that we need four hydrodynamic parameters or four components, such as the pressure components: $p_x^+(y) = \sum(v_x^+(y))^2$, $p_x^-(y)$, $p_y^+(y)$,

$p_y^-(y)$. Similarly, temperature and the number density are divided into $T_x^+(y)$, $T_x^-(y)$, $T_y^+(y)$, $T_y^-(y)$, $n_x^+(y)$, $n_x^-(y)$, $n_y^+(y)$, $n_y^-(y)$.

So, as for the x direction, all the distributions of the velocity components v_x are the symmetric, so, $p_x^+(y) = p_x^-(y)$, $T_x^+(y) = T_x^-(y)$, $n_x^+(y) = n_x^-(y)$. This agrees well with the classical view. However, for the y direction the velocity distribution of v_y, are no more symmetric, and the complete description fails. Fig. 4.8, 4.9 and 4.11 show pressure, temperature of the y components for different number of grains and for different restitution coefficients. We will describe their variations before describing the evolution of the number densities.

4.6.1 Pressure

Typical results obtained by simulations of the variations of the $p_y^+(y)$ and $p_y^-(y)$ as a function of the restitution coefficient are shown in Fig. 4.8 (left). All curves show a great difference between $p_y^+(y)$ and $p_y^-(y)$. $p_y^+(y)$ is the largest in the left boundary wall and decreases linearly with y, while $p_y^-(y)$ is axis symmetrical with $p_y^+(y)$. So the sum $p_y(y)$ of $p_y^+(y)$ and $p_y^-(y)$ still is constant. This result has been proved by J. Villain [93]in the case of dilute systems.

This is the main reason why most work misunderstand the real nature of this problem: In classical gas theory, the $p_y^+(y)$ should be equivalent to $p_y^-(y)$ everywhere. Here, $p_y^+(y) \neq p_y^-(y)$ prove that the granular gas differs from the classical molecular gas. The value of $p_y(y)$ is decreasing with the coefficient restitution, however, the slope of $p_y^+(y)$ of the same particle number and at various restitution coefficient seem close, see Fig. 4.8 (left).

Further more the difference between P^+ and P^- shows that the system is not in static equilibrium: it shows that if we separate the box by a plane perpendicular to vibration, the solution will break at once, except when the plane is chosen to pass through the middle of the box.

4.6.2 Temperature

The granular temperature is defined as $T(x) = [T_x(x) + T_y(x)]/2$, where $T_i(x) = (v_i - \bar{U}_i)^2$, $i = x,\ y$, U_i is the mean velocity and $U_i = 0$ for the steady state. Anyhow, this notion is perhaps difficult to use here: Firstly, we know that the

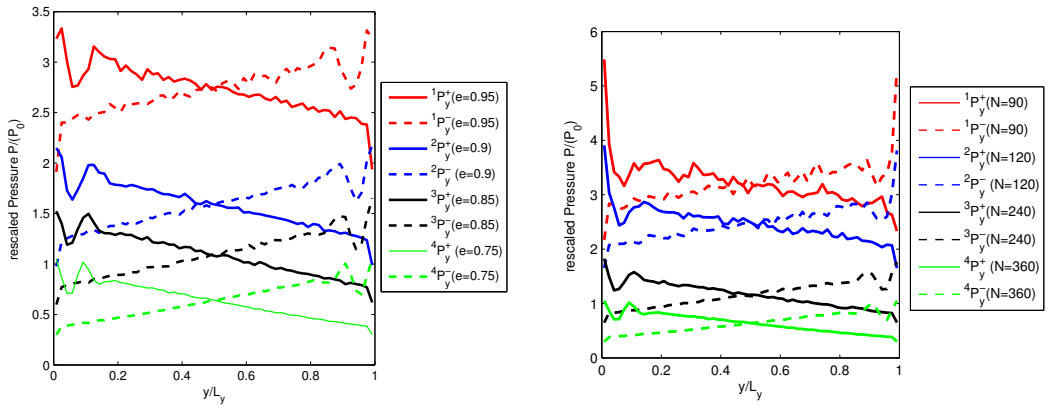

Figure 4.8: Variations of pressure $p_y^+(y)$ and $p_y^-(y)$ for different coefficient restitution e_p (left) and different total number of particle N. $e_w = 0.95$. The box is $300 * 300$. $N = 360$.

analogy with temperature definition coming from molecular gas theory is not so certain[88–90]; secondly, we need to define here two Temperature T depending on the directions (x and y) of motion; thirdly, due to the local velocity asymmetric distribution, we need to calculate the temperature components according to the sign of v_i, $T_i^+ \equiv < v_i^2 >$[13], $i = x,\ y$. In [13], we shew that energy equipartition law does not persist. The temperatures $T_y^+(y)$ and $T_y^-(y)$ are not equal to each other along y direction, although $T_x^+(y)$ is about equal to $T_x^-(y)$. Fig. 4.9 shows the spatial profiles in our simulation. These results also agree with our experiment results. Except for the cell center, for which $T_y^+ = T_y^-$, we find $T_y^+ \neq T_y^-$ everywhere, as in the experiments. This also agrees with our experiment results [13] (see Chap 3). Because of the dissipation in the system and since energy is injected from the side, the temperature falls down from the boundary to the center in the case of excited particles.

Furthermore, one observes the more the dissipation, the larger the difference between $T_y^+(y)$ and $T_y^-(y)$, while $T_x^+(y)$ is almost equal to $T_x^-(y)$. Here we introduce a parameter $q(y) = T_y^+(y)/T_y^-(y)$, which is the ratio of the two temperatures $T_y^+(y)$ and $T_y^-(y)$. The spatial profile of $q(y)$ is shown in Fig. 4.10. $q(y)$ is merely constant at large e:$q(y) \approx 1$, when $e = 0.999$. Furthermore, variations of q(y) vs y is linear in log-linear scale of Fig. 4.10; this tells $ln(q) = -ky$. So, assuming

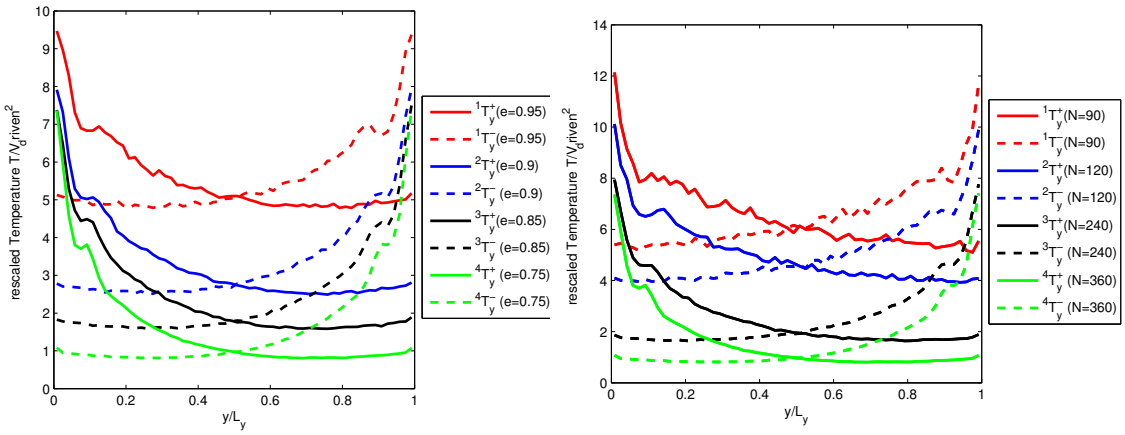

Figure 4.9: Variations of temperature $T_y^+(y)$ and $T_y^-(y)$ for different coefficient restitution e_p(left) and for different number of particle N(right). $e_w = 0.95$. The box is $300 * 300$. $N = 360$.

$ln(q) = -ky$, we obtain

$$\frac{T_y^+(y)}{T_y^-(y)} = e^{-ky} \tag{4.5}$$

The ratio of $T_y^+(y)$ and $T_y^-(y)$ drops exponentially. k can be measured for the different restitution coefficient from Fig. 4.9. So we plot its value as a function of e in Fig. 4.11. This shows that k depends on coefficient of restitution monotonically with a negative slope in fig. 4.11.

4.6.3 The number density

The number density $n_y^+(y)$ and $n_y^-(y)$ in each way ($+y$ and $-y$) are shown in Fig. 4.12 for different ball numbers. The larger the number of particles is, the sharper the peak of $n_y^\pm(y)$ is. Furthermore, $n_y^+(y)$ and $n_y^-(y)$ are different from each other except at the center of the box. This fact demonstrates there is no micro "static" state in the granular system which corresponds to a real local equilibrium, for which one should have $(n_y^+(y) = n_y^-(y))$ everywhere and $P^+ = P^-$ every where. At equipartition, $n^+ = n^-$; it is obtained when $n^+ = n^- = n/2$. So the equipartition is reached when $n^+/(n^+ + n^-) = n^-/(n^+ + n^-) = 0.5$. Fig. 4.13 shows that the equipartition occurs at the same point, whatever the ball number, when we use the same excitation. This is linked to symmetry of excitation.

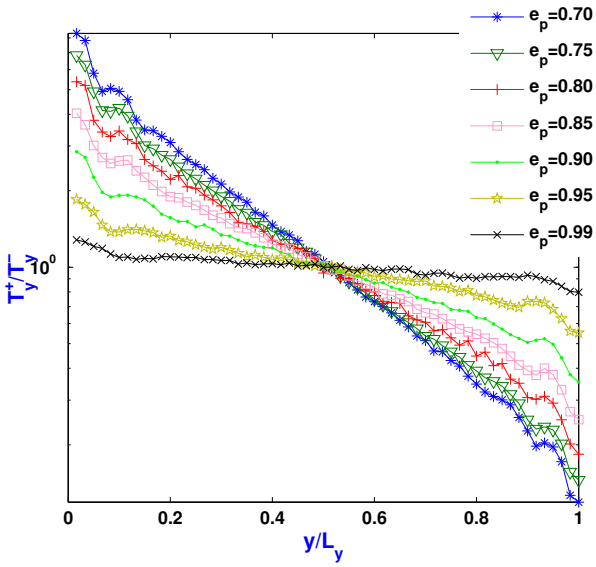

Figure 4.10: Semi-logarithmic variation of the $T_y^+(y)/T_y^-(y)$ vs y position in the cell. The number of particles N is 360, the area fraction $\phi = 0.0126$ .The size of the cell is $(300r * 300r)$, r is the particle radius.

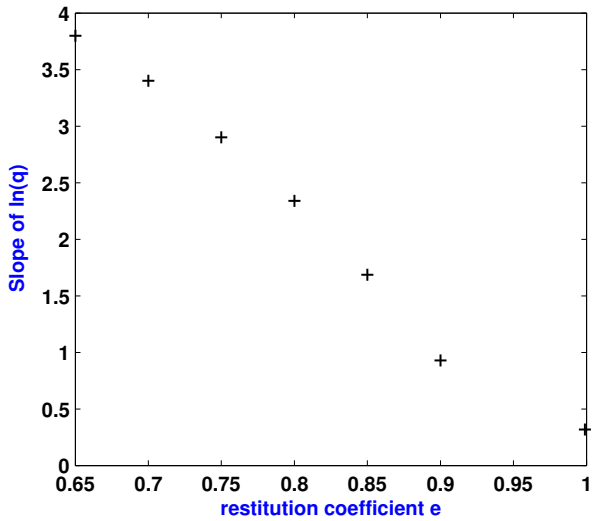

Figure 4.11: Variations of k, i.e the slope (in semi-log coordinate of $\tau(y)$) (see Fig. 4.10) of $ln(q(y)$ in terms of restitution coefficient. The number of particles N is 360, the area fraction $\phi = 0.0126$. The size of the cell is $(300r * 300r)$, r is the particle radius.

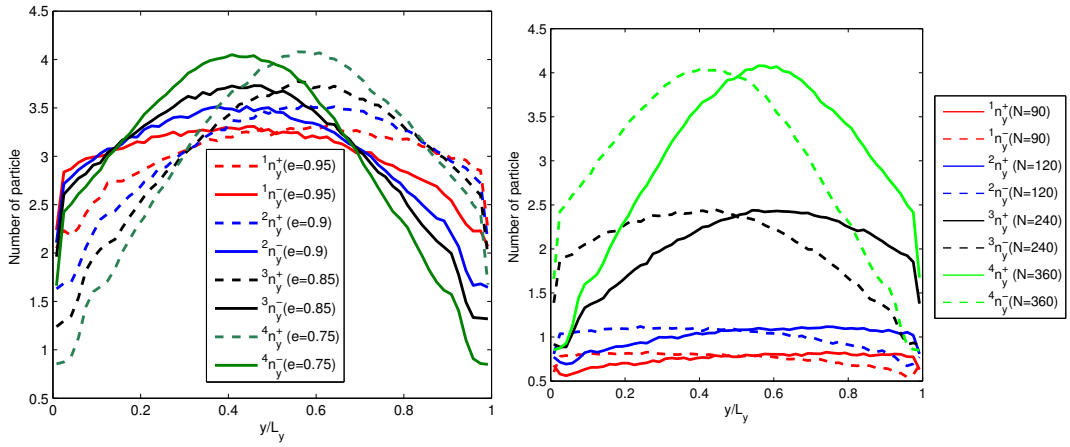

Figure 4.12: The number density spacial profiles $n_y^+(y)$ and $n_y^-(y)$ with various coefficient restitution e_p. $e_w = 0.95$. The box is $300*300$. $N = 360$ for left figure.

Elsewhere the distribution is different since n^+ different n^-. Furthermore the distribution of $n = n^+ + n^-$ depends on y and is maximum at the cell centre. This makes more intricate the problem of calculating the local mean-free-path with the number density, as discussed in preceding section 4.4. It is clear that the mean free path does depend not only on $n(y)$ but also on the set $n_y^+(y)$, $n_y^-(y)$, $v_y^+(y)$ and $v_y^-(y)$; so it varies with the particle velocity.

4.6.4 Velocity field

In most study, the velocity field is a stationary-state[12]; and such a stationary state shall get constant pressure along y axis [68] according to hydrodynamics flow. the pressure shall be constant[67] along y axis. Here we show in Fig. 4.14, that the mean velocity is also zero. However, we also detected the $\bar{v_y^+}$ and $\bar{v_y^-}$. They are different locally. This is shown also in Fig. 4.14, where $\bar{v_y^+}(y)$ and $\bar{v_y^-}(y)$ is not constant in the value but their mean flow is zero. In other words, we can say the system is in global steady (or stationary) state; but this state is in complex dynamics where two fields exists one in $+y$ direction and the other in $-y$ direction. These two fields are interacting together to ensure stability of the solution. So we have two velocity fields. This is not strange. Because the stationary state is different from equilibrium state.

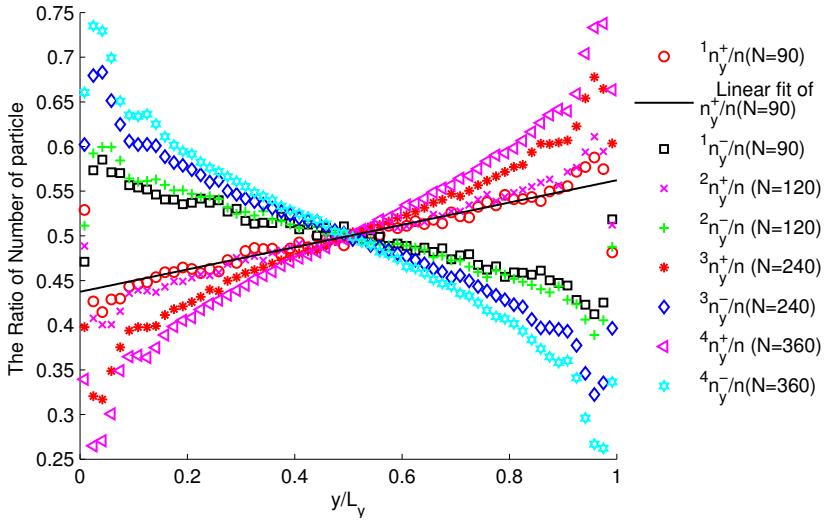

Figure 4.13: The number density Vs N

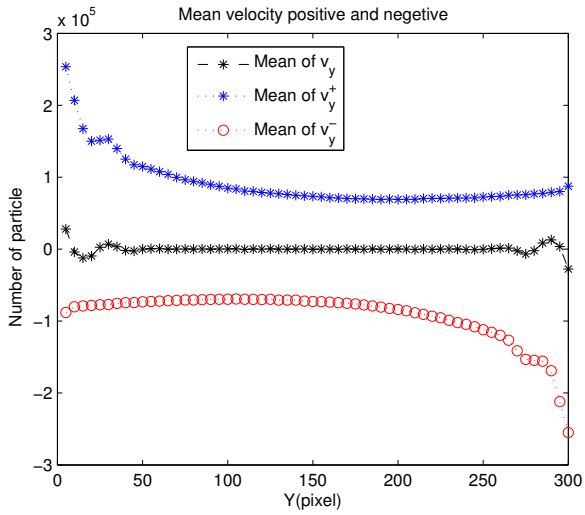

Figure 4.14: the mean velocity the particle $N = 360$, the $e_p = 0.75$ and the $e_w = 0.95$. The box is $300 * 300$. The particle diameter is 2.

4.6.5 The heat flux

Turning now the Fourier law of heat, we can use the classic description for a gas; then we may test this description and see whether it is satisfying or not.

So, the heat flux q is given by $q = -\kappa\nabla T$, where κ is the heat conductivity, T is the temperature. It needs to be emphasized that the heat flux here only contains the kinetic part. For an inelastic system [132], it is expected generally the heat flux is predicted by Chapman-Enskog expansions of Boltzmann kinetic equation, $q = -\kappa\nabla T - \mu\nabla n$, where μ is a transport coefficient, n is the number density. There are relations between these transport coefficient as shown by Einstein. The heat flux, q[127, 132], contains two parts, the free streaming of the particles q_{kin} and the translational energy changes due to collisions q_{int}. q_{kin}, q_{int} in the vibrating direction. However, the sum of q_{kin} and q_{int} is found linear. More, q_{kin} is of the same order of magnitude as the kinetic contribution, q_{kin}. This means the collision part is important. Article[127] proposes some generalized-Fourier modeling, which seems to work well as a constructive law for each flux when the restitution is larger than $e_p > 0.99$. So, it seems to hold as a constitutive relation for the heat flux. However, for stronger inelasticity (i.e. when the coefficient $e_p < 0.99$) [127], their modeling fails; the law $q = -\kappa\nabla T - \mu\nabla n$ fails, too.

Now considering simulation at low density ($\phi = 0.012$) and high inelasticity $e_p = 0.75$, we have to consider what we found previously, i.e. the existence of two temperatures. So, we can measure the heat flux q_{kin}, dividing it into four parts: q_x^+, q_x^-, q_y^+, q_y^-, such as $q_x^+ = \sum_{i=1}^{N} \frac{m(v_x^+)^2}{2} v_x^+$, depending of the surface from where it merges. This is shown in Fig. 4.15 (right side). Our system is far from equilibrium but still in a dynamics steady state. In this case, we know that even the temperatures in $+$ and $-$ directions are different in the vibration direction. Even the temperature looks different from the classical temperature, which is discussed in the above section.

Indeed from the right part of Fig. 4.15, one can see. So, we suggest introducing a new method to calculate the heat flux from four parts and examine the heat flux in a dissipative granular gas.

The spatial profiles of Fig. 4.15 are rescaled by the vibrating velocity v_ω to the third power v_ω^3. One sees:

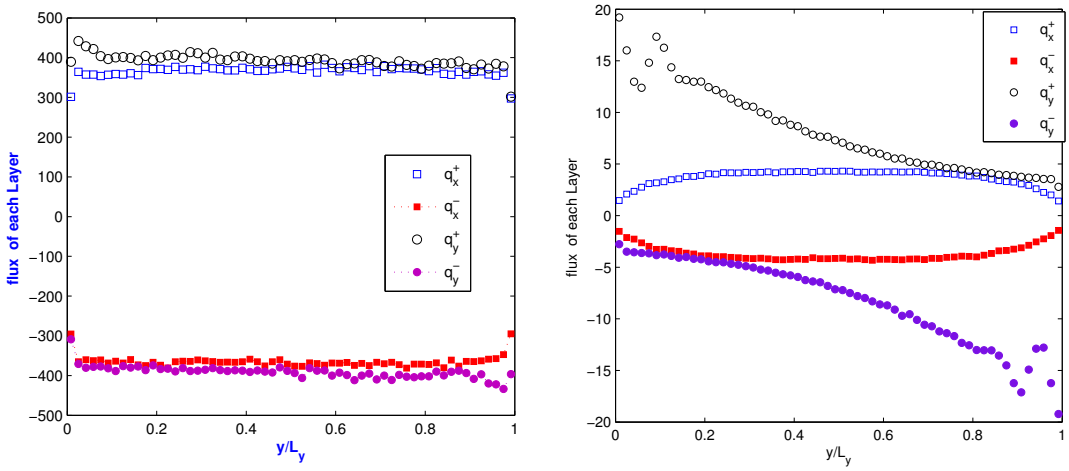

Figure 4.15: The spatial profiles of the four components of the rescaled heat flux q_{kin} in $e = 0.99$ (left) and $e = 0.75$(right),q_x^+, q_x^-, q_y^+, q_y^-. The number of particles is $N = 360$, the area fraction $\phi = 0.0126$.

1. For near elastic situation, absolute values of $q_x^+ = q_x^-$, $q_y^+ = q_y^-$.

2. For inelastic situation, absolute values of q_x^+, q_x^- are equal and symmetric about the middle of the system, but q_y^+ and q_y^- are asymmetric, and absolute values of q_y^+ and q_y^- are not equal to each other.

3. For the same number of particles and vibration velocity, the values of flux in elastic and inelastic systems are quite different. It is clear that the reason of the difference between q_y^+ and q_y^- for inelastic situation is not only limited to boundary, but also system inelasticity.

4. In the case of inelastic system, the spatial profiles of number density vary, which is also leading to a second heat flux term (the factor ∇n in the equation $q = -\kappa\nabla T - \mu\nabla n$). So we need to discuss the number density spatial profiles in our simulation. In[13], n_x^+ and n_x^- are equal to each other, while the two components of the number density, n_y^+ and n_y^- are not equal to each other except at the box center point (y axis is the vibration direction). In 1-phase hydrodynamics, the spatial profiles of n_y^+ and n_y^- is expected to be equal everywhere. Our simulation results confirm the spatial profiles of n_y^+ differ from n_y^+ in various coefficients of restitution(shown in Fig. 4.12).

5. Furthermore, we find that the more the dissipation is, the thinner the density peaks are. So, the larger the difference between n_y^+ and n_y^- are, the larger the heat flux exchange. This is consistent with the difference between the temperature T_y^+ and T_y^- . All these results demonstrate the necessity to analyze the heat flux in details and especially the contribution of both the positive and the negative parts. This point should be considered in the inelastic heat flux theory and need to be explored in the future work. This result highlights the difference of heating function between the two boundary walls.

4.7 The mean free path

The mean free path involved in granular gases is an essential concept, which is defined as the average distance that a particle travels between two successive collisions. It is characterized the particle collisions and also bridges the microstructure inhomogeneity to macroscopic physical length scale even though lack of scale separation between macroscopic scales and microscopic ones for granular gases[90, 133].

The mean free path is widely applied in the granular media physics. For instance, It is a criteria that determines whether granular dynamics can be described by the hydrodynamic or not[70] for granular gases. If the mean free path of a granular system is lower than a value, we supposed the hydrodynamic description could be applied in such granular gases system. Besides, the mean free path is used to calculate the transport property for the granular media, such as viscosity[126] of the granular flow in many literture[122]. So how to calculate the mean free path in the granular gases is a fundamental question.

Grossman et al.[66] gave mean free path expressions in the low and the high density limits for the inelastic granular gases. The low density expression is the same with the mean free path in the molecular gases, while the high density one is based on the close-packing density. These expressions work well when the system is near elastic condition. J. Javier Brey et al.[122] masterly used the local mean free path replacing the coordinate to obtain the temperature spatial profiles for a granular gas fluidized by a vibrating wall and a reflecting one. The local mean

free path could characterize the local inhomogeneity which generally exists in inelastic granular gases.

However, Tan and Goldhirsch[133–135] study the mean free path in an uniform shear flow, elucidating the dimensional shear rate is not small for the strong dissipation and the 'true' mean free path is larger than the equilibrium mean free path. If we analogize the local mean free path from the uniform shear flow to granular gases fluidized by the boundary heating, the local mean free path is supposed to be larger than the Grossman's [66] low density equilibrium-based expression.

In another point of view, the mean free path itself is a concept based on the equilibrium state. One[47] cannot assume a prior 'fast local equilibration' or use local equilibrium as a zeroth order distribution function unless the system is nearly elastic. If its distribution is Maxwell-Boltzmann distribution, the local mean free path in the granular gases could be likened to be the classical calculation in the molecular gas. Whereas the velocity distribution of granular gases vibrated by the boundary is exponential, demonstrated by many experiments[52, 55, 136] and simulations[81]. Furthermore, for the local velocity distribution, two peaks of local velocity distribution were found in the simulation[122]. This phenomenon was confirmed in the micro-gravity experiment[13]. A gradual transition of the local velocity distribution from the boundary to the bulk in the box center are found. The local velocity component distribution, $f(v_y)$ (the vibration direction is y axis), appears two peaks in the marginal layer, melting into one peak in the box center gradually, which could be demonstrated by the skewness of $f(v_y)$s. Skewness is a measure of asymmetry of a distribution, which could be positive, zero and negative that indicates that strength contrast between the distribution tail on the right side and the left side. The skewness of $f(v_y)$ in the experiment reduces linearly from one side of box to the other, passing the zero in the box center. Asymmetric velocity distribution is everywhere, except for the box center point. All these prove that the granular gas is far from the local equilibrium. Local equilibration also need to be scrutinized in granular gases. That is why it is necessary to investigate the local free path in vibro-fluidized granular gases.

Given all of that, what is 'true' local mean free path for granular gases heated by boundary? We need to begin from checking the local velocity distribution in

our simulation. In this paper, we do a detailed investigation into the free path in our simulation results. The local mean free path is investigated directly from the tracking particles in the simulation. Our results show the local mean free path for granular gases is larger than the equilibrium expression given by Grossman, which is consistent with the uniform granular shear system. Moreover, considering the velocity distribution asymmetric, we find the local mean free path also have the direction. Two local mean free path l^+ and l^- are defined according to the sign of the velocity component in the vibration direction. Our results demonstrate l^+ and l^- are different with each other. With double-Maxwellian velocity distribution model, an analytic formula of local mean free path is deduced. The quantitative predictions of the theory are compared with event-driven simulation results. A good agreement is achieved for both l^+ and l^-.

The outline of this section is as follows. In Sec. I Event driven molecular simulation method is introduced. In Sec. II The local free path under various conditions are presented, compared with the present theory prediction. In Sec. III The local velocity distributions are investigated. In addition, the major peaks are fitted by a Gaussian function. The spatial profiles of the fitting results of the parameter will presented to confirmed the double Maxwellian model. In Sec. IV The analytical resolution of the local free path are given. The comparative results between our theory and the simulation are discussed. We will draw our conclusions in V.

4.7.1 Simulation Model and analyse method

A granular gas consisted of N inelastic disks with diameter $d = 1$ and mass m is studied in a rectangular box. The idealized sawtooth manners presented in[12] are adopted in y direction. If the velocities of the particles before collision are $\mathbf{v}_1$ and $\mathbf{v}_2$ and after collision $\mathbf{v}_1'$ and $\mathbf{v}_2'$, let $\mathbf{v}_{12}$ and $\mathbf{v}_{12}'$ be the relative velocity of the particle before collision and after collision, then an inelastic collision satisfy that

$$\mathbf{k} \cdot \mathbf{v}_{12}' = -e(\mathbf{k} \cdot \mathbf{v}_{12}) \tag{4.6}$$

where $\mathbf{k}$ denotes the unit vector directed from the center of the first sphere to

that of the second one, e is the restitution coefficient with the range [0, 1].

For the diving wall, we adopt the driving way which is used in the work[12], a sawtooth driving wall with vanishing amplitude A and diverging frequency ν in x direction. So each particle colliding with the wall has the post-collision velocity:

$$\mathbf{v}' = \mathbf{v} + \Delta\mathbf{v}_{pw} \tag{4.7}$$

where

$$\Delta\mathbf{v}_{pw} = (-2v_x \pm v_{drive})\mathbf{k}_x \tag{4.8}$$

To obtained the asymptotic dynamics of these fitting parameters, we use a coarse graining method[87]. The coarse graining function, $\Phi(\ \mathbf{R})$, defines spatial "windows" with width $\delta x = L_y/270$ (270 strips are fixed in all simulations, so the δx are changed according to the L_y) along x direction and length $\delta y = L_y$ along y direction. The "window" moves step-by-step along y direction(here,the step size is 1), which means "windows" overlapping one with another. All the particles appearing in one "window " count towards the total amount. In our case, there are 270 windows in x axis. For instance, When $L_x = 300$, $\Phi(\ \mathbf{R})$ begins form $x \subseteq [0\ 30]$, then [1 31], ..., until [270 300] .

It needs to be emphasized that our results are obtained from the simulation. When one particle collide with another, their positions are stored. Then the next collision happen, the free path can be calculated directly from the last collision position.

4.7.2 The local mean free path

In work[66], the mean free path is expressed in terms of the density and the diameter. In the low density limit, it is

$$l = \frac{1}{\sqrt{8}\rho d} \tag{4.9}$$

on the other hand, in the high density limit, one has

$$l = \frac{\rho_c - \rho}{2\rho_c} d \tag{4.10}$$

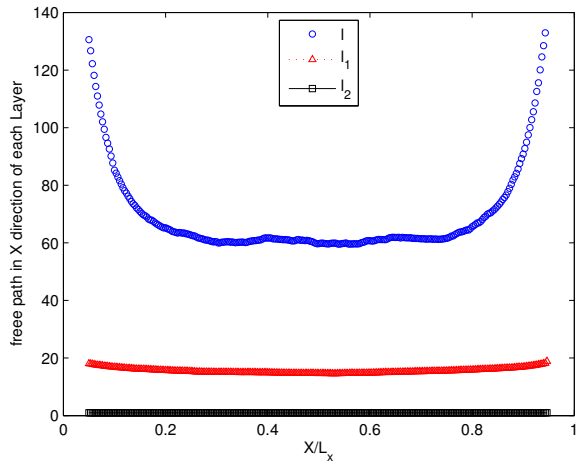

Figure 4.16: The spatial profiles of local free path l, l_1 is the Eq.4.9 and l_2 Eq.4.10.($L_x = L_y = 300$, $e = 0.99$, $N = 1000$, $V_{driven} = 5$).

where ρ_c is the close packing density, ρ is the local number density and d is the diameter of the particle, $\rho_c = 2/(\sqrt{3}d^2)$.

In Fig.4.16, measurements of local free path l reveal that the quantitative value of l is larger than approximation of the molecular gases, especially in the boundary layer. Here, the area fraction is $\phi = \pi d^2 N/4L_xL_y = 0.034$, and the global mean free path calculated from the molecular gases is $l_g = 1/\sqrt{8}\rho d = 31.8$. So granular gas is dilute and near elastic($e = 0.99$), whose parameters are almost the same with papers[66]. l in the boundary is nearly equal to the half of the box length, which means that particles could fly free till arriving at the box center. Then l falls down when leaving the boundary, and reach a plateau finally. We compare our strong dilute and nearly elastic simulation results with the theory predictions of Eq. 4.9 and Eq. 4.10. It is clearly that the most of local free path l are twice time of l_g. The simulation results of l are higher than the l_g, even for the low density limits prediction, Eq. 4.9.

The most expected explanation for this is that it has a nonzero mean velocity, then it would be similar with the uniform shear system[133]. In shear granular system[133], the particle velocity $\overrightarrow{u}$ equals $\overrightarrow{u} = \sqrt{\overline{u}^2 + T}$, with the mean speed $\overline{u}$. So the local mean free path is larger than the the low density limits prediction. But the mean velocity in the vibro-fluidized granular gases media is zero, which is

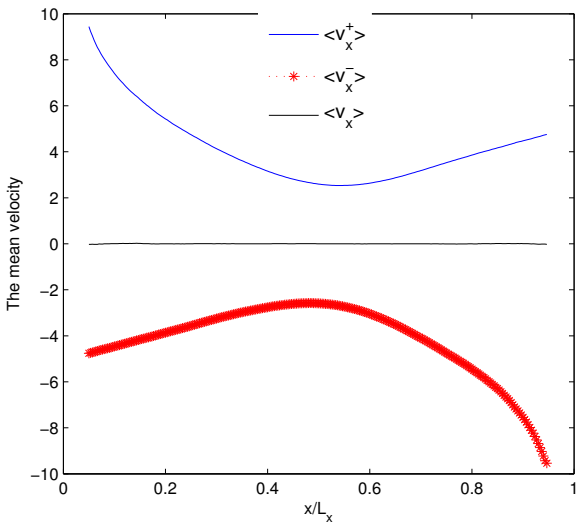

Figure 4.17: The spatial profiles of the mean velocity , v_x, v_x^+ and v_x^- ($L_x = L_y = 300$,$e = 0.9$,$N = 1000$,$V_{driven} = 10$).

also demonstrated in the works[12]. We also do not detect any significant nonzero local velocity field in our simulated system, which is illustrated in Fig. 4.17.

Even so, if we measure two mean velocities v_x^+ and v_x^- according to their velocity v_x sign, then we shall obtain $|v_x^+| \neq |v_x^-|$, also shown in Fig. 4.17. v_x^+ is supposed to equal the v_x^- under the steady state with zero velocity field everywhere for the classical hydrodynamic. It means there is the local velocity field even with the total mean velocity zero. We strongly believe that it is reasonable because this system is far from the equilibrium. So now, we can understand why the local mean free path is larger than the dilute prediction based on the molecular gas by understanding on the uniform shear granular system[133]. In the vibration granular system, though the mean velocity in vibration direction is zero, the mean velocity $< v_x^+ >$ and $< v_x^- >$ are not zero field. This is why the local free path profiles are much larger than the molecular gas prediction.

Moreover, we measure the local free path also depending their sign, l^+ and l^-. All the particles are separated according their moving direction v_y, then when the next collision happens, their free paths are collected, separately. l^+ and l^- are different with each other as shown in Fig. 4.18, beyond our expectations. The local free path of the l^+ and l^- all have a same lowest point in the box centre, as

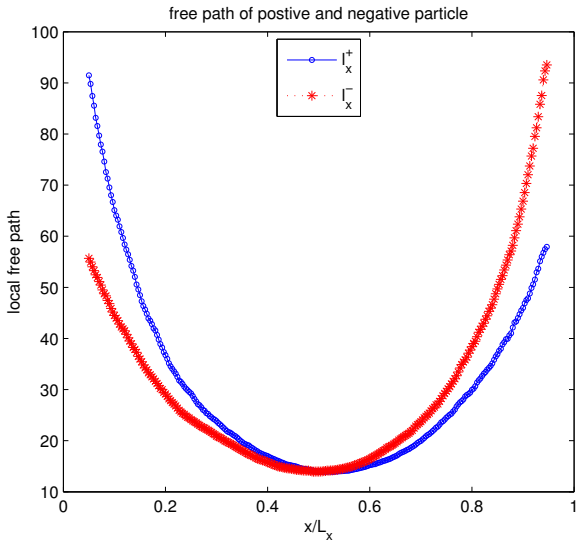

Figure 4.18: The spatial profiles of local free path l^+ and l^-.

it is the densest in the box center. The biggest gap between l^+ and l^- appears in the boundary layer, then reduces gradually till the box center point. These will bring many problems when treating the granular gases to the molecular gas approximately.

Fig. 4.19 provides the spatial profiles of the local free path under various box sizes. The box size varies from the $L_x = 600$ to the $L_x = 4200$, where the area fraction 0.0044 to 0.000623. The free path is found larger than the dilute gases theory prediction. For example, the maximum scaled mean free path of the condition $L_x = 4200$ is about 0.35 but not 0.13 predicted by the dilute gas theory. Furthermore, The gap between l^+ and l^- reduces but still exists when L_x increasing, as we expected. The boundary effect reduces when the system length increasing. Moreover, the free path seems to be linear on one side of the box.

4.7.3 Local Velocity Distribution

To explain above results, we need to conduct a detailed investigation about factors exerting influence over the free path. Let's recall the derivation of the mean free path. A particle moves in a irregular, zigzag path. Then a collision occurs whenever another particle center approaches the distance d from this particle

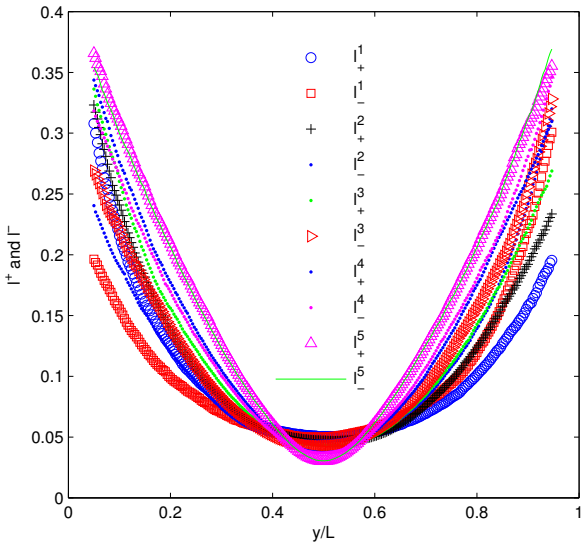

Figure 4.19: The spatial profiles of scaled free path l^+ and l^- under various box size. The note number ♯1 $L_x = 600$, ♯2 $L_x = 1200$, ♯3 $L_x = 1500$, ♯4 $L_x = 1800$, ♯5 $L_x = 4200$. All the free path are sealed by their L_x.($e = 0.9$,$N = 1000$,$V_{driven} = 5$,$L_y = 300$)

center. So the collision region will be a one cylinder swept out by this particle movement. In deriving the expression for the mean free path, four factors are involved, the diameter of the particle, the number density, the particle velocity, the relative velocity with other particles. To avoid supposing all the prior knowledge of the equilibrium, we need to study the local velocity distribution firstly.

We examine the local velocity distribution as the paper[13]. As mentioned above, we measure the local velocity distribution in each window which is moved from the left side of the box to the right side of the box. The three-dimension plot of the local velocity distributions are illustrated in Fig. 4.20. Our simulation results are consistent with the experiments in the papers[12, 13]and simulation results[12, 122]. Two peaks appear in the boundary layer, then melt to one peak when moving to the box center. The superposition of two Maxwellian distributions is supposed to describe this local velocity distribution in such system in [115]. To study Laws for the LVD Development, we use the Gaussian velocity distribution(Eq. 4.11) to fit the major peak of each LVD. It is difficult to obtain the suitable fitting results for the second peak which vanishes gradually. It is

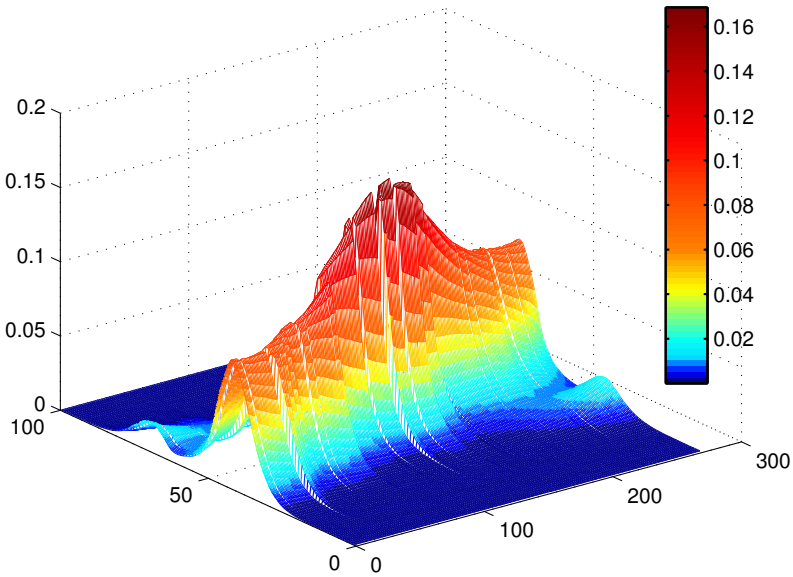

Figure 4.20: 3D probality disitrbution of the velocity.($L_x = L_y = 300$,$e = 0.9$,$N = 1000$,$V_{driven} = 10$).

convenient to study the major peak other than the second one. All the velocities are scaled by the v_{driven}.

$$f_m(v_y) = a \times exp[-(\frac{x-\xi}{\sqrt{2T_y}})^2] \tag{4.11}$$

Fig. 4.21, Fig. 4.22 and Fig. 4.23 show fitting results of the major peak by Eq.4.11 under various vibration velocity, when fixing the rest parameters. Fig. 4.21 gives the $\sqrt{T_y}$ profiles in Eq. 4.11. Excluded the marginal layer, the $\sqrt{T_y}$ values reduce from the boundary to the box center. This could be understood: the boundary heating rises the local temperature. With the dissipation of the inelastic collision, the temperature goes down moving far away from the boundary. Increasing the vibration velocity, $\sqrt{T_y}$ increases little. In Figs.4.22, α is the largest in the box center, reducing when leaving the center, since α is related to the local density which is sensitive to the vibration strength. Fig. 4.23 gives the fitting results of ξ, the expect value of the distribution under various vibration velocities. ξ increases gradually from left of the cell to the right. ξ of various v_{driven} overlap

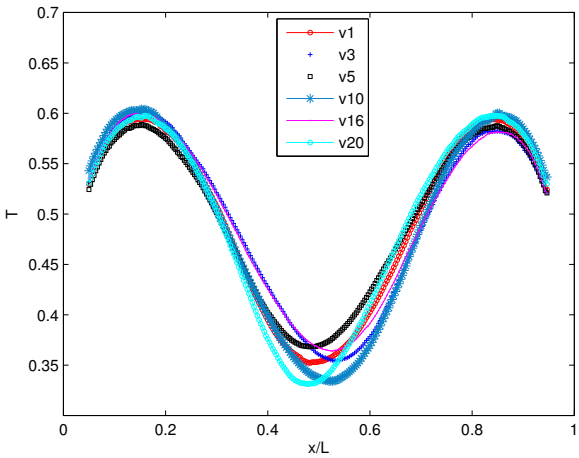

Figure 4.21: The spatial profiles of the fitting parameters $T_y(L_x = L_y = 300, e = 0.9, N = 1000, V_{driven} = 10)$.

with each other shown in the Fig. 4.23. It is surprising that the value ξ is almost the same with each in the various driven velocities. This means the mean of the major peak is not influenced by the boundary vibration.

Another thing needs to be mentioned here is that the difference between the Fig. 4.17 and Fig. 4.23. I need to emphasis the Fig. 4.23 shows the mean velocity of the major peak, while the Fig. 4.17 illustrates the mean value of v_x when the $v_x > 0$ or $v_x < 0$. General opinion starts to make out that the value of ξ should equal $< v_x^+ >$ or $< v_x^- >$. However, the region of integration between two variables is different. That is why the ξ passes the zero in the box center but not for $< v_x^+ >$ or $< v_x^- >$. The above result about Fig. 4.23 is reasonable. The major peak presents the particle free movements which is not directly heated by the driven velocity but other particle collisions, like the number of particles and the restitution coefficients. This result also proves that ξ depends on the particle nature, not on the boundary heating.

The skewness S of LVD is also shown in Fig. 4.24. S_x denotes the skewness of $f(v_x)$ as S_y for $f(v_y)$. S_x and S_y in various vibration conditions are almost overlapping. S_y are mostly near zero, while S_x appears varying from positive to negative. These profiles of S_x are almost the same under different driven velocities.

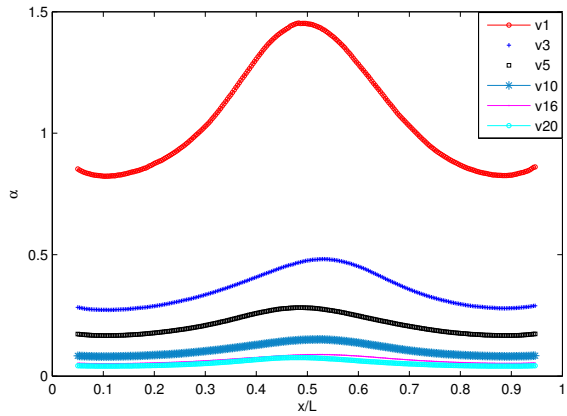

Figure 4.22: The spatial profiles of the fitting parameters a ($L_x = L_y = 300$,$e = 0.9$,$N = 1000$,$V_{driven} = 10$).

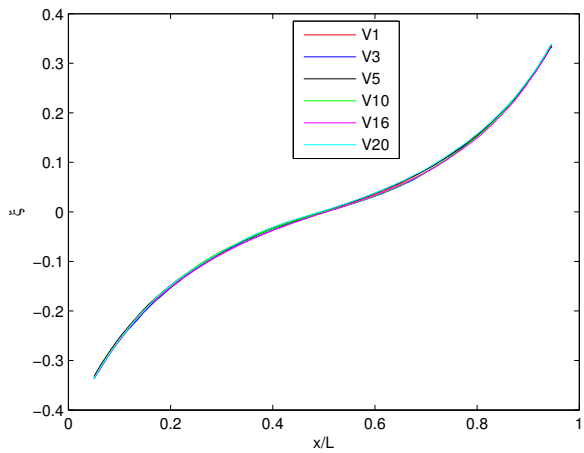

Figure 4.23: The spatial profiles of the fitting parameters ξ($L_x = L_y = 300$,$e = 0.9$,$N = 1000$,$V_{driven} = 10$).

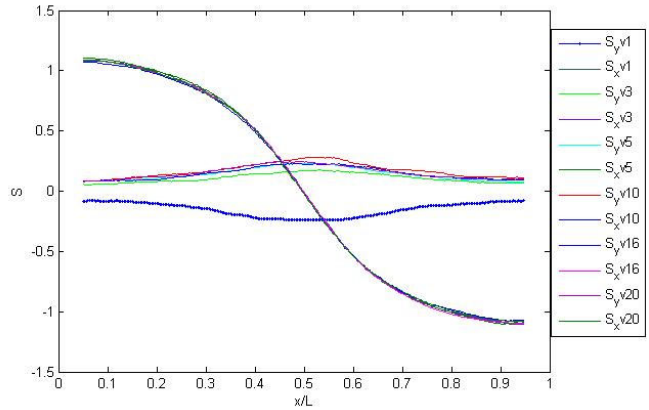

Figure 4.24: The spatial profiles of the fitting parameters S ($L_x = L_y = 300$,$e = 0.9$,$N = 1000$,$V_{driven} = 10$).

Fig. 4.21, Fig. 4.22, Fig. (4.23 and Fig. 4.24 gives a brief profile for the local velocity distribution in two dimensional granular gases. It demonstrates our assumption about the two peaks of the local velocity distributions. These results prove that the vibration only varies the number distribution but almost not change the value of the ξ or T_y. In the following, we will use the kinetic theory to give an analysis resolution for the local free path with the local velocity distributions.

4.7.4 The kinetic expression

In this part, we treat particles from two opposite directions in x axis to two species particles. Positive particle and negative particle are treated as two different type particles, and each is assumed to be Maxwellian distribution, separately. Then with the assumptions made for a vibrated granular gas discussed in [115], the colliding pairs of particles could be obtained analytically[69]. Each one has the Maxwellian distribution[137, 138]:

$$f_i(\mathbf{r}_i, v) = n_i(\frac{1}{2\pi t_i})exp[-\frac{(v-\xi_i)^2}{2t_i}] \tag{4.12}$$

where ξ_i denotes the mean velocity, t_i is the temperature, n_i is the number density. Each direction has its own temperature, the mean value and the number density.

To keep the mean velocity is zero, their parameters should satisfy:

$$n_1 + n_2 = n \tag{4.13}$$

$$n_1\xi_1 = -n_2\xi_2 \tag{4.14}$$

Where the note 1 and 2 represent the positive and negative components of v_x, n means the local number density. For the two dimensional situation here, $n = N/A$, N is the particle number, A is the area.

So the frequencies of the binary collisions can be expressed as

$$N_{ij} = \int\int\int f_{ij}^{(2)}(\mathbf{r}_i, \mathbf{v}_i, \mathbf{r}_j, \mathbf{v}_j) d_{ij} d\mathbf{k} d\mathbf{v}_i d\mathbf{v}_j \tag{4.15}$$

Here, i,j could be either direction (positive and negative direction in x axis). In order to simplify our discussion, molecular chaos assumption are used. So, the pair distribution, $f_{ij}^{(2)}$, could be written as,

$$f_{ij}^{(2)}(\mathbf{r}_i, \mathbf{v}_i, \mathbf{r}_j, \mathbf{v}_j) = f(\mathbf{r}_i, \mathbf{v}_i) f(\mathbf{r}_j, \mathbf{v}_j) \tag{4.16}$$

The pair distribution could be obtained by assuming chaos:

$$f_{ij}^{(2)}(\mathbf{r}_i, \mathbf{v}_i, \mathbf{r}_j, \mathbf{v}_j) = \frac{n_i n_j}{(2\pi)^2 t_i t_j} exp[-\frac{(v_i - \xi_i)^2}{2t_i} - \frac{(v_j - \xi_j)^2}{2t_j}] \tag{4.17}$$

where, i and j could be source-like or unlike particles, that is, the binary collisions could happen between particle with positive velocity and one with negative velocity, and positive one, positive one and negative one, and negative and negative one.

Firstly of all, the collision frequency:

$$N_{ik} = \int\int\int f_{ij}^{(2)}(\mathbf{r}_i, \mathbf{v}_i, \mathbf{r}_j, \mathbf{v}_j)(\mathbf{c}_{ji} \cdot \mathbf{k}) d^2 d\mathbf{k} d\mathbf{c}_i d\mathbf{c}_j \tag{4.18}$$

Let the relative velocity of the particle is

$$\mathbf{c}_{ji} = \mathbf{c}_j - \mathbf{c}_i \tag{4.19}$$

$$\mathbf{G}_{ji} = \frac{1}{2}(\mathbf{c}_j + \mathbf{c}_i) \tag{4.20}$$

$\mathbf{k}$ is the unit vector directed from the center of the first sphere to the second one during the collision. Considering the particle move is two dimension, so

$$\int \mathbf{c}_{ji} \cdot \mathbf{k} d\mathbf{k} = 2c_{ji} \tag{4.21}$$

where $\mathbf{c}_{ji} \cdot \mathbf{k} > 0$ is to make sure a collision will happen.

Using $\mathbf{v}_i$ and $\mathbf{v}_j$ substituted by $\mathbf{G}$ and $\mathbf{c}_{ji}$, frequencies of collision per unit time is expressed as

$$\begin{aligned} N_{ik} = \quad & \int\int \frac{n_i n_j 8 d_{ij} \pi^2}{(2\pi)^2 t_i t_j} \\ & \times exp[-\frac{(G + (1/2)c_{ji} - \xi_i)^2}{2t_i} - \frac{(G - (1/2)c_{ji} - \xi_j)^2}{2t_j}] \\ & \times c_{ji}^2 G dc_{ji} dG \end{aligned} \tag{4.22}$$

Then expanding it by Taylor series and ignoring all the high order terms, the solution of Eq. 4.22 is

$$N_{ik} = \frac{8 d_{ij} n_i n_j \sqrt{2\pi} (t_i t_j)^{3/2}}{(t_i + t_j)^{5/2}} e^{-\frac{1}{2}(\frac{\xi_i^2}{t_i} + \frac{\xi_j^2}{t_j})} \tag{4.23}$$

When $t_i = t_j$ and $\xi_i = \xi_j = 0$, the expression reduces to the molecular gases mixture in the[69] for two dimension gas. The mean speed of two dimensional Maxwellian gases is $\bar{v} = \sqrt{\frac{\pi k T}{2m}}$. Then we can calculate the mean free path for two components of the local free path basing on the Eq.4.23. The local mean free path for the positive direction is

$$l_1 = n_1 \overline{\mathbf{c}}_1 / (N_{11} + N_{12}) \tag{4.24}$$

where the subscript 1 denotes the positive component, while 2 represents the negative one. So the negative mean free path will be

$$l_2 = n_2 \overline{\mathbf{c}}_2 / (N_{22} + N_{12}) \tag{4.25}$$

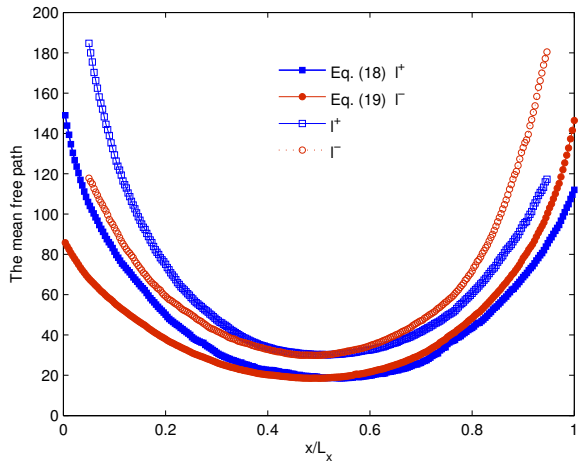

Figure 4.25: Parametric plots of Eq.4.24 l^+ (■) and Eq. (4.25) l^-(●), compared with the free path l^+ (□)and l^- (○) the simulation results with parameters $L_x = L_y = 600$,$e = 0.9$,$N = 1000$,$V_{driven} = 5$.

To compare our simulation results and the equation (4.23), the definitions of parameters are:

$$t_1 = \sum (v_x^+)^2 \tag{4.26}$$

$$\xi_1 =< v_x^+ > \tag{4.27}$$

Fig. 4.25 shows parametric plots of Eq. (4.24) and Eq. (4.25), compared with our simulation results. Our theory prediction works quite well with the simulation results. The trends of Eq. (4.24) and Eq. (4.25) are almost the same with simulation results. The qualitative value of our theory prediction is much larger than the dilute theory Eq.4.9. These demonstration Eq. (4.24) and Eq. (4.25) are effective representations of l^+ and l^- in the simulation. It means the free path are related with the local temperature and the number density with positive and negative components. Eq. (4.23) is much larger than the classical Grossman's Eq (4.9). It also describes the difference between the positive and negative free path feature which exists generally in the granular gases heated by the boundary.

In this section we investigate the local mean free path of granular gases, driven by vibrated walls. Each free path is obtained directly from particles tracking

in our simulation. We firstly compare our results of the dilute and near elastic situation, and the local free path is much larger than the classical molecular gases theory predicted which means that the local mean free path is underestimated for the vibrated granular gases. After increasing the length of the box in the vibration direction, we observe different local mean free path in various the area fraction. The spatial profiles of the local mean path become more and more linear with increasing the box length L_x. Moreover, the positive and negative components of the local mean free path is different with each other. The gap between the l^+ and l^- reduce when the L_x is elongated. Even the area fraction reduced to the 10^{-4}, the local mean free path is still larger than the classical theory prediction. By assuming the double Maxwellian velocity distribution, we obtain the local mean free analysis solution. Our theory agrees well with the simulation results.

4.8 Summary

In this Chapter, we have demonstrated, confirmed and discussed the asymmetry of the local velocity distribution in the vibrating direction using simulations. So, this is a real feature, which is also confirmed by simulation. Its variation with dissipation is demonstrated using different values of the restitution coefficient ($e < 1$) and different number of particles in the cell. Furthermore, we measured the skewness of the local velocity distribution as functions of the restitution coefficient ($0.999 < e_p < 0.65$) and of the number of particle (the area fraction $3.49 * 10^{-4} < \phi < 0.0126$). For the elastic system, the skewness is nearly uniform and $S = 0$ everywhere. For inelastic system, the skewness is non-zero except at the cell center. In the left side of the box, the skewness is positive and decreases (to 0) with the increase of the distance from the left boundary. In the right side of the box, the skewness is negative, and increases (to 0) with the distance to the right boundary. Skewness is 0 in the center of the cell due to the symmetry of the excitation we chose. The spatial profiles of the skewness (which is non zero most everywhere) indicates that this asymmetry is a bulk effect. Furthermore, we have shown that the value of skewness module increases when the restitution coefficient is decreased; this demonstrates this long range boundary effect is related to the system dissipation.

By using a simplified phenomenological model (superposition of two Gaussian functions), an expression of the skewness can be derived, which is consistent with our simulation data and consistent with our previous Airbus experimental results (see Chap 3), as soon as the modeling reaches a steady state. This confirms that boundary excitation and the dissipation property of the system lead to this long range boundary effect. The temperature evolution is also studied using the simulation. Study needs to define two different temperatures along x and y, and also two temperatures in $+y$ and $-y$.

The mean free path l^+ (of particles with $v_y > 0$) and l^- (of particles with $v_y < 0$) are different in the box, and varies in the opposite ways as a function of y.

Furthermore, one shall split the temperature problem in the y direction (vibration direction) to introduce two different temperatures T_y^+ and T_y^- . We calculate the two temperatures from the two components: the positive and negative temperatures. We find the energy equipartition does no longer persist in our simulation. Moreover, the ratio of two temperatures drops exponentially.

Finally, we discuss the heat flux and find the difference between a classical system and the granular system. These results imply that a new point of view is defined for exploring and explaining the properties of a granular system.

It is worth noting that we cannot explain the non Gaussian tail of the distribution of speeds, that remains to be understood clearly.

Chapter 5

The experiment results with the various gravity

In this Chapter, we consider the case of a vibrated-fluidized granular system in presence of various gravity field, such as an experiment reported by Kudrolli[54], where the granular gases are excited in an inclined plane. For the velocity component in the direction perpendicular to the motion of the oscillating wall, the distribution is found strongly non-Gaussian. For velocity component in the direction parallel to the vibrating wall, the distribution is even asymmetric. Moreover, This asymmetry becomes weaker if the tilting angle increases, and the velocity distribution becomes more Gaussian. This is due to the gravity which increases the ratio between the heating rate and the collision rate. And Baldassarri[62] simulated this experiment and get consistent results. If the force field increases to $100g$ (g is the acceleration of earth gravity), the velocity distribution becomes more Gaussian.

Brey et al. [139] investigated a similar system by simulation method and using an hydrodynamic description. The granular density profile exhibits a maximum. But the temperature profile exhibits a minimum at high altitude; this does not agree with the results in[140]. Further, in[141], the local velocity distribution are measured in a 1-or-2-layer system, and it was found that the shapes of the velocity distribution depend on the height of the layer (i.e. 1 or 2), on the coefficient of restitution and the measured location. This point implies that the local state of

a granular system is necessary to be investigated carefully, in the case of vertical vibration, too.

But, current studies of the local state of the granular system using experiment are scarce and they are connected mainly to data from the simulation. In this Chapter, we present our experimental results on 2D granular systems confined in an inclined 2-D cell and fluidized by vibration in the direction of the inclined cell. To study the variations of the different fields and distributions on gravity field, we changed the tilted angle from 0° to 85.5° by means of 5° step. It means we checked the dependence of granular system upon the parameters of vibration and upon the ball number from horizontal vibration to near vertical vibration at each step. Several hundreds of experimental data groups are obtained. The details of the experimental apparatus and the most important results can be found in this chapter; but other data are reported in Appendices C & D.

5.1 Experimental setup

The experiment are conducted in a quasi-2D rectangle cell (whose side walls were in aluminum, and front and back walls in glass, L_x, L_y, depth=$70mm * 50mm * 10mm$). The depth of the box is $10mm$ at largest (the width of side wall, Max($10mm$)), but is adjustable by using added glass widows to cover bottom to fit the ball diameter and to make sure the cell to be quasi-2D. The box is fixed on a vibrator(LDS). The vibrator is mounted on a rotary table (accuracy ,1 round=4°; and 240 grad/round). This table can circumrotate by 180° . The sketch of the experiment setup is shown in Fig. 5.1. There are two kinds of particles we used: one is made of bronze with diameter $d = 3mm$ and the other one is made of delrin with diameter $6mm$. In this thesis, due to space limitations, we only show the results of the bronze ball with $d = 3mm$. The movements of beads are recorded by a fast camera ($500fps$). Because image recording images are 2D, the particle rotation is not considered. An other thing to be noted is that one needs to rotate the camera to face the box windows, when rotating the angle of vibration. A 2D set of LEDs is mounted on the back side of the cell to increase the contrast between beads and the background. The box is divided into 15 layers along the vibration x direction (the size L_x is $70mm$). For inclined situation, particles

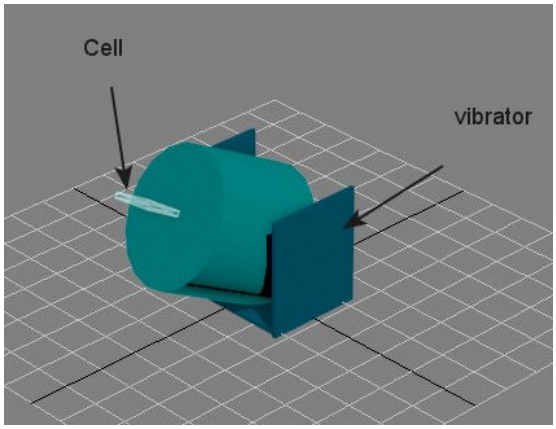

Figure 5.1: the experimental setup.

may not reach the top bins (depending on the vibrating parameters and on the inclination angle); for such bins, all the parameters are set to zero. Each group (for a single inclination) include 9000 frames.

The experiments in gravity field is more complex than those in micro-gravity. There are two reasons: A) Some friction exists between a particle and the bottom board of the cell, however, the friction between the bronze ball and the glass window is small. More, this friction can be ignored when the vibration intensity increases. B) there is a gravity field, so that each particle suffers gravity, which movement is parabola when it is free. The collisions are also influenced by gravity.

The images recorded by the fast camera are firstly processed to get the positions of bead centers, which are calculated through the ultimate eroded points(UEPs) in the Euclidian distance map(EDM). Afterwards, the particles are tracked by using the program of minimum-distance algorithm as described in Chapter. 3.

We did a series of experiments. Firstly, we tilted the angle and changed the inclination from near horizontal to near vertical each 5°. Then, the number of monolayer is changed per layer. So several hundred of groups of images are analyzed and processed.

The next sections of this chapter has the following structure. In Sec. 2.1 we present the experimental results in nearly horizontal vibration. Two cases are considered consecutively: in the first part of sub-section 5.2.1 vibration strength

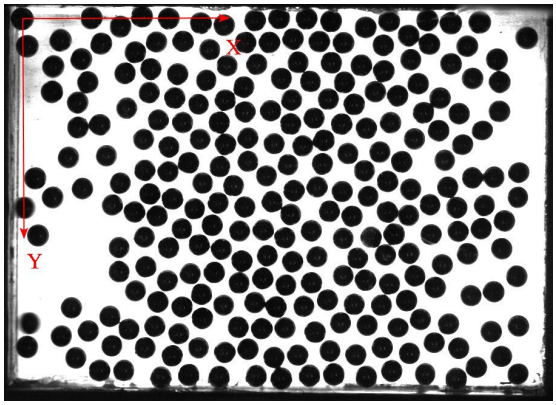

Figure 5.2: Snapshot of the cell and particles. The cell ($L_x * L_y = 70mm * 50mm$) contains 256 bronze sphere particles, driven in the x direction at various vibration parameters(A, V_ω, Γ, f).

is changed, which means comparing results in different parameters of vibration; in the second part of 5.2.1, the number of layers is then changed. In Sec. 2.2, we show results at various inclined angles. For brevity, we confine our attention on the velocity distribution and on the hydrodynamics profiles, although the other properties can be found if required. In section 5.3, dependence of the behaviors with gravity will be described.

5.2 Experiment results for slightly tilted vibration

In this section, we consider the properties of granular gases under a slight inclination (diameter $D = 3mm$, Bronze, tilt angle $q(\theta) < 1°$). Parts of the objective are to study the micro-gravity effect, and the slightly dependence about small-g effect; for instance, in parabolic flight, sometimes, the gravity is not equal to zero. Its gravity field fluctuates around zero. This experiment will study this kind of quasi-static micro-gravity effect. We are interested in two variational parameters: vibration parameters and the number of monolayer.

5.2.1 Various vibration intensity

Our experimental parameters are shown in Table.5.1. In this part of experiment the number of particles is kept constant $N = 256$, the number of monolayer is 16 and the area fraction $\phi = 0.52$. For such a system, the number density is quite large, so the system have to get energy from two boundary walls, and dissipate a lot through ball-ball collisions.

Table 5.1: The vibration parameters used in Fig. 5.3, Fig. 5.5 and Fig. 5.6.

Item	N	Freq(Hz)	Acc(m/s^2)	$V_\omega(m/s)$	Amp (mm)
1	256	50	70	0.22	0.14
2	256	50	80	0.25	0.16
3	256	50	90	0.29	0.18
4	256	50	100	0.31	0.20
5	256	50	110	0.35	0.22

5.2.1.1 The velocity distribution

Firstly, we take Item 5 data of Table 5.1 as an example to analyze the global and local velocity distributions $f(v_x)$ and $f(v_y)$, in log-linear scale. The global velocity distribution are displayed in Fig. 5.3. It is clearly that both velocity components are non-Gaussian. But the value of the exponent in the exponential law seems not clear. Here, x is the vibrational direction.

The local distributions of v_x and v_y are displayed in Fig. 5.4 and 5.5. Comparing these results with the experiment in micro-gravity and the simulation results, we do not see anymore the structure with two peaks in v_x; instead, we see a slight displacement of the peak towards positive velocities. There is no two-peak velocity distribution for $f(v_x)$ near the boundary layer. Instead, the center of $f(v_x)$ near the boundary layer is offset. Moreover, $f(v_x)$ bias goes to right in the left side of the box and bias goes to left in the right side of the box. Moving towards the center of the cell, the local distributions $f(v_x)$ become more symmetry and more Gaussian. This asymmetry around zero is consistent with the experiments in micro-gravity and simulation results. On the contrary, local distribution $f(v_y)$ looks symmetric everywhere in Fig. 5.5. Moreover, in Bin 1 and Bin 15 the shape

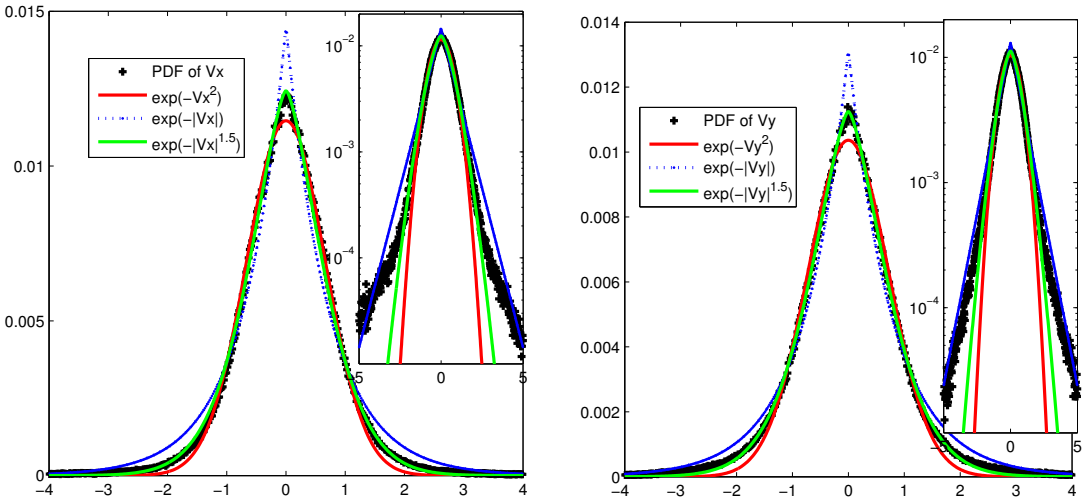

Figure 5.3: The global velocity distributions of the components v_x and v_y. Here, x is the vibration direction. v_x and v_y is scaled by their mean squared. The vibration parameters are listed in Item 5 in Table. 5.1).

of $f(v_y)$ is exponential, while in Bin 7, $f(v_y)$ become more Gaussian. It is obvious that the shapes of $f(v_x)$ and $f(v_y)$ are dependent on the position of the cell.

For various vibrational parameters function, we observe the skewness of the local $f(v_x)$ and $f(v_y)$ (shown in Fig. 5.6). It is also clear that skewness of $f(v_y)$ are 0 for y direction, while Skewness is positive on the negative v_x side and negative on the positive v_x side. Skewness passes through 0 at $v_x = 0$ linearly decreasing. It is clear $f(v_y)$ skewness remains near zero, while the profiles of the local $f(v_x)$ skewness is smaller when increasing the vibration parameters. One possible explanation for these findings is that: when increasing vibration strength, the dissipation increase, then the skewness of the local $f(v_x)$ become larger. This increasing dissipation leads the skewness larger; this has been demonstrated also in Chapter. 4. It is worth noting that the maximum of the skewness is not in the boundary layer as in microgravity result, but closer to the center of the box (see Fig. 5.6).

It is clear that the shape of the velocity distribution is affected by the vibration parameter. It seems that the stronger the vibration is, the skewer the local $f(v_x)$ is. Reasons for this looks obvious. Vibration velocity v_ω can decide energy a

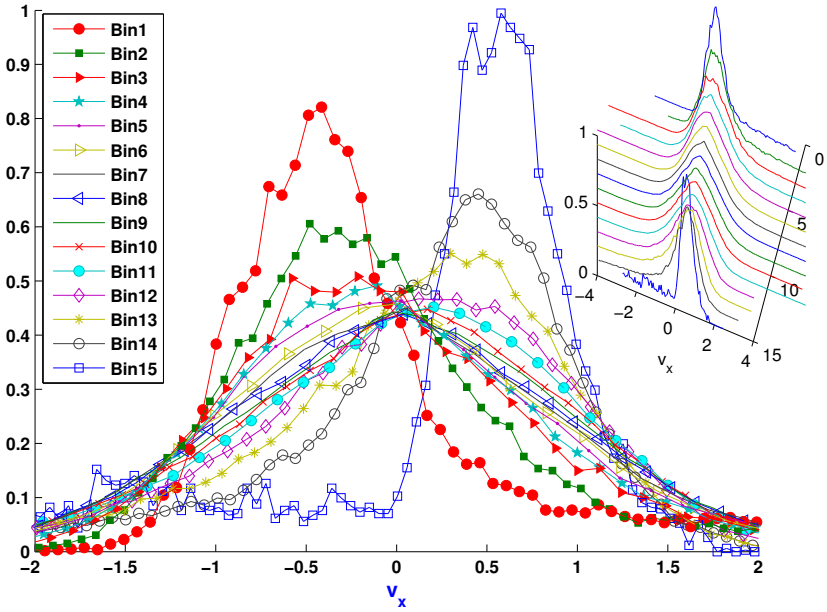

Figure 5.4: Local distribution $f(v_x)$ on log-linearscales of vibration parameters Item 5 (in Table. 5.1).

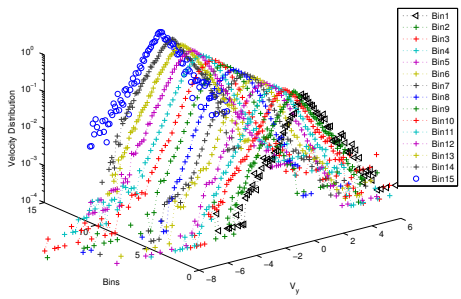

Figure 5.5: Local v_y distribution $f(v_y)$ on log-linear scales of vibration parameters Item 5 (in Table. 5.1).

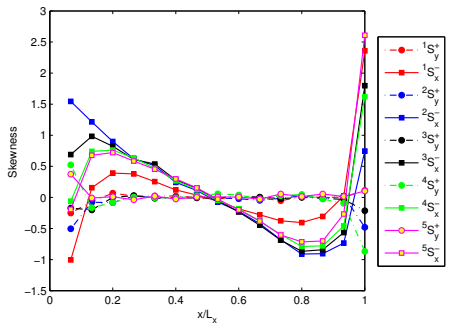

Figure 5.6: Skewness of $f(v_x)$ as function of vibration parameters in Table. 5.1.

Table 5.2: The vibration parameters used to display results with different number of particles.

Item	Freq(Hz)	Acc(m/s^2)	$V_\omega(m/s)$	Amp (mm)
1	60	134	0.36	0.18

particle obtained from the boundary wall. The larger the boundary effect is, the skewer the local velocity distribution $f(v_x)$ is.

5.2.1.2 The spatial profiles of Hydrodynamics

The number density profiles n_y^+& n_y^- are shown in Fig. 16 (bottom left) of Appendix C. It is found $n_x^\pm$ also are not equal, while $n_y^\pm$ are equal, whatever the vibration parameters. This point is consistent with our results in the micro-gravity and with those from simulation. In Fig. 16 (of the bottom right corner) of Appendix C, n_x^+ and n_x^- are rather symmetric like the results ahead. However, one sees the maximum of n_y^+ and n_y^- not to be on the center of the box, but slightly on the right side, the position of $n_x^+ = n_x^-$ are not in the center of the box. This is probably because our system is slightly tilted, leading to an effective small gravity. However, n seems not sensitive to the vibration parameter. So it needs to be studied in more details in future work.

The spatial profiles of the pressure and of the temperature at various vibration strength are shown in Fig. 16 of Appendix C. Top left of Fig. 16 shows $T_x^+ \neq T_x^-$ while Top right one displays $P_x^+ \neq P_x^-$. Such behaviors can also be found in our experimental results, which are consistent with these ones.

5.2.2 The number of layers

Let us describe the results obtained form a vibrated granular system, slightly tilted, containing various filling ratio. The number of layers is changed by step of 1 layer at a time; (1 layer=16 balls) till 16 layer (=256 balls) is achieved. Vibration parameters are not varied here but remains equal to those in Table. 5.2. Parts of results are listed in the Appendix C.

Firstly, we compare global velocity distributions $f(x)$ for various number of

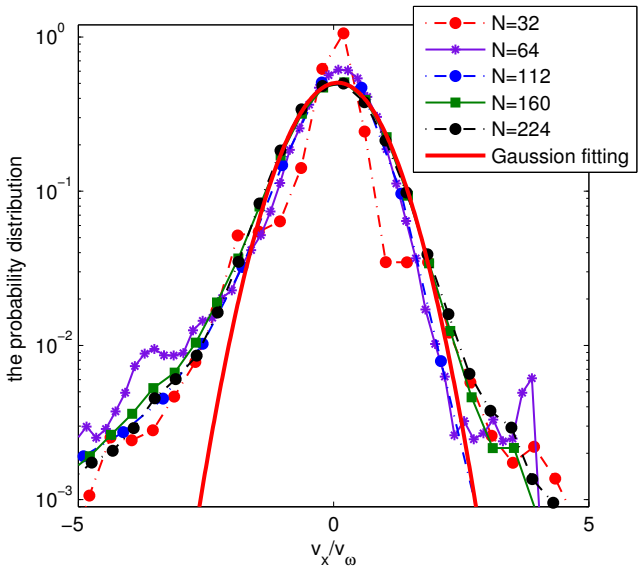

Figure 5.7: The Probability distribution $f(v_x)$ versus the number of particle. The solid line in red Gaussian fitting for $N = 160$. The vibration parameters are listed in the Table. 5.2.

monolayer in radius unit v_ω in Fig. 5.7. The differences between $f(v_x)$ does not appear after rescaling. All the distributions looks not Gaussian, a larger negative velocity tail. This is due to our cell which is slightly inclined. Secondly, in Fig. 19 of Appendix C, the hydrodynamics profiles are displayed.

As N increases, the system looks to become more and more inhomogeneous. For instance, the maximum of the number density looks to become larger than in Fig. 5.7. So, in order to investigate this point, we study the variation of this maximum; it is displayed in Fig. 5.8, where it looks increasing linearly in the present case.

5.2.3 The local equation of state

The work[12] presented the local equation of state for the simulation. We experimentally measure the local equation of state for our system[142] in this section. Local equation of state can be seen as a local constitutive equation of tempera-

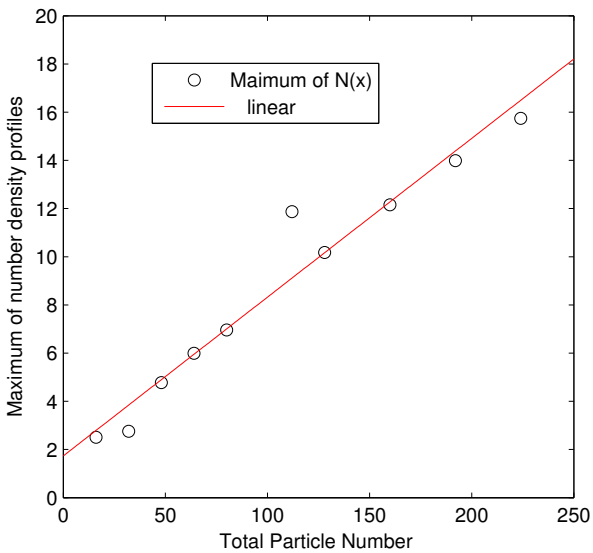

Figure 5.8: The maximum of the number density profiles versus total particle number N. The size of box is $70mm * 50mm$, the diameter of a particle is $3mm$. The particle change from one layer to 14 layers(16 particles per layer). The vibration parameters are listed in the Table. 5.2.

ture, pressure and the number density. The kinetic part is calculate by

$$\sigma_{ij}^{kin} = -m \int_{\Re} dv_x \int_{\Re} f_{stat}(\mathbf{r}, v_x, v_y) \times [v_i - U_i(r)][v_j - U_j(r)] \tag{5.1}$$

Except for the kinetic parts, the collision parts of the stress tensor are included. The detail calculation is Eq. 2.31 in the Chapter 2. Fig. 5.9 gives stress composed of the kinetic parts and the collision parts in our experiment. We could find that the stress σ_{xx}^{kin} and σ_{yy}^{kin} decrease moving from the boundary to the center, while the σ_{xx}^{int} and σ_{yy}^{int} increase. So the diagonal components of the stress tensor, σ_{xx} and σ_{yy}, are almost constant, which is consistent with the results from the simulation[12] and hydrodynamic theory.

Now, let us turn to the local equations of state predicted by theory[12] is:

$$\frac{p(x)}{\rho(x)T(x)} = G(\phi(x)) = 1 + (1+\alpha)\phi\chi \tag{5.2}$$

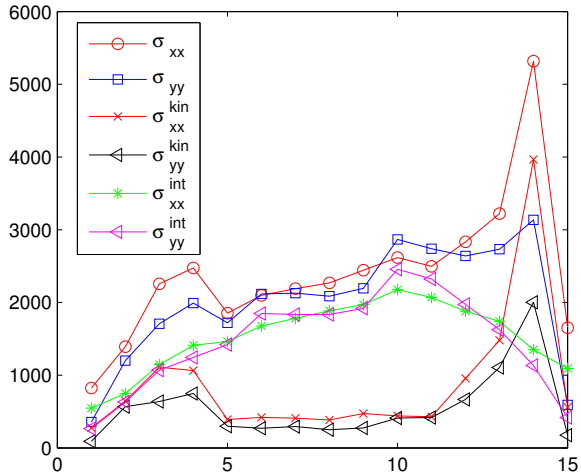

Figure 5.9: The spatial profiles of the stress versus total particle number N: σ_{xx}, σ_{yy},σ_{xx}^{kin}, σ_{yy}^{kin},σ_{xx}^{int}, σ_{yy}^{int}. The size of box is $70mm * 50mm$, the diameter of a particle is $3mm$, the number of particles is 256. The vibration parameters: the vibration frequencies $50Hz$, the acceleration $110m/s^2$.

where $\chi = \frac{1-7\phi/16}{(1-\phi)^2}$, ϕ is the are fraction, α is the restitution coefficient. Based on above stress tensor, we could calculated G in our experiments by $G = p(\phi)/nT(\phi)$. Fig. 5.10 compare 8 group experiment results G with various area fractions. The G is global underestimated by theory. It seems that when $\phi > 0.3$, the local equation seems agree well with the theory perdition. However, $\phi < 0.3$, the G are shown great difference between the experiment and simulation.

The possible reason maybe 1) The errors are introduced by tracking particles. 2) The above theory is based on the idea dense gas, but maybe not suitable for granular media. 3) The friction between particles and the box bottom is important factor. We also vary the value of α , but it has a little effect on the fitting results.

5.3 Experiments for various degree

In this section, we present experimental results as function of the inclination. The number of particles are varied at each angle. Some results are listed in the

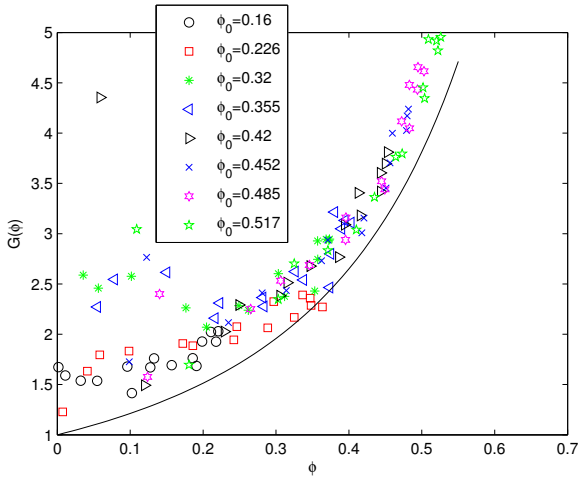

Figure 5.10: The semi-logarithmic plots the $G(\phi)$ under various area fractions. The solid line is calculated by Eq. 5.2. we suppose $\alpha = 0.8$. The size of box is $70mm * 50mm$, the diameter of a particle is $3mm$, the number of particles is from 80 to 256. The vibration parameters: the vibration frequencies $60Hz$, the acceleration $130m/s^2$.

Appendix D. Here, we only give the trends and the most important results. It is obvious that each particle is now subject to a gravitation effect $g_e = gsin\theta$ pointing downward, where θ is the inclined angle.

5.3.1 The velocity distribution

We first start with the velocity distributions. Here, we display the global velocity distribution $f(v_x)$ and $f(v_y)$ at various degrees. $f(v_y)$ is still symmetric, but $f(v_x)$ is asymmetric from 5.5° to 85.5° (shown in Fig. 5.11). This results are consistent with the experiment results in [58]; it does not show up strong dependence with angle of gravity.

The velocity distribution perpendicular to the vibration direction can be fitted by an $f(v_y) = Ae^{-B|v_y|^{-1.5}}$; it means that the velocity distributions along v_y is are still non-Gaussian even when gravity is increased.

Fig. 5.12 display the $f(v_x)$ distribution, for different gravity field. All the distributions look asymmetric and quite similar in the top, while they may diverge in the far tails. The the velocity probability distribution turn to be never Gaussian

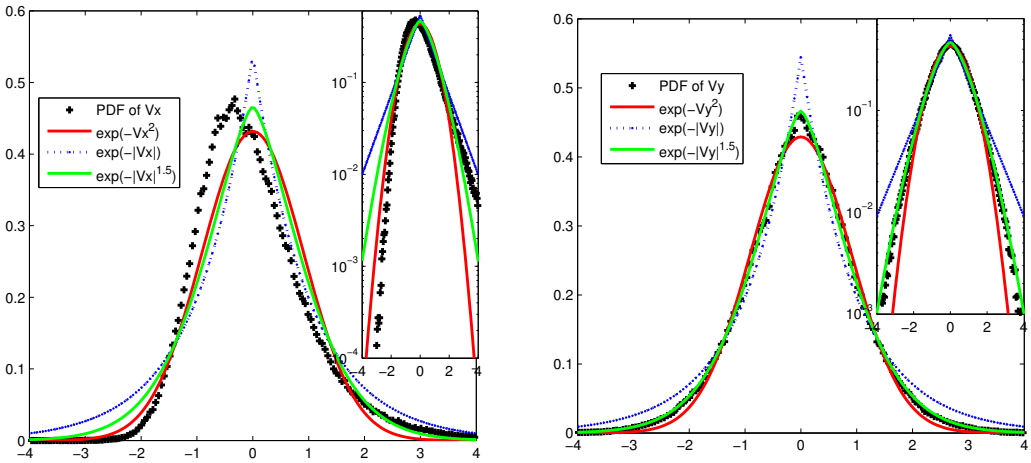

Figure 5.11: The global velocity distributions of different components v_x and v_y. Here, x is the vibration direction. v_x and v_y are scaled by their mean squared. The vibration parameters are listed in Table 22). Degree is 30°.

and seems reach a steady shape, merely independent of the angle as soon as the angle of inclination are raised up above 5.5°. This means that most of the asymmetry happens below $0.1g$ within our vibration parameter. This is different from experiments in [54, 62]. They assumed this is a effect of the increase of the heating rate. However, our results show that the heating rate reaches a steady value even if the inclined angle increasing continuously. Another explanation might be that the heating rate has already reached its maximum and can not be able to increase continuously.

Results for the local velocity distributions are displayed in Appendix D at various inclinations. Here we describe a single example: the one corresponding to Fig. 35 and 36, obtained at 35.5°. The $f(v_y)$ in each bin is displayed in Fig. 35 in Appendix C, which shows a symmetric distribution in each bin. But the $f(v_x)$ in Fig. 36, display different shape, depending on the bins, and the nearer the bins from the boundary, the more asymmetric the distribution as usual. The more central the bin the more regular the shape of $f(v_x)$. This situation always exists, i.e. whatever the inclination. It is clear the boundary plays a part in the asymmetry of the distribution, and hence plays also a part in the non Gaussian shape.

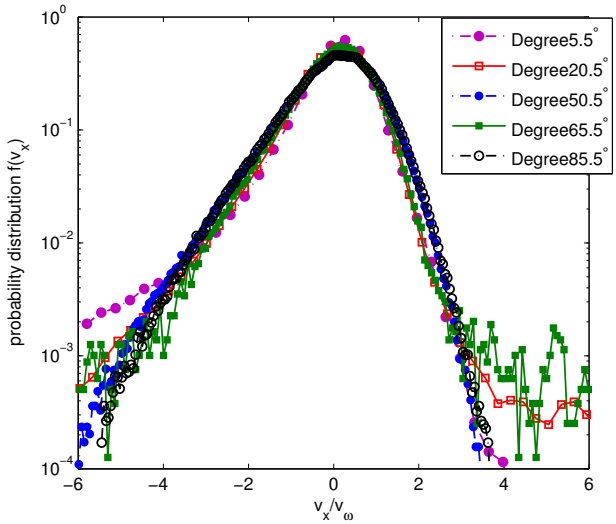

Figure 5.12: The probability distribution $f(v_x)$ versus the tilted angle. x is the vibration direction.

5.3.2 Spatial profiles of the number density $n^{\pm}_{x,y}$

We turn now to the study of mean ball numbers n^+_x, n^-_x, n^+_y, n^-_y at different inclinations; this is sketched in Fig. 5.13. One observes, (i) the larger the distribution the smaller the inclination, at least for 5.5° and n^+_x is larger than n^-_x. While n^+_y and n^-_y are of same order for the same inclination. So, $n^+_y = n^-_y$ and $n^+_x \neq n^-_x$ exists in various tilted degrees; furthermore, one can tell also that $n^+_y + n^-_y = n^+_x + n^-_x$. However this relation is not precise. From these figures we can tell that starting from level 0, the number of grains first increases, passes through a maximum, then decreases. The mean height (where $n = 4 \sim 6$ is always about the same except for 5.5° inclination, the height of which is slightly larger ($y/L = 0.5$ or 0.6, while the other are 0.4). The lower the maximum of density the large the gravity (or the inclination); this looks also quite normal, since the heap is dense by gravity.

For a molecular gas, the number density of in the atmosphere is scaling as

$$n = n_0 e^{-\frac{mgh}{kT}} \tag{5.3}$$

Indeed, our experimental results demonstrate the spatial profiles of granular gases

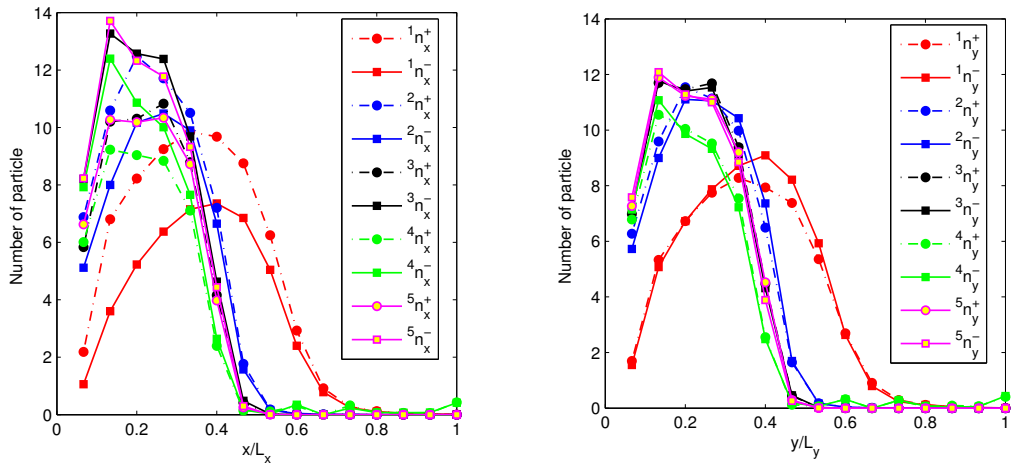

Figure 5.13: Spatial profiles of the number particles $n_x^{\pm}$ and $n_y^{\pm}$. Here, x is the vibration direction. The vibration parameter is listed in Table. D.22), Label #1 corresponds to 5.5° inclination, #2 to 20.5°, #3 to 50.5°, #4 to 65.5° , and #5 to 85.5°.The number of particles is 112 and the area fraction is 0.23.

are not exponential forms. Furthermore, n_x^+ is not equal to n_x^-. This demonstrates that vibration-fluidized granular gases are a dynamics process and total different from the classical situation.

To keep the momentum conservation, it can be deduced that the $\bar{v_x^+} \neq \bar{v_x^-}$. In different inclined angle, mean of velocity components $\bar{v_x^+}$ and $\bar{v_x^-}$ are shown in Fig. 5.14. For the degree 5.5°, the mean velocity is similar with our molecular simulation in the previous chapter. When the degree increase to 35.5° , the spatial profiles of the mean velocity change a lot. Even the spatial profiles ofv_x^+ and v_x^- are no long axis symmetric, but influenced by gravity.

Theories about the vibrational granular gases under gravity include(a) hydrodynamic model[62]. (b) statistics model[58]. However, these model often take the assumptions based on the classical thermodynamics and hydrodynamics. From our above experiments, due to great dissipation, the deviation with the theory is not surprising.

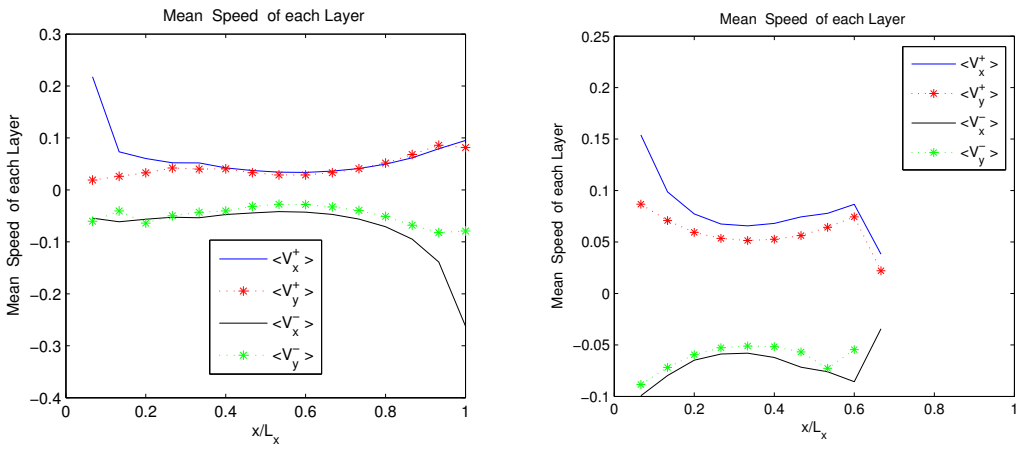

Figure 5.14: The spatial profiles of the mean velocity $v_x^{\pm}$ and $v_y^{\pm}$. Here, x is the vibration direction. The vibration parameters are listed in Table. 22). (Left)5.5°. (right) 35.5°

5.4 The Hydrodynamic model

In presence of a uniform external force $\mathbf{f}$, for a dilute granular gas[139], the hydrodynamic equations are:

$$\frac{\partial n}{\partial t} + \vec{\nabla} \cdot (n\vec{u}) = 0 \tag{5.4}$$

$$\frac{\partial u_i}{\partial t} + \mathbf{u} \cdot \nabla u_i + (nm)^{-1} \nabla_i p - (nm)^{-1} \nabla_j \times [\eta(\nabla_i u_j + \nabla_j u_i - \frac{2}{d}\delta_{ij}\vec{\nabla} \cdot \vec{u})] - m^{-1} f_i = 0 \tag{5.5}$$

$$\frac{\partial T}{\partial t} + 2(dnk_B)^{-1} P \nabla_i u_j \times [\eta(\nabla_i u_j + \nabla_j u_i) - \frac{2}{d}\delta_{ij}\nabla \cdot \vec{u})] - 2(dnk_B)^{-1} \nabla \cdot (\kappa \nabla T + \mu \nabla n) + T\xi^{(0)} = 0 \tag{5.6}$$

$$\mathbf{f} = -mg\hat{\mathbf{e}}_z \tag{5.7}$$

Here, $n(\vec{r}, t)$ is the local number density field , $\vec{u}(\vec{r}, t)$ is local average velocity field, or local flow velocity, $T(\vec{r}, t)$ is the temperature field, $\hat{\mathbf{P}}(\vec{r}, t)$ is the pressure tensor, m is the mass, $\zeta(\vec{r}, t)$ is the cooling coefficient, k_B is the Boltzmann constant, μ is the granular transport efficient, η is the shear viscosity, κ is the heat transport

efficient. Their expressions are as follows:

$$\eta = \eta^*(\alpha)\eta_0(T) = \eta^*(\alpha)\frac{2+d}{8}\Gamma(d/2)\pi^{-(d-1)/2}(mk_BT)^{1/2}\sigma^{-(d-1)} \tag{5.8}$$

$$\eta^*(\alpha) = [\nu_1^* - \frac{\zeta^*(\alpha)}{2}]^{-1} \tag{5.9}$$

$$\kappa = \kappa^*(\alpha)\eta_0(T) = \kappa^*(\alpha)\frac{d(2+d)^2}{16(d-1)}\Gamma(d/2)\pi^{-(d-1)/2}(\frac{k_BT}{2})^{1/2}\sigma^{-(d-1)} \tag{5.10}$$

$$\kappa^*(\alpha) = [\nu_2^* - \frac{2d\zeta^*(\alpha)}{d-1}]^{-1}[1+c^*(\alpha)] \tag{5.11}$$

$$\mu = \mu^*(\alpha)\mu_0(T) \tag{5.12}$$

$$\mu^*(\alpha) = 2\zeta^*(\alpha)[\kappa^*(\alpha) + \frac{(d-1)c^*(\alpha)}{2d\zeta^*(\alpha)}] \times [\frac{2(d-1)}{d}\nu_2^*(\alpha) - 3\zeta^*(\alpha)]^{-1} \tag{5.13}$$

$$\zeta^{(0)} = \zeta^*(\alpha)\frac{p}{\zeta_0} \tag{5.14}$$

$$\zeta^*(\alpha) = \frac{2+d}{4d}(1-\alpha^2)[1+\frac{3}{32}c^*(\alpha)] \tag{5.15}$$

$$\nu_1^*(\alpha) = \frac{(3-3\alpha+2d)(1+\alpha)}{4d}[1-\frac{1}{64}c^*(\alpha)] \tag{5.16}$$

$$\nu_2^*(\alpha) = \frac{1+\alpha}{d-1}[\frac{d-1}{2} + \frac{3(d+8)(1+\alpha)}{16} + \frac{4+5d-3(4-d)\alpha}{1024}c^*(\alpha)] \tag{5.17}$$

$$c^*(\alpha) = \frac{32(1-\alpha)(1-2\alpha^(2))}{9+24d+(8d-41)\alpha+30\alpha^2(1-\alpha)} \tag{5.18}$$

For the steady state, the above equations reduce to:

$$\frac{\partial p}{\partial z} = -nmg \tag{5.19}$$

$$\frac{2}{dnk_B}\frac{\partial}{\partial z}(\kappa\frac{\partial T}{\partial z}+\mu\frac{\partial n}{\partial z})-T\zeta^{(0)}=0 \tag{5.20}$$

By introducing the local mean free path scale l:

$$l=\int_z^L dz'\frac{1}{\lambda(z')} \tag{5.21}$$

Then detail derivation could be found in the work[139]. The general solution of the temperature will be :

$$T^{1/2}(\xi)=A\xi^{-\nu}I_\nu(\xi)+B\xi^{-\nu}K_\nu(\xi) \tag{5.22}$$

$$\nu(\alpha)=\frac{\mu^*(\alpha)}{4[\kappa^*(\alpha)-\mu^*(\alpha)]}>0 \tag{5.23}$$

I_ν and K_ν are modified Bessel functions of the first and second kind.

$$p(\xi)=\frac{mg\xi}{C\sigma^{d-1}\sqrt{a(\alpha)}} \tag{5.24}$$

$$\frac{d\xi}{n(\xi)}=-\sqrt{a(\alpha)}C\sigma^{d-1}dz \tag{5.25}$$

Our system is not an open vibrated system, it is difficult to obtain the solution of Eq. 5.20 appropriately. Though our experimental box is closed, the particles do not collide on the other wall when the inclination is small. So we could compare our large inclination results with the simulations in the above open vibrated system (Our experiment results could be found in the Appendix D). Comparing with above simulation and theory, we could conclude the follow points in our experiments:

(i) The trends of the number density profiles in the experiments are similar with simulation. The number density have a maximum at $\xi=\xi_n$. The height of the location ξ_n increases with the inclination degree growing up, which is shown in the Fig. 5.13. However, the height of the location ξ_n does not seems to be sensitive with the vibration strength, which is almost the same under various vibration strengths shown in the Fig. 25. This Figure also demonstrates that the value of the maximum of number density is increase with vibration strength when the inclination degree is small. When we increasing the inclination, we could find

the maximum of the number density varies not only the value but also the height in the box.

(ii) Besides similar points above, we also find that two components of the number density according to the vibration direction, n_x^+ and n_x^-. They are different with each other but the number densities n_y^+ and n_y^+ overlap with each other. All these findings are consistent with our previous results.

(iii) The overall trend of the granular temperature is also similar with the open system, where the temperature could be described approximately by :

$$T^{1/2}(\xi) \simeq A\xi^{-\nu} I_\nu(\xi) - B\xi^{-\nu} ln\xi \tag{5.26}$$

The maximum of the granular temperature also appears in the low altitude, which is consistent with the simulation in[139]. With the inclination degree increasing, the scaled temperature becomes smaller and smaller. The gap between the T_x^+ and T_x^- reach its maximum in the box bottom (near the vibrator), then slowly narrows toward the box center.

(iv)The pressure could be directly expressed by the Eq. 5.24. With the effective gravity increasing(the inclination degree increasing), the scaled pressure gradually increases, which is shown in the Fig. 24 to 52.

5.5 Summary

The objective of this work is to study the steady state of a vibrated granular gas in various gravity. It has been shown the following major results: (i) For the horizontal vibration, the global velocity distributions $f(v_x)$ and $f(v_y)$ are exponential fitted with the coefficient 1.5. Here, the vibration direction is x axis. $f(v_x)$ is asymmetric which is consistent with our experiment in micro-gravity or simulation in previous chapters. However, there are no two peaks appearing in the boundary layer for $f(v_x)$ like the results in micro-gravity, replacing by the peak overall shift. Comparing with the results in micro-gravity, the bottom friction maybe the important factor. (ii) The skewness of $f(v_x)$ is strongly affected by the vibration strength. The skewness becomes larger with increasing vibration strength. (iii) there exists a maximum for the number density along x axis. Height

corresponding the maximum point is increasing with the inclination degree. n_x^+ and n_x^- are different with each other, more, $n_x^+ > n_x^-$. It means the number of upward particle is larger than the down wards flows. The biggest gap between n_x^+ and n_x^- appear in the height corresponding the maximum point. (iv) The positive and negative components of the temperature, pressure and the number density in x direction are also show difference in presentation of gravity.

Chapter 6

Conclusions

In this thesis, we have explored the physical properties of dissipative granular gases in steady state driven by vibrating boundaries. The great research progresses are obtained in the granular physics in the last score years. The classical molecular gas theories and hydrodynamics was applied to describe the granular gases. Plenty of agreements between the classical theory and the granular media are obtained. However, a growing body of research is raising questions whether the classical theories can run efficiently on the physics of granular gases. Most focus on questions,take a example, the local equilibrium exists or not, Breakdown of molecular chaos and boundary layers. In particular, the boundary condition is one more difficult and open subject of investigation in the granular physics[143]. In this thesis, we are considering the boundary effect on vibrated granular gases.

The boundary condition is crucial because of the granular dissipation. The dissipation characters the granular media. To maintain a steady state, the energy is injected continuously to balance the energy loss. In the most experiment cases, energy usually is injected from the boundary. However, the theory usually omit the boundary effect. Is that reasonable or not? We need to find the answer.

In this thesis, we focus on the vibrated granular gas in a steady state. Three study methods are adopted in this thesis: micro-gravity experiments, event-driven molecular dynamic simulations and the experiments in various gravity. Remarkably, this work introduces a new innovative view to observe granular gases by employing local measurement of speed and density at different directions. This allows to show that local velocity distributions deviate measurably from a sym-

metric distribution for the velocity component in the vibrating direction. By separating statistics on positive and negative components of velocity at each point of the cell, we could demonstrate a long range effect which is generated by the vibrating boundary. The energy equipartition is found to break down in 2D boundary driven granular gases, in all directions and in different ways. We also find the mean free path and energy sink are anisotropic, and the mean free path is much larger than the classical gas theory prediction. By using simulation, we found this effect to be related to the system dissipation, since the asymmetry is getting larger when this dissipation increases, i.e. either diminishing the restitution coefficient e ($e < 1$) or increasing the particle number N. On the contrary, no speed asymmetry is found in the elastic case, i.e. when using $e = 1$ for the restitution coefficient, there is no such effect.

We propose a superposition of two Gaussian distributions to describe the local velocity distributions for the velocity component in the vibrating direction. The results of the experiment and the simulation show a good agreement. Furthermore, Double-Gaussian model are also used to calculate the mean free path, the results is closer to the true mean free path. We argue that this model is simple but can be captured the nature of the vibrated granular gas, which is strongly affected by two boundary wall.

We extend these results to vibrating geometries such as those with inclined planes and cells, that mimic various gravity field, where we find asymmetry of speeds, but with some modification about the local densities and speeds, especially on the upper part of the heap, when the heap is not efficiently excited. This result brings an additional piece of evidence that the problem we are facing couples gravity and boundary effects.

These results allow shedding light on the reason why the classical theories can not describe effectively on granular gases. It is clear now that the local equilibrium does not exist in granular gases. Future work will focus on theoretical development combining experiment and simulation results to understand the real unique nature of granular gases, which looks quite unique and strange at this research stage.

Appendix A: Airbus data

This Appendix A presents the Airbus experimental results of granular gases in Chapter2. All the experiment parameter are list in the Table. 3.1.

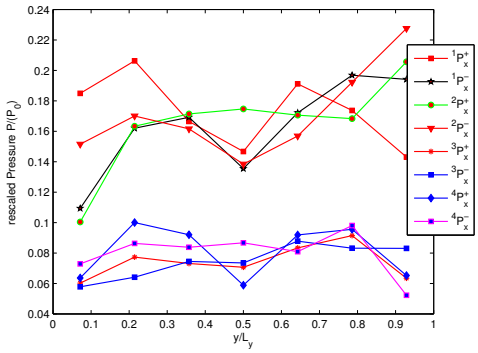

Figure 1: Experimental results of scaled pressure $p_x^{\pm}$ profiles in y direction, $N = 47$, and vibration parameters labelled Item 1 $\sim$ 4 in Table. 3.1).

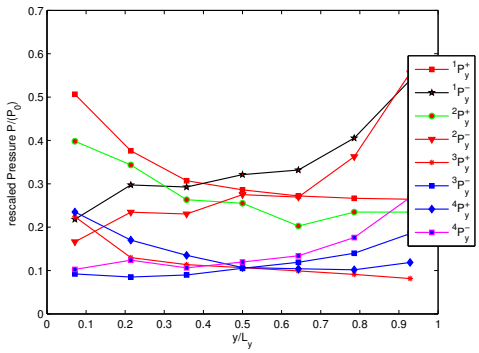

Figure 2: Experimental results of scaled pressure $p_y^{\pm}$ profiles in y direction, $N = 47$, and vibration parameters labelled Item 1 $\sim$ 4 in Table. 3.1).

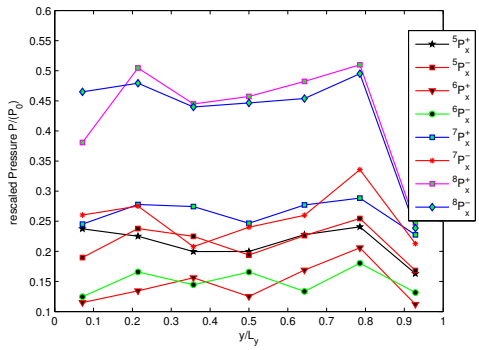

Figure 3: Experimental results of scaled pressure $p_x^{\pm}$ profiles in y direction, $N = 47$, and vibration parameters labelled Item $5 \sim 6$ in Table. 3.1).

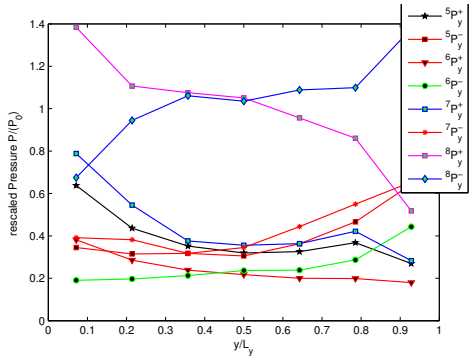

Figure 4: Experimental results of scaled pressure $p_y^{\pm}$ profiles in y direction, $N = 47$, and vibration parameters labelled Item $5 \sim 6$ in Table. 3.1).

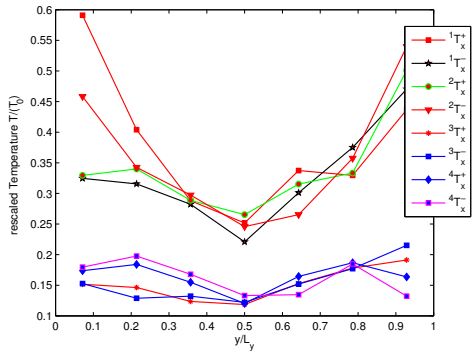

Figure 5: Experimental results of scaled temperature $T_x^{\pm}$ profiles in y direction, $N = 47$, and vibration parameters labelled Item $1 \sim 4$ in Table. 3.1).

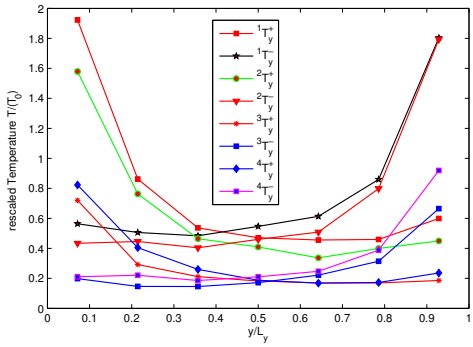

Figure 6: Experimental results of scaled temperature $T_y^{\pm}$ profiles in y direction, $N = 47$, and vibration parameters labelled Item $1 \sim 4$ in Table. 3.1).

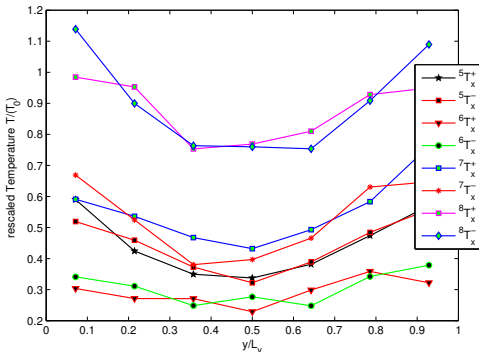

Figure 7: Experimental results of scaled temperature $T_x^{\pm}$ profiles in y direction, $N = 47$, and vibration parameters labelled Item $5 \sim 6$ in Table. 3.1).

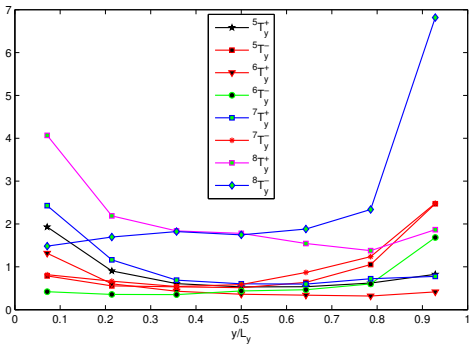

Figure 8: Experimental results of scaled temperature $T_y^{\pm}$ profiles in y direction, $N = 47$, and vibration parameters labelled Item $5 \sim 6$ in Table. 3.1).

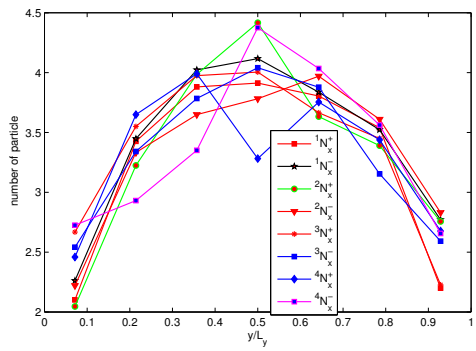

Figure 9: Experimental results of number of particle $N_x^{\pm}$ profiles in y direction, $N = 47$, and vibration parameters labelled Item $1 \sim 4$ in Table. 3.1).

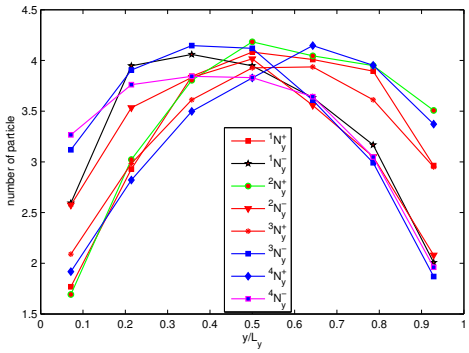

Figure 10: Experimental results of number of particle $N_y^{\pm}$ profiles in y direction, $N = 47$, and vibration parameters labelled Item $1 \sim 4$ in Table. 3.1).

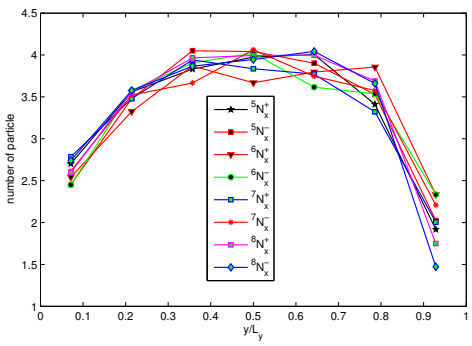

Figure 11: Experimental results of number of particle $N_x^{\pm}$ profiles in y direction, $N = 47$, and vibration parameters labelled Item $5 \sim 6$ in Table. 3.1).

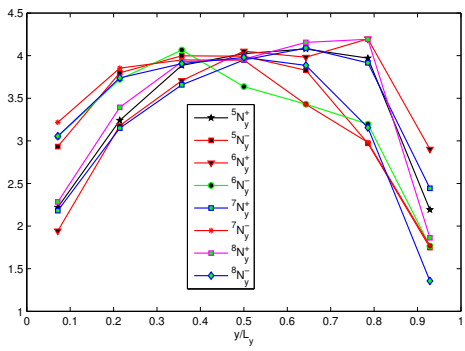

Figure 12: Experimental results of number of particle $N_y^{\pm}$ profiles in y direction, $N = 47$, and vibration parameters labelled Item $5 \sim 6$ in Table. 3.1).

Appendix B: simulation Results

This Appendix B presents The simulation results for various coefficient of restitution.

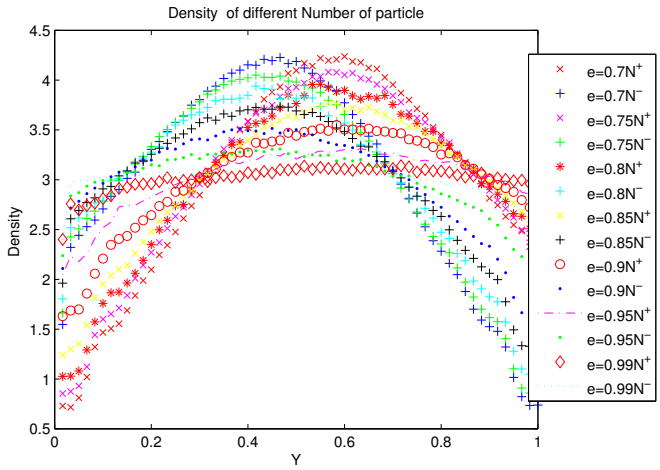

Figure 13: The number of particle $N_y^{\pm}$ for various coefficient of restitution. The particle radius r is set to be 1. The size of the cell is $(300r \times 300r\ )$. The number N of particles is $N = 360$, the area fraction is $\phi = 0.0126$.

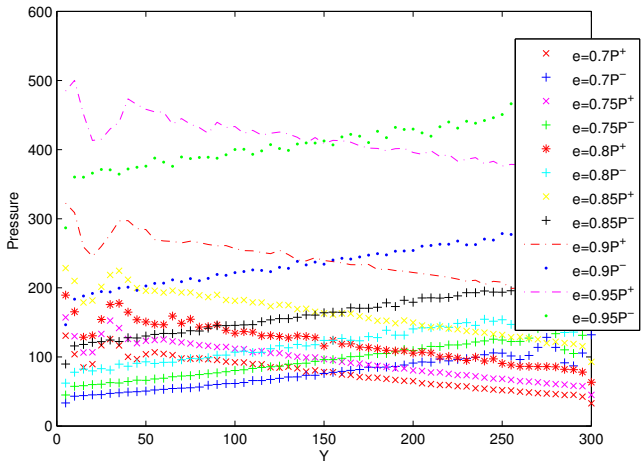

Figure 14: The pressure $p_y^{\pm}$ for various coefficient of restitution. The particle radius r is set to be 1. The size of the cell is $(300r \times 300r\ )$. The number N of particles is $N = 360$, the area fraction is $\phi = 0.0126$.

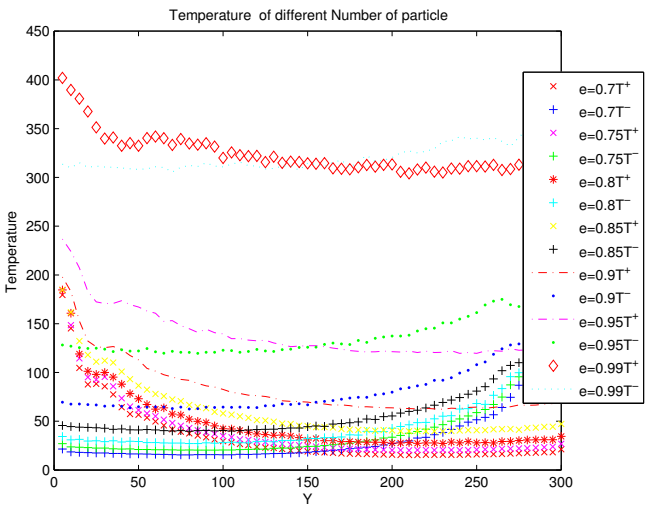

Figure 15: The pressure $T_y^{\pm}$ for various coefficient of restitution. The particle radius r is set to be 1. The size of the cell is $(300r \times 300r\ )$. The number N of particles is $N = 360$, the area fraction is $\phi = 0.0126$.

Appendix C: experimental results on slightly tilted 2D cell

This Appendix C presents the experimental results of 2D granular gases excited in a slightly tilted plane($< 2°$) with incilined vibration. The details experimental setup and method can be found in Chapter. 5. By adjusting the vibration parameter and number of particles, we investigated the local state of granular gases. There are two parts in this appendix: the first one is the results of local state as a function of vibration parameters for each st (item); the second one is the results of local state as a function of the number N of particles.

A-1) Local state as a function of vibration parameters for $Angle = 2°$

Table 1: The vibration parameters are displayed in fig.20, 21 and 16.

Item	N	Freq(Hz)	Acc(m/s^2)	$V_\omega(m/s)$	Amp (mm)
1	256	50	70	0.22	0.14
2	256	50	80	0.25	0.16
3	256	50	90	0.29	0.18
4	256	50	100	0.31	0.20
5	256	50	110	0.35	0.22

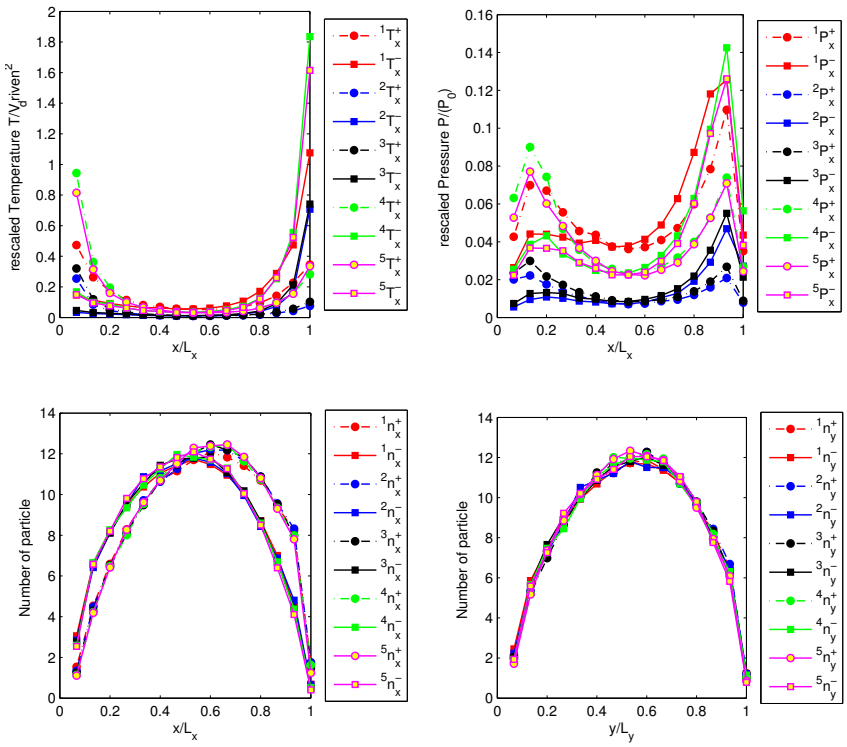

Figure 16: (upper left) The scaled temperature T_x^{pm} with velocity $v_x^{\pm}$.. (upper right) Pressure. (low left) Number of particle with $v_x^{\pm}$. (low right) Number of particle with $v_y^{\pm}$. Parameters are in Table. 1.

Table 2: The vibration parameters are displayed in fig.17, 18 and 19.

Item	N	Freq(Hz)	Acc(m/s^2)	$V_\omega(m/s)$	Amp (mm)
1	112	60	134	0.36	0.18
2	128	60	134	0.36	0.18
3	160	60	134	0.36	0.18
4	192	60	134	0.36	0.18
5	224	60	134	0.36	0.18

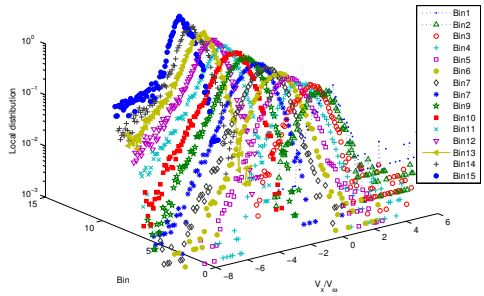

Figure 17: Local v_x distribution $f(v_x)$ on log-linear scales for vibration parameters Item 1 and in units of Item 1, as the bin number (in Table. 2).

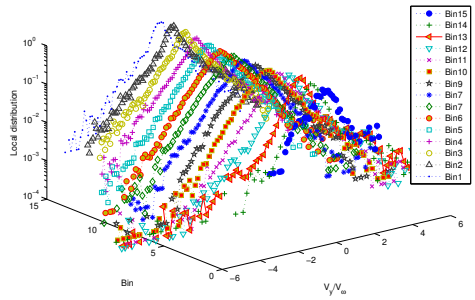

Figure 18: Local v_y distribution $f(v_y)$ on log-linearscales of vibration parameters Item 1 (in Table. 2).

A-2) Local state as a function of number of particles

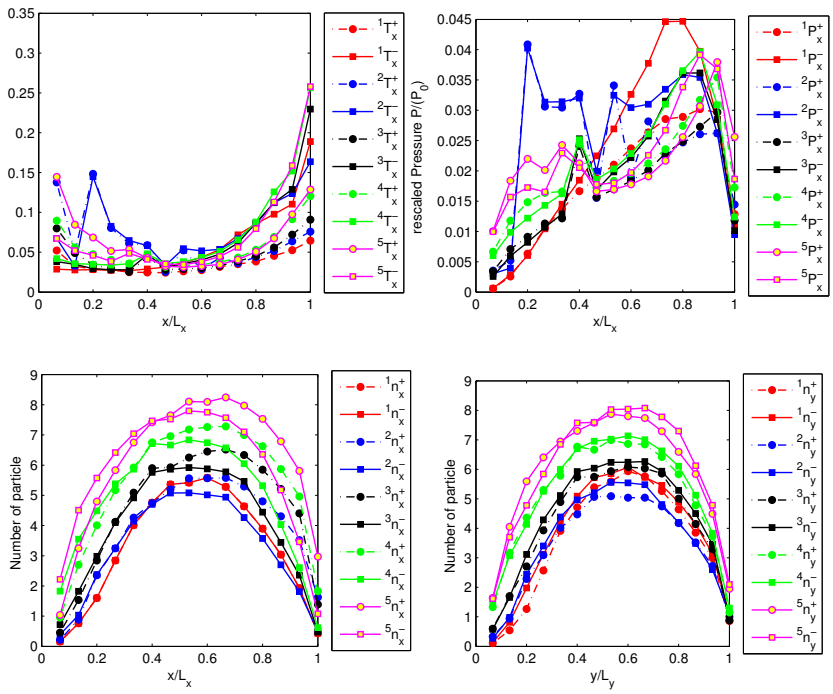

Figure 19: (upper left) Temperature in each bin as a function of the bin number, and rescaled by v_ω^2 . (upper right) Pressure with $v_x^\pm$. (low left) Number of particle with $v_x^\pm$. (low right) Number of particle with $v_y^\pm$. Parameters are in Table. 2.

Appendix D:experimental results on various inclination angle(from 5 to 85)

This Appendix D presents the experimental results of granular gases excited in a tilted plane. The tilted degree is varied from 5.5° to 90.5° by step of 5°. Furthermore, the number of particles are also varied in each angle. Here, we present parts of the experimental results.

Table 3: The vibration parameters are displayed in fig.20, 21 and 16.

Item	Freq(Hz)	Acc(m/s^2)	$V_\omega(m/s)$	Amp (mm)
1	60	124	0.36	0.18

Degree 5.5°

The local state obtained with a tilted angle of 5.5° are presented. The virational parameters are in Table.22. The number of particle is $N = 64$ (labelled 1), $N = 96$ (labelled 2), $N = 128$ (labelled 3), $N = 160$ (labelled 4),$N = 192$ (labelled 5), corresponding area fraction:0.129, 0.94, 0.259, 0.32 and 0.388, respectively.

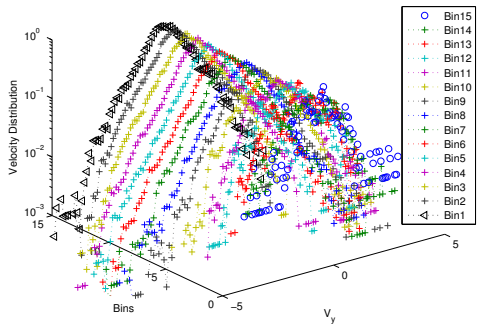

Figure 20: Local v_y distribution $f(v_y)$ on log-linearscales of vibration parameters ($D = 5.5°$ and $N = 64$ labelled 1 in Table. 22).

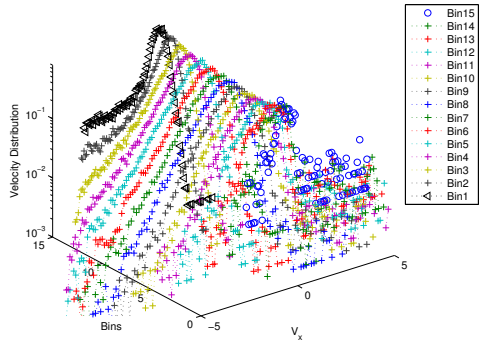

Figure 21: Local v_x distribution $f(v_x)$ on log-linearscales of vibration parameters ($D = 5.5°$ and $N = 64$ labelled 1 in Table. 22).

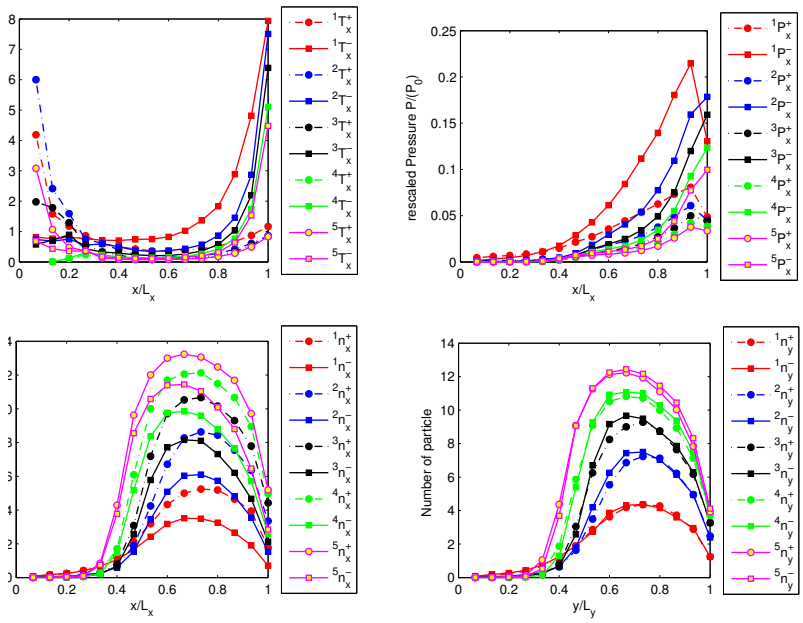

Figure 22: (upper left) The scaled temperature $T_x^{\pm}$ with velocity $v_x^{\pm}$. (upper right) The scaled pressure $p_x^{\pm}$ with velocity $v_x^{\pm}$. (low left) Number of particle with $v_x^{\pm}$. (low right) Number of particle with $v_y^{\pm}$. $D = 5.5°$ and vibrational parameters are in Table. 22.

Degree 10.5°

The local state obtained with a tilted angle of 10.5° are presented. The virational parameters are in Table.22. The number of particle is $N = 64$ (labelled 1), $N = 96$ (labelled 2), $N = 128$ (labelled 3), $N = 160$ (labelled 4),$N = 192$ (labelled 5), corresponding area fraction:0.129, 0.94, 0.259, 0.32 and 0.388, respectively.

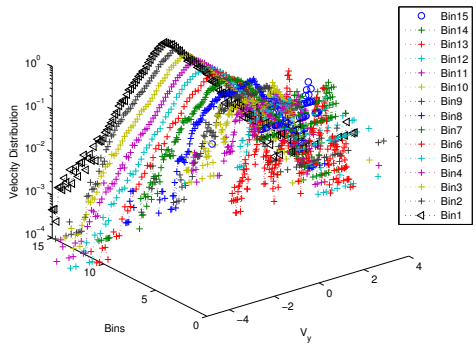

Figure 23: Local v_y distribution $f(v_y)$ on log-linearscales of vibration parameters ($D = 10.5°$ and $N = 64$ labelled 1 in Table. 22).

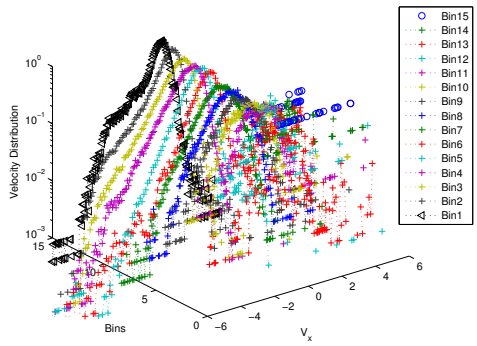

Figure 24: Local v_x distribution $f(v_x)$ on log-linearscales of vibration parameters ($D = 10.5°$ and $N = 64$ labelled 1 in Table. 22).

Degree 15.5°

The local state obtained with a tilted angle of 15.5° are presented. The virational parameters are in Table.22. The number of particle is $N = 64$ (labelled 1), $N = 96$ (labelled 2), $N = 128$ (labelled 3), $N = 160$ (labelled 4),$N = 192$ (labelled 5), corresponding area fraction:0.129, 0.94, 0.259, 0.32 and 0.388, respectively.

Degree 20.5°

The local state obtained with a tilted angle of 20.5° are presented. The virational parameters are in Table.22. The number of particle is $N = 64$ (labelled 1), $N = 96$ (labelled 2), $N = 128$ (labelled 3), $N = 160$ (labelled 4),$N = 192$ (labelled 5), corresponding area fraction:0.129, 0.94, 0.259, 0.32 and 0.388, respectively.

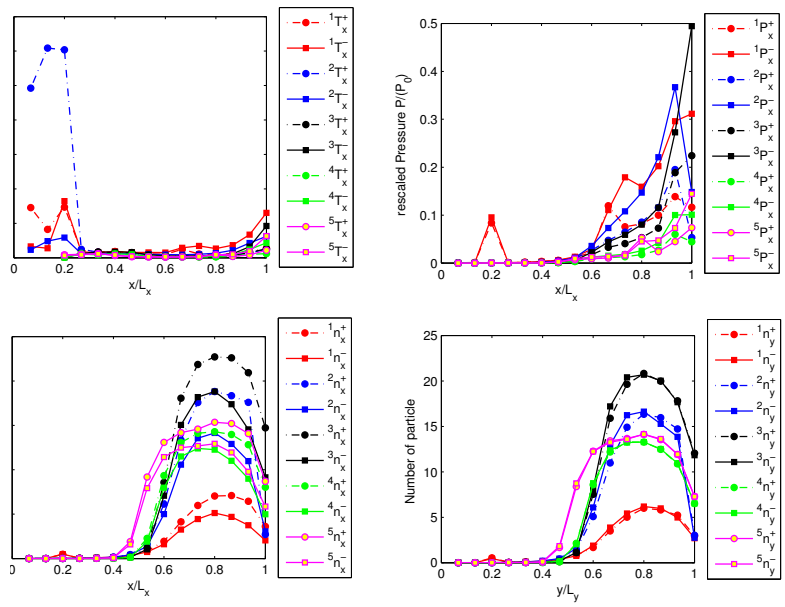

Figure 25: (upper left) The scaled temperature $T_x^{\pm}$ with velocity $v_x^{\pm}$. (upper right) The scaled pressure $p_x^{\pm}$ with velocity $v_x^{\pm}$. (low left) Number of particle with $v_x^{\pm}$. (low right) Number of particle with $v_y^{\pm}$. $D = 10.5°$ and vibrational parameters are in Table. 22.

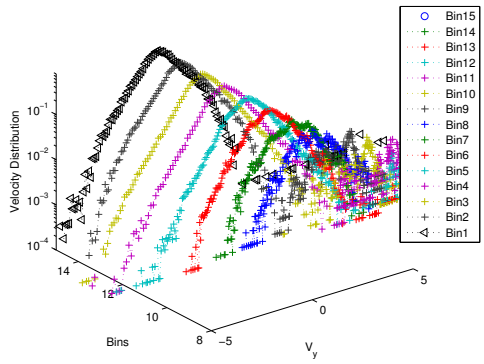

Figure 26: Local v_y distribution $f(v_y)$ on log-linearscales of vibration parameters ($D = 15.5°$ and $N = 64$ labelled 1 in Table. 22).

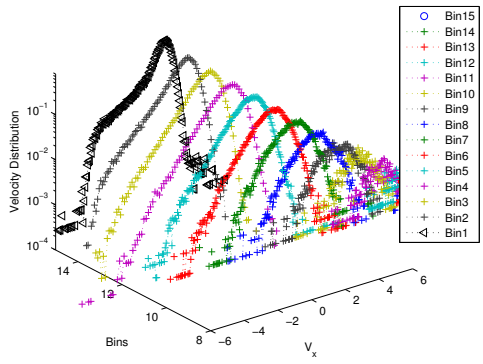

Figure 27: Local v_x distribution $f(v_x)$ on log-linearscales of vibration parameters ($D = 15.5°$ and $N = 64$ labelled 1 in Table. 22).

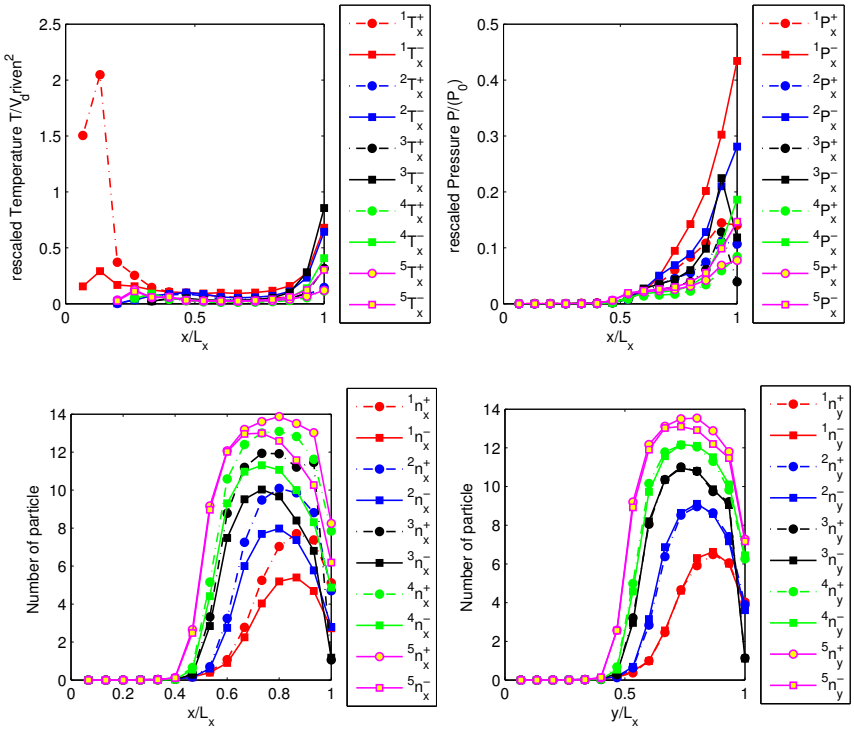

Figure 28: (upper left) The scaled temperature $T_x^{\pm}$ with velocity $v_x^{\pm}$. (upper right) The scaled pressure $p_x^{\pm}$ with velocity $v_x^{\pm}$. (low left) Number of particle with $v_x^{\pm}$. (low right) Number of particle with $v_y^{\pm}$. $D = 15.5°$ and vibrational parameters are in Table. 22.

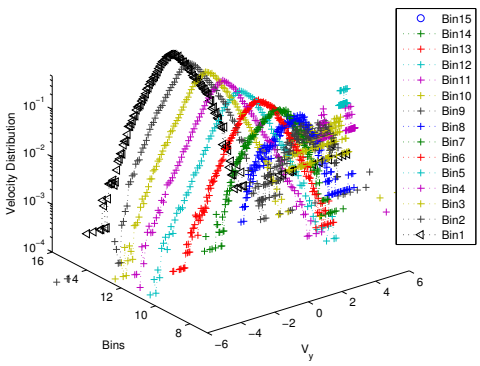

Figure 29: Local v_y distribution $f(v_y)$ on log-linearscales of vibration parameters ($D = 20.5°$ and $N = 64$ labelled 1 in Table. 22).

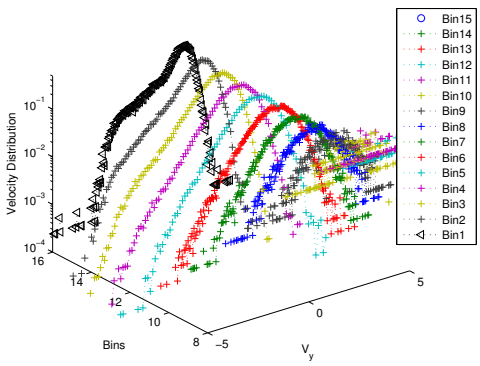

Figure 30: Local v_x distribution $f(v_x)$ on log-linearscales of vibration parameters ($D = 20.5°$ and $N = 64$ labelled 1 in Table. 22).

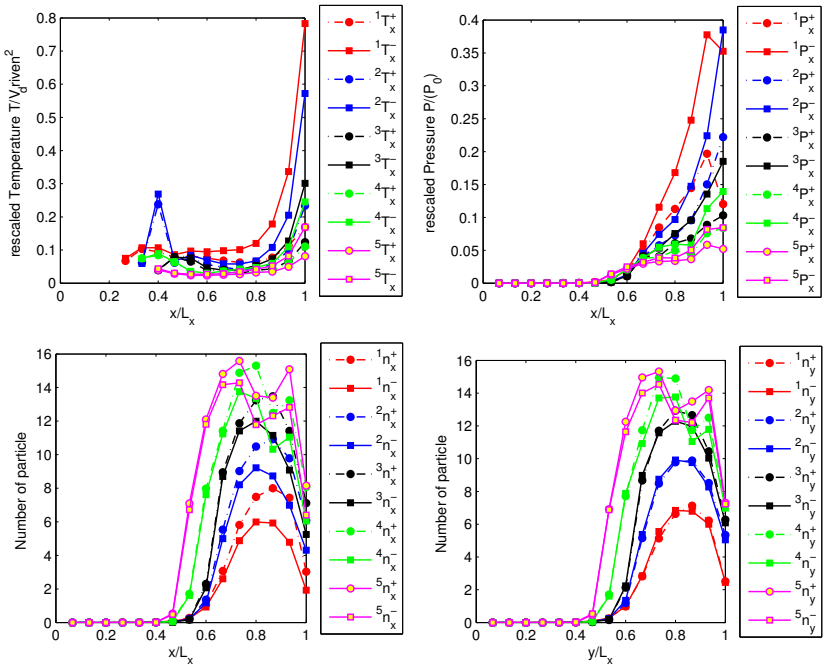

Figure 31: (upper left) The scaled temperature $T_x^{\pm}$ with velocity $v_x^{\pm}$. (upper right) The scaled pressure $p_x^{\pm}$ with velocity $v_x^{\pm}$. (low left) Number of particle with $v_x^{\pm}$. (low right) Number of particle with $v_y^{\pm}$. $D = 20.5°$ and vibrational parameters are in Table. 22.

Degree 25.5°

The local state obtained with a tilted angle of 20.5° are presented. The virational parameters are in Table.22. The number of particle is $N = 64$ (labelled 1), $N = 96$ (labelled 2), $N = 128$ (labelled 3), $N = 160$ (labelled 4),$N = 192$ (labelled 5), corresponding area fraction:0.129, 0.94, 0.259, 0.32 and 0.388, respectively.

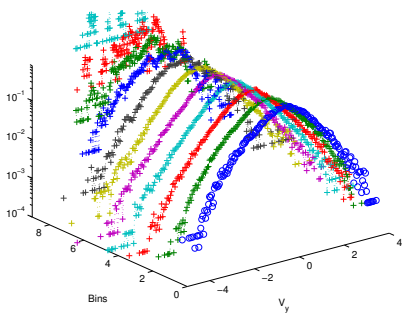

Figure 32: Local v_y distribution $f(v_y)$ on log-linearscales of vibration parameters ($D = 25.5°$ and $N = 64$ labelled 1 in Table. 22).

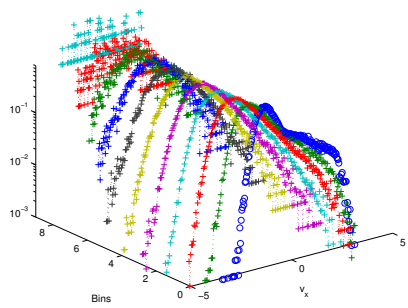

Figure 33: Local v_x distribution $f(v_x)$ on log-linearscales of vibration parameters ($D = 25.5°$ and $N = 64$ labelled 1 in Table. 22).

Degree 35.5°

The local state obtained with a tilted angle of 35.5° are presented. The virational parameters are in Table.22. The number of particle is $N = 64$ (labelled 1), $N = 96$ (labelled 2), $N = 128$ (labelled 3), $N = 160$ (labelled 4),$N = 192$ (labelled 5), corresponding area fraction:0.129, 0.94, 0.259, 0.32 and 0.388, respectively.

Degree 45.5°

The local state obtained with a tilted angle of 45.5° are presented. The virational parameters are in Table.22. The number of particle is $N = 64$ (labelled 1), $N = 96$ (labelled 2), $N = 128$ (labelled 3), $N = 160$ (labelled 4),$N = 192$ (labelled 5), corresponding area fraction:0.129, 0.94, 0.259, 0.32 and 0.388, respectively.

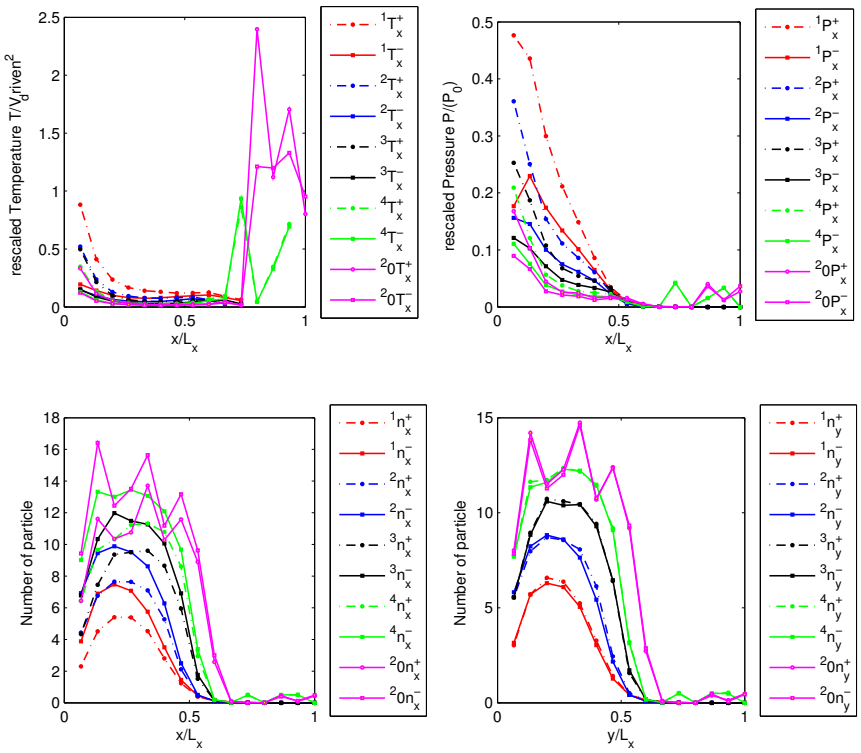

Figure 34: (upper left) The scaled temperature $T_x^{\pm}$ with velocity $v_x^{\pm}$. (upper right) The scaled pressure $p_x^{\pm}$ with velocity $v_x^{\pm}$. (low left) Number of particle with $v_x^{\pm}$. (low right) Number of particle with $v_y^{\pm}$. $D = 25.5°$ and vibrational parameters are in Table. 22.

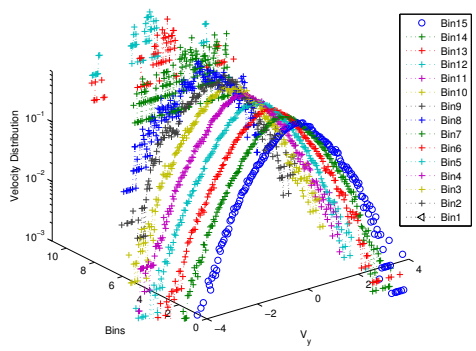

Figure 35: Local v_y distribution $f(v_y)$ on log-linearscales of vibration parameters ($D = 35.5°$ and $N = 64$ labelled 1 in Table. 22).

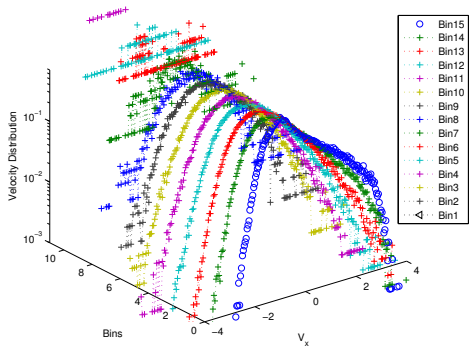

Figure 36: Local v_x distribution $f(v_x)$ on log-linearscales of vibration parameters ($D = 35.5°$ and $N = 64$ labelled 1 in Table. 22).

Degree 55.5°

The local state obtained with a tilted angle of 55.5° are presented. The virational parameters are in Table.22. The number of particle is $N = 64$ (labelled 1), $N = 96$ (labelled 2), $N = 128$ (labelled 3), $N = 160$ (labelled 4),$N = 192$ (labelled 5), corresponding area fraction:0.129, 0.94, 0.259, 0.32 and 0.388, respectively.

Degree 65.5°

The local state obtained with a tilted angle of 65.5° are presented. The virational parameters are in Table.22. The number of particle is $N = 64$ (labelled 1), $N = 96$ (labelled 2), $N = 128$ (labelled 3), $N = 160$ (labelled 4),$N = 192$ (labelled 5), corresponding area fraction:0.129, 0.94, 0.259, 0.32 and 0.388, respectively.

Degree 75.5°

The local state obtained with a tilted angle of 55.5° are presented. The virational parameters are in Table.22. The number of particle is $N = 32$ (labelled 1), $N = 64$ (labelled 2), $N = 96$ (labelled 3), $N = 128$ (labelled 4), $N = 160$ (labelled 5), corresponding area fraction:0.065, 0.129, 0.94, 0.259 and 0.32.

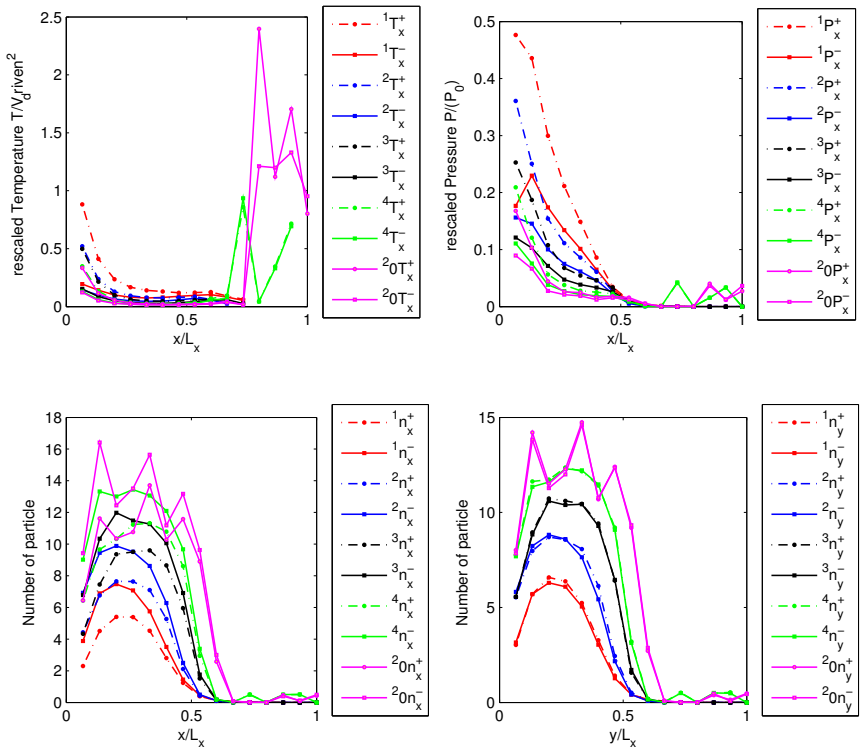

Figure 37: (upper left) The scaled temperature $T_x^{\pm}$ with velocity $v_x^{\pm}$. (upper right) The scaled pressure $p_x^{\pm}$ with velocity $v_x^{\pm}$. (low left) Number of particle with $v_x^{\pm}$. (low right) Number of particle with $v_y^{\pm}$. $D = 35.5°$ and vibrational parameters are in Table. 22.

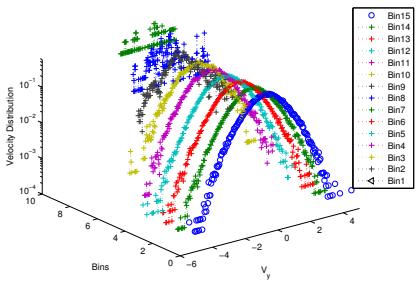

Figure 38: Local v_y distribution $f(v_y)$ on log-linearscales of vibration parameters ($D = 45.5°$ and $N = 64$ labelled 1 in Table. 22).

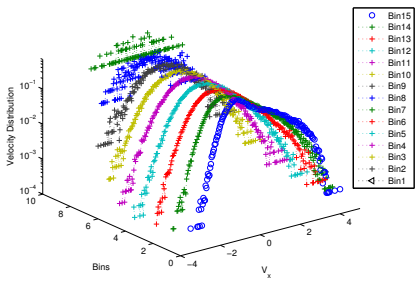

Figure 39: Local v_x distribution $f(v_x)$ on log-linearscales of vibration parameters ($D = 45.5°$ and $N = 64$ labelled 1 in Table. 22).

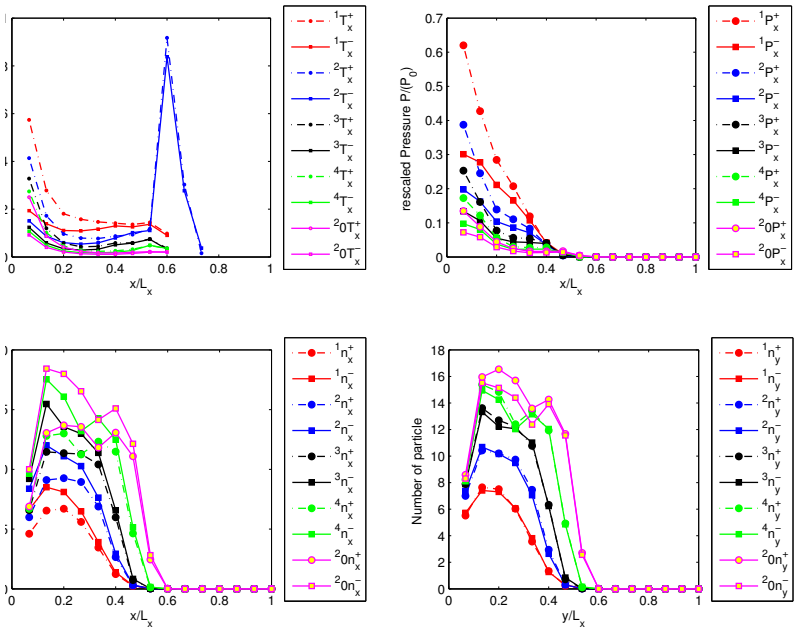

Figure 40: (upper left) The scaled temperature $T_x^{\pm}$ with velocity $v_x^{\pm}$. (upper right) The scaled pressure $p_x^{\pm}$ with velocity $v_x^{\pm}$. (low left) Number of particle with $v_x^{\pm}$. (low right) Number of particle with $v_y^{\pm}$. $D = 45.5°$ and vibrational parameters are in Table. 22.

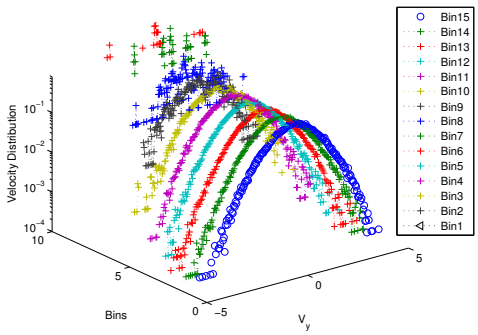

Figure 41: Local v_y distribution $f(v_y)$ on log-linearscales of vibration parameters ($D = 55.5°$ and $N = 64$ labelled 1 in Table. 22).

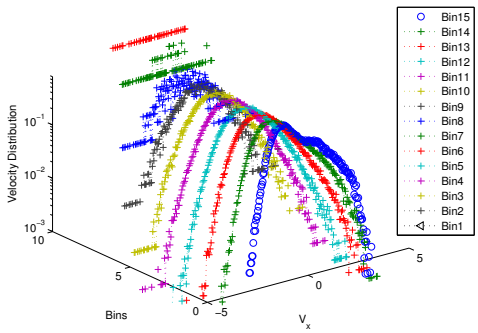

Figure 42: Local v_x distribution $f(v_x)$ on log-linearscales of vibration parameters ($D = 55.5°$ and $N = 64$ labelled 1 in Table. 22).

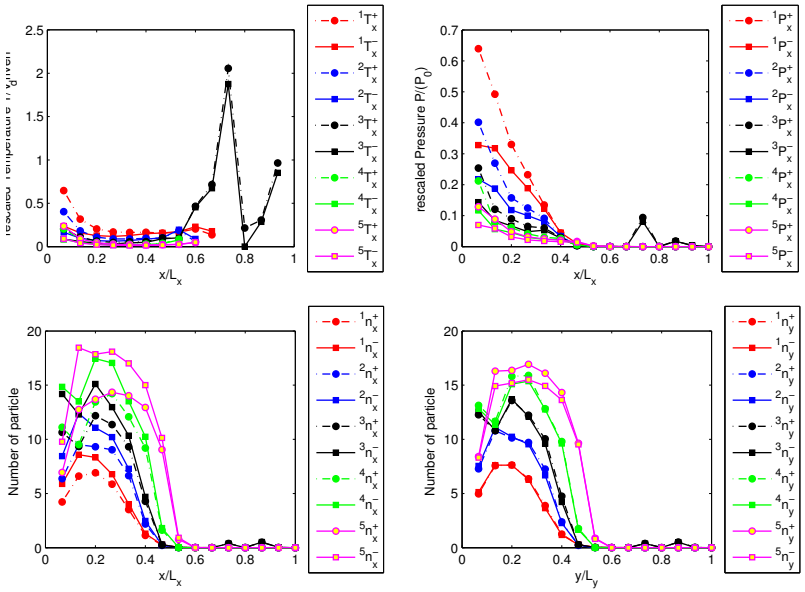

Figure 43: (upper left) The scaled temperature $T_x^{\pm}$ with velocity $v_x^{\pm}$. (upper right) The scaled pressure $p_x^{\pm}$ with velocity $v_x^{\pm}$. (low left) Number of particle with $v_x^{\pm}$. (low right) Number of particle with $v_y^{\pm}$. $D = 55.5°$ and vibrational parameters are in Table. 22.

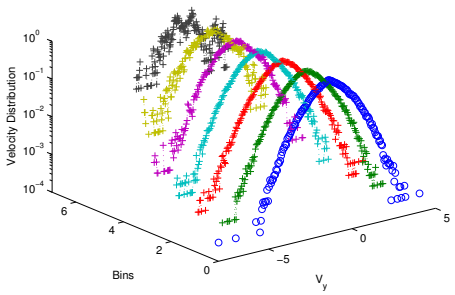

Figure 44: Local v_y distribution $f(v_y)$ on log-linearscales of vibration parameters ($D = 65.5°$ and $N = 64$ labelled 1 in Table. 22).

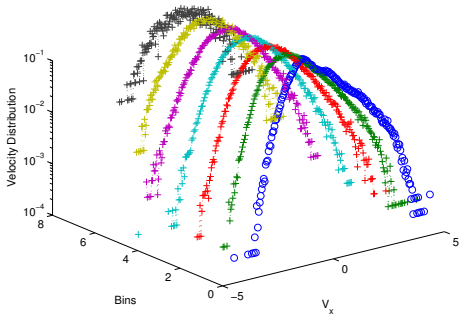

Figure 45: Local v_x distribution $f(v_x)$ on log-linearscales of vibration parameters ($D = 65.5°$ and $N = 64$ labelled 1 in Table. 22).

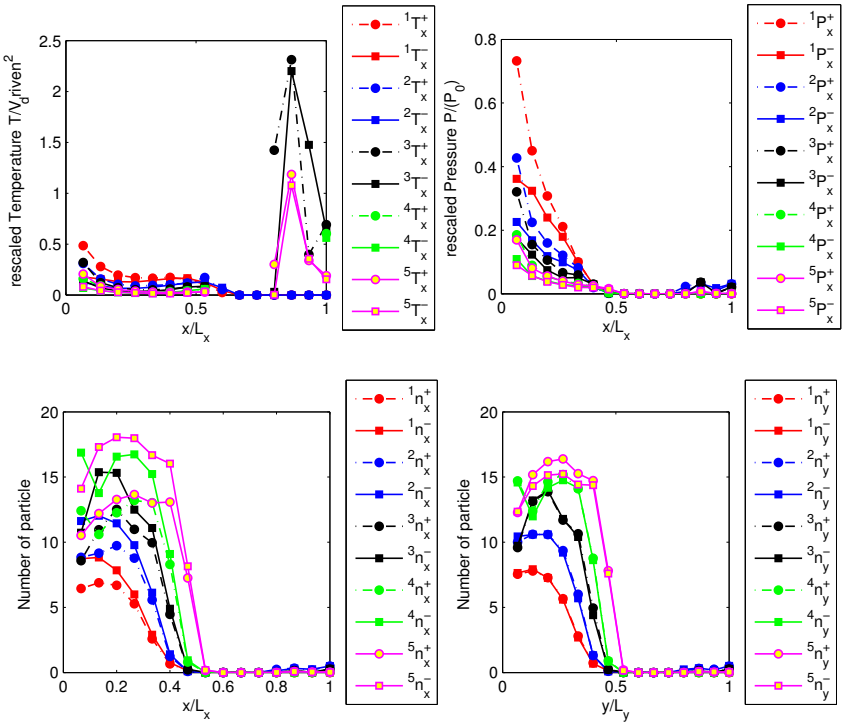

Figure 46: (upper left) The scaled temperature $T_x^{\pm}$ with velocity $v_x^{\pm}$. (upper right) The scaled pressure $p_x^{\pm}$ with velocity $v_x^{\pm}$. (low left) Number of particle with $v_x^{\pm}$. (low right) Number of particle with $v_y^{\pm}$. $D = 65.5°$ and vibrational parameters are in Table. 22.

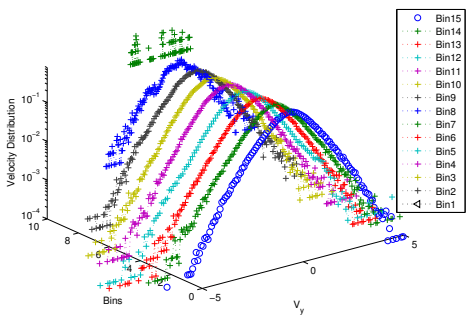

Figure 47: Local v_y distribution $f(v_y)$ on log-linearscales of vibration parameters ($D = 75.5°$ and $N = 64$ labelled 1 in Table. 22).

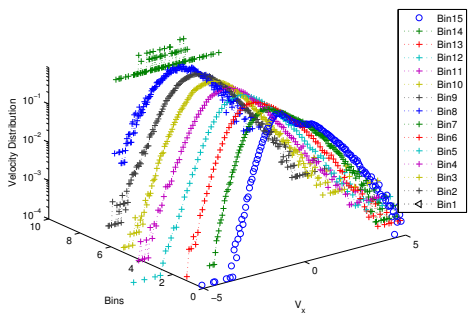

Figure 48: Local v_x distribution $f(v_x)$ on log-linearscales of vibration parameters ($D = 75.5°$ and $N = 64$ labelled 1 in Table. 22).

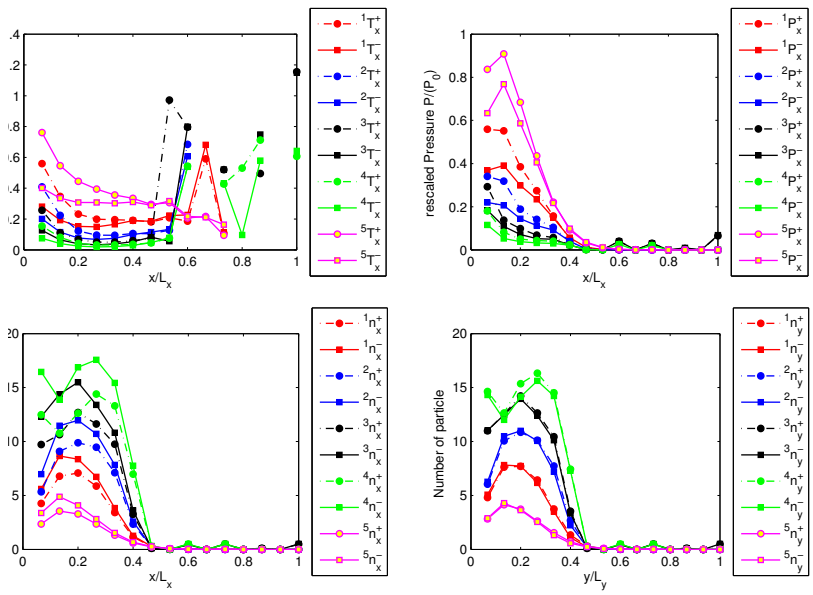

Figure 49: (upper left) The scaled temperature $T_x^{\pm}$ with velocity $v_x^{\pm}$. (upper right) The scaled pressure $p_x^{\pm}$ with velocity $v_x^{\pm}$. (low left) Number of particle with $v_x^{\pm}$. (low right) Number of particle with $v_y^{\pm}$. $D = 75.5°$ and vibrational parameters are in Table. 22.

Degree 85.5°

The local state obtained with a tilted angle of 85.5° are presented. The virational parameters are in Table.22. The number of particle is $N = 64$ (labelled 1), $N = 96$ (labelled 2), $N = 128$ (labelled 3), $N = 160$ (labelled 4),$N = 192$ (labelled 5), corresponding area fraction:0.129, 0.94, 0.259, 0.32 and 0.388, respectively.

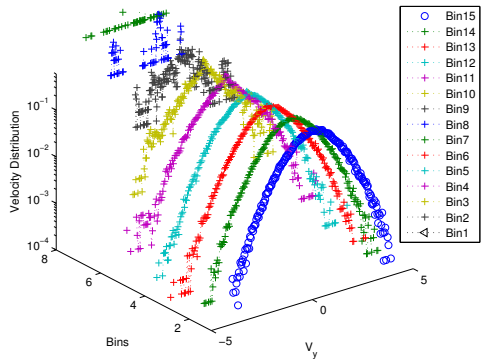

Figure 50: Local v_y distribution $f(v_y)$ on log-linearscales of vibration parameters ($D = 85.5°$ and $N = 64$ labelled 1 in Table. 22).

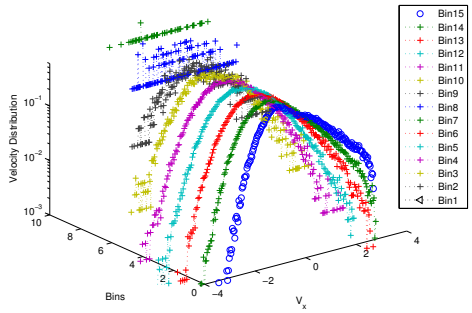

Figure 51: Local v_x distribution $f(v_x)$ on log-linearscales of vibration parameters ($D = 85.5°$ and $N = 64$ labelled 1 in Table. 22).

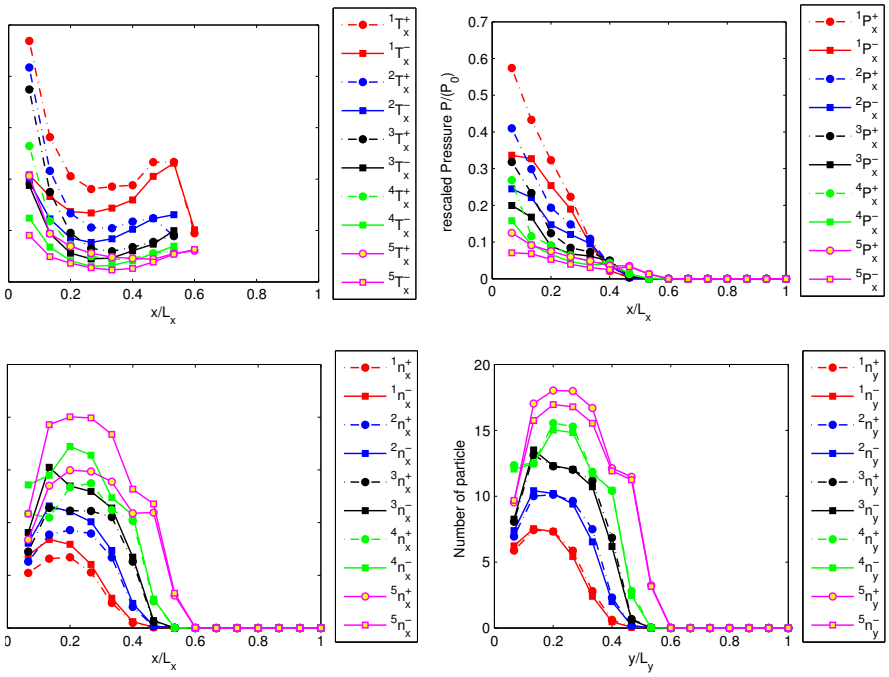

Figure 52: (upper left) The scaled temperature $T_x^{\pm}$ with velocity $v_x^{\pm}$. (upper right) The scaled pressure $p_x^{\pm}$ with velocity $v_x^{\pm}$. (low left) Number of particle with $v_x^{\pm}$. (low right) Number of particle with $v_y^{\pm}$. $D = 85.5°$ and vibrational parameters are in Table. 22.

References

[1] L. Vanel, D. Howell, D. Clark, R. P. Behringer, and E. Clement, "Memories in sand: Experimental tests of construction history on stress distributions under sandpiles", *Physcial Review E*, vol. 60, no. 5, Part a, pp. R5040–R5043, NOV 1999. xii, 3

[2] Y. Forterre and O. Pouliquen, "Long-surface-wave instability in dense granular flows", *Journal of Fluid Mechanics*, vol. 486, pp. 21–50, JUL 10 2003. xii, 4

[3] P. B. Umbanhowar, F. Melo, and H. L. Swinney, "Localized excitations in a vertically vibrated granular layer", *Nature*, vol. 382, no. 6594, pp. 793–796, AUG 29 1996. xii, 4

[4] J. M. Ottino and D. V. Khakhar, "Open problems in active chaotic flows: Competition between chaos and order in granular materials", *Chaos*, vol. 12, no. 2, pp. 400–407, JUN 2002. xii, 4

[5] D. M. Mueth, G. F. Debregeas, G. S. Karczmar, P. J. Eng, S. R. Nagel, and H. M. Jaeger, "Signatures of granular microstructure in dense shear flows", *Nature*, vol. 406, no. 6794, pp. 385–389, JUL 27 2000. xii, 4

[6] Andrea J. Liu and Sidney R. Nagel, "Nonlinear dynamics: Jamming is not cool anymore", *Nature*, vol. 396, pp. 21–22, 1998. xii, 4, 5

[7] Zexin Zhang, Ning Xu, Daniel T. N. Chen, Peter Yunker, Ahmed M. Alsayed, Kevin B. Aptowicz, Piotr Habdas, Andrea J. Liu, Sidney R. Nagel, and Arjun G. Yodh, "Thermal vestige of the zero-temperature jamming transition", *Nature*, vol. 459, no. 7244, pp. 230–233, MAY 14 2009. xii, 5

[8] P. Evesque, "The jamming surface of granular matter determined from soil mechanics results", *Poudre & Grains*, vol. 11, pp. 58–59, 2000. xii, 4, 5

[9] E. Falcon, R. Wunenburger, P. Evesque, S. Fauve, C. Chabot, Y. Garrabos, and D. Beysens, "Cluster formation in a granular medium fluidized by vibrations in low gravity l_1", *Phy. Rev. Lett*, vol. 83, pp. 440–444, 1999. xii, 6, 30, 31

[10] P. Eshuis, K. van der Weele, D. van der Meer, and D. Lohse, "Granular leidenfrost effect: Experiment and theory of floating particle clusters", *Phy. Rev. Lett.*, vol. 95, no. 25, DEC 16 2005. xii, 6, 7

[11] P. Evesque, "Granular gas and the 2nd principle of thermodynamics", *Poudre & Grains*, vol. 21, pp. 1–19, 2013. xii, 7

[12] O. Herbst, P. Müller, M. Otto, and A. Zippelius, "Local equation of state and velocity distributions of a driven granular gas", *Phy. Rev. E*, vol. 70, pp. 051313, 2004. xii, xiv, 21, 22, 23, 24, 36, 48, 50, 51, 60, 61, 72, 77, 83, 84, 86, 88, 106, 107

[13] Y. Chen, P. Evesque, and M. Hou, "Breakdown of energy equipartition in vibro-fluidized granular media in micro-gravity", *Chin. Phys. Lett*, vol. 29, pp. 074501, 2012. xiv, 30, 31, 44, 48, 50, 51, 60, 61, 66, 70, 74, 80, 82, 88

[14] P. G. de Gennes, "Granular matter: a tentative view", *Reviews of Modern Physics*, vol. 71, pp. 374–382, 1999. 1, 3

[15] R. L. Brown and J. C. Richards, *Principles of powder mechanics essays on the packing and flow of powders and bulk solids*, Pergamon, Oxford, 1970. 1

[16] L. Francois, *Contribution aux approches numérique de la densification d'assemblées granulaires*, PhD thesis, Université sw liège, 2006. 1

[17] T. Pöschel and T. Schwager, *Computational Granular Dynamics, Model and Algorithms*, Springer-Verlag, Berlin, 2005. 2, 10, 11, 62, 67

[18] P. G. de Gennes, "Soft matter", November 1999. 2

[19] J. Eggers, "Sand as Maxwell's demon", *Phy. Rev. Lett*, vol. 83, no. 25, pp. 5322–5325, DEC 20 1999. 3

[20] J. L. Finney, "Random packings and structure of simple liquids. 1. Greometry of random close packing", *Prceedings of the royal society of London series a-Mathmatical and physical sciences*, vol. 319, no. 1539, pp. 479, 1970. 3

[21] V. Frette, K. Christensen, A. MaltheSorenssen, J. Feder, T. Jossang, and P. Meakin, "Avalanche dynamics in a pile of rice", *Nature*, vol. 379, no. 6560, pp. 49–52, JAN 4 1996. 3

[22] P. Evesque and J. Rajchenbach, "Instability in a sand heap", *Phy. Rev. Lett*, vol. 62, pp. 44–46, Jan 1989. 3

[23] J. P. Bouchaud, M. E. Cares, and P. Claudin, "Stress-distribution in granular media and nonlinear-wave equation", *Journal de physique I* , vol. 5, no. 6, pp. 639–656, JUN 1995.

[24] A. Modaressi, S. Boufellouh, and P. Evesque, "Modelling of stress distribution in granular pile : comparison with centrifuge experiments", *Chaos*, vol. 9, pp. 523–543, 1999.

[25] P. Evesque, S. Noblet, and G. Rault, "Stress in conic piles determined by a centrifuge experiment: Breakdown of scaling hypothesis", *Phys. Rev. E*, vol. 59, pp. R6259–R6262, Jun 1999.

[26] P. Evesque and S. Boufellouh, "Stress distribution in an inclined pile: Soil mechanics calculation using finite element technique", in *Powders and Grains*, R. P. Behringer and J. T. Jenkins, Eds., 1997, pp. 295–298.

[27] A. Modaressi and P.Evesque, "Is the friction angle the maximum slope of a free surface of a non cohesive material?", *Poudre & Grains*, vol. 12, pp. 83–102, 2001. 3

[28] F. Radjai, M. Jean, J. Moreau, and S. Roux, "Force distributions in dense two-dimensional granular systems", *Phys. Rev. Lett.*, vol. 77, pp. 274–277, Jul 1996. 3

[29] I. S. Aranson, B. Meerson, P. V. Sasorov, and V. M. Vinokur, "Phase separation and coarsening in electrostatically driven granular media", *Phy. Rev. Lett*, vol. 88, no. 20, MAY 20 2002. 4

[30] Igor S. Aranson and Lev S. Tsimring, "Patterns and collective behavior in granular media: Theoretical concepts", *Reviews of Modern Physics*, vol. 78, no. 2, pp. 641–692, APR-JUN 2006. 4

[31] Debashish Chowdhury, Ludger Santen, and Andreas Schadschneider, "Statistical physics of vehicular traffic and some related systems", *Physics Reports*, vol. 329, no. 4C6, pp. 199 – 329, 2000. 4

[32] C. Bizon, M. D. Shattuck, J. B. Swift, W. D. McCormick, and H. L. Swinney, "Patterns in 3d vertically oscillated granular layers: Simulation and experiment", *Phy. Rev. Lett*, vol. 80, no. 1, pp. 57–60, JAN 5 1998. 4

[33] A. Rosato, Katherine J. Strandburg, F. Prinz, and Robert H. Swendsen, "Why the brazil nuts are on top: Size segregation of particulate matter by shaking", *Phy. Rev. Lett*, vol. 58, pp. 1038–1040, Mar 1987. 4

[34] J. B. Kinght, H. M. Jaeger, and S. R. Nagel, "Vibration-induced size separation in granular media-the convection connection ", *Phy. Rev. Lett*, vol. 70, no. 24, pp. 3728–3731, JUN 14 1993. 4

[35] R. M. Nedderman, *Statics and Kinematics of Granular Materials*, Cambridge University Press, Cambridge, second edition, 1992. 4

[36] J. Duran, A. Reisinger, and P. G. de Gennes, *Sands, Powders, and Grains: An Introduction to the physics oF Granular Materials*, Springer-Verlag, New York, 1999.

[37] J. P. Gollub and J. S. Langer, "Pattern formation in nonequilibrium physics", *Reviews of Modern Physics*, vol. 71, no. 2, SI, pp. S396–S403, MAR 1999.

[38] C. Bowman and A. C. Newell, "Natural patterns and wavelets", *Reviews of Modern Physics*, vol. 70, no. 1, pp. 289–301, JAN 1998.

[39] H. M. Jaeger, S. R. Nagel, and R. P. Behringer, "Granular solids, liquids, and gases", *Rev. Mod. Phys.*, vol. 68, pp. 1259–1273, Oct 1996. 4, 5

[40] L. P. Kadanoff, "Built upon sand: Theoretical ideas inspired by granular flows", *Rev. Mod. Phys.*, vol. 71, pp. 435–444, Jan 1999. 24

[41] J. M. Ottino and D. V. Khakhar, "Mixing and segregation of granular materials", *Annual Review of Fluid Mechanics*, vol. 32, no. 1, pp. 55–91, 2000.

[42] J. Rajchenbach, "Granular flows", *Adv. Phys.*, vol. 49, pp. 229–256, 2000.

[43] G. H. Ristow, *Pattern Formation in Granular Materials*, Springer, New York, 2000. 4

[44] E. Opsomer, F. Ludewig, and N. Vandewalle, "Phase transitions in vibrated granular systems in microgravity", *Phy. Rev. E*, vol. 84, no. 5, Part 1, NOV 28 2011. 6

[45] P. Eshuis, K. van der Weele, D. van der Meer, Robert Bos, and D. Lohse, "Phase diagram of vertically shaken granular matter", *Physics of Fluids*, vol. 19, no. 12, DEC 2007. 6

[46] Hongqiang Wang, *Experiments and Simulations on Granular Gases*, PhD thesis, University of Massachusetts-Amherst, 2011. 7, 8

[47] I. Goldhirsch, "Rapid granular flows", *Annual Review of Fluid Mechanics*, vol. 35, pp. 267–293, 2003. 7, 8, 82

[48] E. Fukushima, "Nuclear magnetic resonance as a tool to study flow", *Annual Review of Fluid Mechanics*, vol. 31, pp. 95–123, 1999. 8

[49] R. D. Wildman, J. M. Huntley, and D. J. Parker, "Convection in highly fluidized three-dimensional granular beds", *Phy. Rev. Lett*, vol. 86, no. 15, pp. 3304–3307, APR 9 2001. 8

[50] S. Warr, J. M. Huntley, and G. T. H. Jacques, "Fluidization of a two-dimensional granular system: Experimental study and scaling behavior", *Phy. Rev. E*, vol. 52, pp. 5583–5595, Nov 1995. 8

[51] S. WARR and J. M. HUNTLEY, "Energy input and scaling laws for a single-particle vibrating in one-dimension", *Phy. Rev. E*, vol. 52, no. 5, Part b, pp. 5596–5601, NOV 1995. 8

[52] W. Losert, D. G. W. Cooper, J. Delour, A. Kudrolli, and J. P. Gollub, "Velocity statistics in excited granular media", *chaos*, vol. 9, pp. 682–690, 1999. 9, 19, 35, 38, 60, 82

[53] F. Rouyer and N. Menon, "Velocity fluctuations in a homogeneous 2d granular gas in steady state", *Phy. Rev. Lett*, vol. 85, pp. 3676–3679, Oct 2000. 35, 36, 38

[54] A. Kudrolli and J. Henry, "Non-gaussian velocity distributions in excited granular matter in the absence of clustering", *Phy. Rev. E*, vol. 62, pp. 1489, 2000. 35, 98, 110

[55] J. S. Olafsen and J. S. Urbach, "Velocity distributions and density fluctuations in a granular gas", *Phy. Rev. E*, vol. 60, pp. R2468–R2471, Sep 1999. 9, 35, 82

[56] G. W. Baxter and J. S. Olafsen, "Kinetics - Gaussian statistics in granular gases", *Nature*, vol. 425, no. 6959, pp. 680, 2003. 9, 36, 60

[57] K. Kohlstedt, A. Snezhko, M. V. Sapozhnikov, I. S. Aranson, J. S. Olafsen, and E. Ben-Naim, "Velocity distributions of granular gases with drag and with long-range interactions", *Phy. Rev. Lett*, vol. 95, pp. 068001, Aug 2005. 9, 31

[58] D. L. Blair and A. Kudrolli, "Collision statistics of driven granular materials", *Phy. Rev. E*, vol. 67, no. 4, Part 1, APR 2003. 9, 109, 112

[59] G. A. Bird, *Molecular Gas Dynamics*, Clarendon Press, OXford, 1976. 10

[60] C. K. K. Lun, "Kinetic-theory for granular flow of dense, slightly inelastic, slightly rough spheres", *Journal of Fluid Mechanics*, vol. 233, pp. 539–559, DEC 1991. 10

[61] T. Pöschel and S. Luding, *Granular Gases*, Springer, 2000. 10

[62] A. Baldassarri, U. Marini Bettolo Marconi, A. Puglisi, and A. Vulpiani, "Driven granular gases with gravity", *Phy. Rev. E*, vol. 64, pp. 011301, Jun 2001. 10, 98, 110, 112

[63] S. J. Moon, J. B. Swift, and H. L. Swinney, "Steady-state velocity distributions of an oscillated granular gas", *Phys. Rev. E*, vol. 69, pp. 011301, Jan 2004. 10, 36

[64] J. S. van Zon and F. C. MacKintosh, "Velocity distributions in dilute granular systems", *Phy. Rev. E*, vol. 72, pp. 051301, 2005. 10, 36

[65] J. S. van Zon and F. C. MacKintosh, "Velocity distributions in dissipative granular gases", *Phy. Rev. Lett*, vol. 93, no. 3, JUL 16 2004. 10

[66] E. L. Grossman, Tong Zhou, and E. Ben-Naim, "Towards granular hydrodynamics in two dimensions", *Phy. Rev. E*, vol. 55, pp. 4200–4206, 1997. 10, 53, 56, 60, 81, 82, 84, 85

[67] M. J. Ruizmontero J. Javier Brey and D. Cubero, "Homogeneous cooling state of a low-density granular flow", *Phy. Rev. E*, vol. 54, pp. 3664–3671, 1996. 10, 22, 77

[68] P. Evesque, "Statistical mechanics of granular media: An approach la boltzmann", *Poudre & Grains*, vol. 6, pp. 13–19, 1999. 13

[69] S. Chapman and T. G. Cowling, *The mathematical theory of non-uniform gases*, Cambridge University Press, 1970. 13, 15, 16, 92, 94

[70] N. V. Brilliantov and T. Pöschel, *Kinetic Theory of Granular Gases*, Oxford University Press, New York, 2004. 15, 16, 21, 53, 81

[71] A. Goldshtein and M. Shapiro, "Mechanics of collisional motion of granular materials. part 1. general hydrodynamic equations", *J. Fluid Mech*, vol. 282, pp. 75–114, 1995. 14

[72] Sergei E. Esipov and Thorsten Pöschel, "The granular phase diagram", *J. Stat. Phys*, vol. 86, pp. 1385, 1997. 14, 16, 18

[73] T. P. C. van Noije and M. H. Ernst, "Velocity distributions in homogeneous granular fluids: the free and the heated case", *Granular Matter*, vol. 1, pp. 57–64, 1998. 13, 14, 37

[74] D. R. Wilkinson and S. F. Edwards, "Spontaneous interparticle percolation", *Proc. R. Soc. Lond. A*, vol. 381, pp. 33–51, 1982. 14

[75] N. Sela and I. Goldhirsch, "Hydrodynamic equations for rapid flows of smooth inelastic spheres, to burnett order", *J. Fluid Mech*, vol. 361, pp. 41–74, 1998. 14

[76] M. H. Ernst and R. Brito, "Driven inelastic maxwell models with high energy tails", *Phy. Rev. E.*, vol. 65, pp. 4, 2002. 14, 37

[77] J. A. McLennan, *Introduction to nonequilibrium statistical mechanics*, Prentice Hall, London, 1989. 14, 15

[78] T. P. C. van Noije, M. H. Ernst, and R. Brito, "Ring knetic theory for an idealized granular gas", *Physica A*, vol. 251, pp. 266–283, 1998. 15, 16

[79] P. Resibois and M. de Leener, *Classical Kinetic Theory of Fluids*, Wiley & son, New York, 1977.

[80] P. P. J. M. Schram, *Kinetic Theory of Gases and Plasmas*, Kluwer Academic Publishers, AA Dordrecht, 1991. 16

[81] J. Javier Brey, D. Cubero, and M. J. Ruiz-Montero, "High energy tail in the velocity distribution of a granular gas", *Phy. Rev. E*, vol. 59, pp. 1256–1258, 1999. 19, 82

[82] M.Hou, R.Liu, G.Zhai, Z.Sun, K.Lu, Y. Garrabos, and P. Evesque, "Velocity distribution of vibration-driven granular gas in knudsen regime in microgravity", *Microgravity Sci Technol*, vol. 20, pp. 73–80, 2008. 19, 20, 30, 31, 34

[83] M. Leconte, Y. Garrabos, E. Falcon, C. Lecontre-Chabot, F. Palencia, P. Evesque, and D. Beysens, "Microgravity experiments on vibrated gran-

ular gases in a dilute regimes: non-classical statistics", *J. Stat. Mech.*, vol. 07, pp. 07012, 2006. 20, 31

[84] J. Javier Brey, James W. Dufty, Chang Sub Kim, and Andrés Santos, "Hydrodynamics for granular flow at low density", *Phy. Rev. E*, vol. 58, pp. 4638–4653, Oct 1998. 20

[85] P. K. Haff, "Grain flow as a fluid-mechanical phenomenon", *J. Fluid Mech*, vol. 134, pp. 401–430, 1983. 20, 26

[86] P. Evesque, "'hydrodynamique' avec dissipation. vers un mlange, ou une sgrgation ?", *Poudre & Grains*, vol. 20, pp. 11–28, 2013. 21

[87] B. J. Glasser and I. Goldhirsch, "Scale dependence, correlations, and fluctuations of stresses in rapid granular flows", *Physics of Fluids*, vol. 13, no. 2, pp. 407–420, 2001. 23, 84

[88] P. Evesque, "Are temperature and other thermodynamics variables efficient concepts for describing granular gases and/or flows ?", *Poudre & Grains*, vol. 13, pp. 20–26, 2002. 23, 24, 60, 74

[89] A. Baldassarri, A. Barrat, G. D'Anna, V. Loreto, P. Mayor, and A. Puglisi, "What is the temperature of a granular medium?", *Condens Matter*, vol. 17, pp. S2405–S2428, 2005. 24

[90] I. Goldhirsch, "Introduction to granular temperature", *Power Technology*, vol. 182, pp. 130–136, 2008. 23, 74, 81

[91] S. Ogawa, "Mutitemperature theory of granular materials", in *Continuum Mechanics and Statistical Approaches in the Mechanics of Granular Materials, Gakujusu Bunken Fukyu-Kai*, M. Satake S. C. Cowin, Ed. 2004, U. S.-Japan Symp. 23

[92] R. D. Widman and D. J. Parker, "Coexistence of two granular temperature in binary vibrofluidized beds", *Phy. Rev. Lett*, vol. 88, pp. 64301, 2002. 23

[93] J. Villain and P.Evesque, "Shaken sand, stress and test particles", *Poudre &Grains*, vol. 12, pp. 37–51, 2001. 24, 73

[94] C. S. Campbell, "Granular flows-an overview", *Power Technol*, vol. 162(3), pp. 208–229, 2006. 24

[95] k. Hutter and K. R. Rajagopal, "On the flows of granular materials", *Contin. Mech. Thermodyn*, vol. 6, pp. 81–139, 1994. 24

[96] Y. Srebro and D. Levine, "Exactly solvable model for driven dissipative systems", *Phys. Rev. Lett.*, vol. 93, pp. 240601, Dec 2004. 25

[97] Y. Shokef and D. Levine, "Energy distribution and effective temperatures in a driven dissipative model", *Phys. Rev. E*, vol. 74, pp. 051111, Nov 2006. 25

[98] Y. Jiang and M. Liu, "Granular solid hydrodynamics", *Granular Matter*, vol. 11, no. 3, pp. 139–156, MAY 2009. 25, 26, 46, 49, 51

[99] L. Onsager, "Reciprocal relations in irreversible processes. i.", *Phys. Rev.*, vol. 37, pp. 405–426, Feb 1931. 25

[100] Y. Grasselli, G. Bossis, and G. Goutallier, "Velocity-denpendent restitution coefficient and granular cooling in microgravity", *Europhysics Letters*, vol. 86, pp. 60007, 2009. 31

[101] P. Evesque, "Granular media under vibration in zero-gravity: transition from rattling to granular gas", *Poudre & Grains*, vol. 19, pp. 1–4, 2011. 31

[102] P. Evesque, "Microgravity and dissipative granular gas in a vibrated container: a gas with an asymmetric speed distribution in the vibration direction, but with a null mean speed everywhere", *Poudre & Grains*, vol. 18, pp. 1–19, 2010. 31

[103] S. Warr, J. M. Huntley, and G. T. H. Jacques, "Fluidization of a two-dimensional granular system: Experimental study and scaling behavior", *Phy. Rev. E*, vol. 52, pp. 5538, 1995. 35

[104] I. S. Aranson and J. S. Olafsen, "Velocity fluctuations in electrostatically driven granular media", *Phys. Rev. E*, vol. 66, pp. 061302, Dec 2002. 35, 38

[105] P. Evesque, "On the role of boundary condition on the speed- & impact-distributions in dissipative granular gases in knudsen regime excited by vibration", *Poudre & Grains*, vol. 15, pp. 1–16, 2005. 36

[106] P. Evesque, "Boundary conditions and the dynamics of a dissipative granular gas: slightly dense case", *Poudre & Grains*, vol. 16, pp. 38–62, 2007. 36

[107] S. Hussain Shah, Y. Li, and M. Hou, "Effect of number density on velocity distributions in a driven quasi-two-dimensional granular gas", *Chinese Physics B)*, vol. 19, pp. 108203, 2010. 36, 38

[108] A. Barrat and E. Trizac, "Random inelasticity and velocity fluctuations in a driven granular gas", *European Physical Journal E*, vol. 11, no. 1, pp. 99–104, MAY 2003. 36, 37

[109] A. Barrat, E. Trizac, and M. H. Ernst, "Granular gases: dynamics and collective effects", *Journal of physics-condensed matter*, vol. 17, no. 24, SI, pp. S2429–S2437, Jun 22 2005. 37

[110] A. Puglisi, V. Loreto, U. M. B. Marconi, and A. Vulpiani, "Kinetic approach to granular gases", *Phy. Rev. E*, vol. 59, pp. 5582–5595, 1999. 37

[111] T. P. C. van Noije, M. H. Ernst, E. Trizac, and I. Pagonabarraga, "Randomly driven granular fluids: Large-scale structure", *Phy. Rev. E*, vol. 59, pp. 4326–4341, 1999.

[112] V. Garzo and J. M. Montanero, "Transport coefficients of a heated granular gas", *Phy. Rev. E*, vol. 313, pp. 336–356, 2002.

[113] Sung Joon Moon, M. D. Shattuck, and J. B. Swift, "Velocity distributions and correlations in homogeneously heated granular media", *Phy. Rev. E*, vol. 64, pp. 031303, Aug 2001.

[114] J. M. Montanero and A. Santos, "Computer simulation of uniformly heated granular fluids", *Granular Matter*, vol. 2, no. 2, pp. 53–64, MAY 2000. 37

[115] Yanpei Chen, Meiying Hou, Yimin Jiang, and Mario Liu, "Hydrodynamics of granular gases with a two-peak distribution", *Phys. Rev. E*, vol. 88, pp. 052204, Nov 2013. 45, 67, 88, 92

[116] P. Evesque, "Hydrodynamics with dissipation. towards mixing or demixing?", *Poudre & Grains*, vol. 20, pp. 1–26, 2012. 45

[117] P. G. Gennes and J. Prost, *The physics of Liquid Crystals*, Clarendon Press, 1993. 46

[118] Y. Jiang and M. Liu, "From elasticity to hypoplasticity: Dynamics of granular solids", *Phys. Rev. Lett.*, vol. 99, pp. 105501, Sep 2007. 46, 49

[119] G. Gudehus, Y. Jiang, and M. Liu, "Seismo- and thermodynamics of granular solids", *Granular Matter*, vol. 13, no. 4, pp. 319–340, AUG 2011. 46

[120] L. Bocquet, W. Losert, D. Schalk, T. C. Lubensky, and J. P. Gollub, "Granular shear flow dynamics and forces: Experiment and continuum theory", *Phy. Rev. E*, vol. 65, pp. 011307, Dec 2001. 47

[121] S. Luding, "Towards dense, realistic granular media in 2D", *Nonlinearity*, vol. 22, no. 12, pp. R101–R146, DEC 2009. 49, 51

[122] J. Javier Brey, M. J. Ruiz-Montero, and F. Moreno, "Boundary conditions and normal state for a vibrated granular fluid", *Phy. Rev. E*, vol. 62, pp. 5339–5346, 2000. 52, 54, 61, 66, 70, 72, 81, 82, 88

[123] D. Van der Meer and P. Reimann, "Temperature anisotropy in a driven granular gas", *Europhys.Lett*, vol. 74(3), pp. 384–390, 2006. 53

[124] K Feitosa and N Menon, "Breakdown of energy equipartition in a 2D binary vibrated granular gas", *Phys. Rev. Lett.*, vol. 88, no. 19, MAY 13 2002. 54, 60

[125] Hong-Qiang Wang and Narayanan Menon, "Heating mechanism affects equipartition in a binary granular system", *Phys. Rev. Lett.*, vol. 100, no. 15, APR 18 2008. 54, 61

[126] W. G. Vincenti and C. H. Kruger, *Introduction to Physical Gas Dynamics*, John Wiley & Sons, New York, 1965. 55, 81

[127] O. Herbst, P. Muller, and A. Zippelius, "Local heat flux and energy loss in a two-dimensional vibrated granular gas", *Phy. Rev. E*, vol. 72, no. 4, Part 1, OCT 2005. 60, 66, 79

[128] P. Evesque, Y. Garrabos, C. Lecoutre, F. Palencia, and D. Beysens, "Dilute dissipative granular gas in knudsen regime and in micro-gravity: evidence for a "velostat" as boundary conditions", in *Powders and Grains*, 2005, vol. 97, pp. 1107–1111. 61

[129] R. Liu, M. Hou, and P. Evesque, "Simulation of 3d granular dissipative gas under different kinds of excitations & with different number of balls n", *Poudre & Grains*, vol. 17, pp. 1–561, 2009. 61

[130] P. Evesque, "Evidence for speed-symmetry breaking in steady state of dissipative granular gas in 0g", *Poudre & Grains*, vol. 17, pp. 563–576, 2009.

[131] P. Evesque, "Microgravité et gaz granulaire dissipatif dans un système vibré : un gaz à vitesse dissymétrique, mais à moyenne nulle", *Poudre & Grains*, vol. 17, pp. 577–595, 2009. 61

[132] J. W. Dufty, J. Javier. Brey, and A. Santos, "Kinetic models for hard sphere dynamics", *Physica A*, vol. 240, no. 1-2, pp. 212–220, JUN 1 1997. 79

[133] ML Tan and I Goldhirsch, "Rapid granular flows as mesoscopic systems", *Phys. Rev. Lett.*, vol. 81, no. 14, pp. 3022–3025, OCT 5 1998. 81, 82, 85, 86

[134] JW Dufty and JJ Brey, "Comment on '"rapid granular flows as mesoscopic systems"", *Phys. Rev. Lett.*, vol. 82, no. 22, pp. 4566, MAY 31 1999.

[135] ML Tan and I Goldhirsch, "Rapid granular flows as mesoscopic systems - reply", *Phys. Rev. Lett.*, vol. 82, no. 22, pp. 4567, MAY 31 1999. 82

[136] A Puglisi, V Loreto, UMB Marconi, A Petri, and A Vulpiani, "Clustering and non-gaussian behavior in granular matter", *Phys. Rev. Lett.*, vol. 81, no. 18, pp. 3848–3851, NOV 2 1998. 82

[137] CKK Lun, "Kinetic-theory for granular flow of dense, slightly inelastic, slightly rough spheres", *Journal of Fluid Mechanics*, vol. 233, pp. 539–559, DEC 1991. 92

[138] Lu Huilin, Dimitri Gidaspow, and Eirik Manger, "Kinetic theory of fluidized binary granular mixtures", *Phys. Rev. E*, vol. 64, pp. 061301, Nov 2001. 92

[139] J. Javier Brey, M. J. Ruiz-Montero, and F. Moreno, "Hydrodynamics of an open vibrated granular system", *Phy. Rev. E*, vol. 63, pp. 061305, 2001. 98, 113, 115, 116

[140] E. Clement and J. Rajchenbach, "Fluidization of a bidimensional powder", *Europhysics Letters*, vol. 16, no. 2, pp. 133–188, Sept. 1991. 98

[141] J. Javier Brey and M. J. Ruiz-Montero, "Velocity distribution of fluidized granular gases in the presence of gravity", *Phy. Rev. E*, vol. 67, no. 2, Part 1, FEB 2003. 98

[142] Yanpei Chen, Pierre Evesque, and Meiying Hou, "Experimental study on the local equation of state for granular gases", *Acta. Phys. Sin.*, vol. 62, no. 16, pp. 164503, APR 18 2013. 106

[143] Andrea Puglisi, *A numberical approach to the kinetics of driven and cooling granular gases*, PhD thesis, Universita Degli Studi Di Roma, 2001. 118